UNIVERSITY OF SOUTHAMPTON

FACULTY OF ENGINEERING AND THE ENVIRONMENT

Bioengineering Research Group

Nanostructure and mechanics of collagen fibrils from osteogenesis imperfecta mice and chronic asthma assessed with atomic force microscopy

by

Orestis G. Andriotis

Thesis for the degree of Doctor of Philosophy

December 2013

UNIVERSITY OF SOUTHAMPTON

ABSTRACT

FACULTY OF ENGINEERING AND THE ENVIRONMENT
Bioengineering Research Group

Doctor of Philosophy

NANOSTRUCTURE AND MECHANICS OF COLLAGEN FIBRILS FROM OSTEOGENESIS IMPERFECTA MICE AND CHRONIC ASTHMA ASSESSED WITH ATOMIC FORCE MICROSCOPY

by Orestis G. Andriotis

A number of pathologies are characterized by long term functional impairment of tissues and organs in the human body. Some case pathologies are directly associated with gene mutations that alter the biosynthesis of collagen; the basic structural element and most vital protein of biological tissues in vertebrates.

An example is osteogenesis imperfecta, a heritable bone disorder characterized by abnormally increased number of bone fractures. Other pathologies, however, develop over time as a result of tissue remodelling. In the case of asthma, the mechanical performance of the bronchial airways are now thought to be affiliated with alterations in the quality and quantity of collagen fibrils. This thesis is based on the hypothesis that both the structure and biochemistry is altered in collagen–related pathologies, and as a result of these alterations the mechanical properties of collagen fibrils are impaired.

The mechanical assessment of individual collagen fibrils (of larger than 100 nm in diameter) has been accomplished with a number of techniques, but atomic force microscopy (AFM) has been most widely used between several research groups and is the most promising technique at hand for this task. The main aim of this thesis was to assess the structure–mechanical function of collagen fibrils in osteogenesis imperfecta and asthma by employing AFM cantilever based–nanoindentation.

Prior to conducting scientific studies, the AFM cantilever based–nanoindentation was successfully validated with conventional nanoindentation, a well established technique in thin film nanometrology. Collagen fibrils from the *oim* mouse model of osteogenesis imperfecta were mechanically characterized. This, as well as an *in vitro* study, using ribose, to artificially cross–link collagen fibrils, demonstrated that the indentation modulus was much dependent on the amount of non–enzymatic cross–links present in collagen fibrils. Further, it became clear that alterations in the structure can have an effect on the type of cross–link predominantly formed, as well as the hydration behaviour of collagen fibrils, and hence also on elasticity and in further instance likely on the ductility. Collagen fibrils from asthmatic donors showed close a trend towards a lower indentation modulus compared to collagen fibrils from healthy donors. An unparalleled biochemistry study could in part complement on this difference but further experimentation is required to draw conclusions with certainty.

To date there are several avenues that could explain the nanomechanical changes seen in asthmatic collagen fibrils, yet the biochemical assays necessary to answer to these are, unfortunately, beyond the scope of this thesis. One possible change may be the amount of collagen types I and III, the abundant collagen types found in the submucosa. It is suggested that the fibril diameter of collagen type I is decreased with increasing the amount of collagen type III. The biochemistry study suggested a trend towards lower amount of type III collagen in asthmatics. In consequence of a possible decreased fibril diameter in asthmatics the density of the subepithelial layer in the airways could change and hence the mechanical properties at the tissue level. Beyond structural changes,

there could also be changes in the immature to mature cross–links which would affect the fibril mechanics. This is supported by evidence of decreasing indentation modulus with increase of the immature to mature cross–linking ratio. Moreover, a strong effect of non–enzymatic glycation end products on collagen fibril mechanics was observed. The indentation modulus of collagen fibrils with artificially induced AGEs (advanced glycation end products) was significantly increased.

This finding suggests that relative amount of glycosylated collagen fibrils in asthma could also be a contributing factor to the development of mechanical impairment of asthmatic airways. Nevertheless, findings within this thesis suggest that the biochemistry of collagen is directly associated with its mechanical performance. It has become clear during this thesis that the AFM serves as an important tool to characterize mechanically basic biological elements at the submicrometre scale. The technique used was highly effective towards associating the mechanics of individual collagen fibrils with pathology and biochemistry in model systems. Paralleled data are still needed to provide a holistic picture of a clear pathology state. Importantly, the technique is able to characterize the mechanics of individual collagen fibrils and the studies presented within this thesis have brought interesting results as well as further questions to be answered. With wider use of the technique it is anticipated that some of the issues raised within this thesis can also be discussed and answered by a larger research community.

Contents

List of Figures

List of Tables

Declaration of Authorship

I, Orestis G. Andriotis, declare that the thesis entitled *Nanostructure and mechanics of collagen fibrils from osteogenesis imperfecta mice and chronic asthma assessed with atomic force microscopy* and the work presented in the thesis are both my own, and have been generated by me as the result of my own original research. I confirm that:

- this work was done wholly or mainly while in candidature for a research degree at this University;
- where any part of this thesis has previously been submitted for a degree or any other qualification at this University or any other institution, this has been clearly stated;
- where I have consulted the published work of others, this is always clearly attributed;
- where I have quoted from the work of others, the source is always given. With the exception of such quotations, this thesis is entirely my own work;
- I have acknowledged all main sources of help;
- where the thesis is based on work done by myself jointly with others, I have made clear exactly what was done by others and what I have contributed myself;
- none of this work has been published before submission

Signed:.....

Date:.....

Acknowledgements

First and foremost my sincere thanks are due to my primary supervisor Prof. Philipp J. Thurner for his guidance and support where I needed them the most.

I am also indebted to Prof. Donna E. Davies and to Dr. Peter H. Howarth for providing me with fruitful discussions and valuable samples.

I would also like to thank Dr. Martin Stolz for our fruitful discussions in any subject and for providing his knowledge.

Thanks also to Prof. Simon Robins for fruitful discussions.

I would also like to thank people from the Bioengineering Research Group (with no specific order): Orestis, Tom, Tsiloon, Hatice, Faye, Hamid, Maria, Pramod, Lorenzo, Dario, Alex, Louise, Nick for providing one of the best environments to work at.

Special thanks I would like to give to Ermina for her support, encouragement and for endorsing my statistical questions.

Finally, I would also like to thank the EPSRC, MRC and AAIR Charity for the financial support of this PhD project.

Nomenclature

AFM	atomic force microscopy
AFM–cbN	atomic force microscopy cantilever–based nanoindentation
MEMS	microelectromechanical systems
OI	osteogenesis imperfecta
WT	wild–type
oim	osteogenesis imperfecta mouse
BHR	bronchial hyperresponsiveness
FEV_1	Forced Expiratory Volume at 1 second

α	half opening cone angle
β	correction factor
ε	indenter geometry shape factor
A_c	contact area function
E_i	indentation modulus of indenter
E_r	reduced indentation modulus
E_s	indentation modulus of sample
h	indentation depth
h_c	contact indentation depth
h_{max}	maxiumum indentation depth
m, n	power law fitting constants
S_c	contact stiffness
ν	Poisson's ratio
ν_i	Poisson's ratio of tip indenter
ν_s	Poisson's ratio of sample

Chapter 1

Introduction

1.1 Background

Collagen is a family of closely related but chemically distinct molecules that make up the extracellular matrix of tissues in the human body. To date, 28 different types of collagen, which compose 25% to 30% of the protein mass content of the human body, have been identified. This makes collagen the most abundant protein in the body of humans and, indeed, all vertebrates.

Collagen is involved in many important functions, such as cell adhesion, migration and chemotaxis. In addition, the dynamic interaction between cells and collagen regulates tissue remodelling during growth, differentiation, wound healing and morphogenesis (Montesano and Orci, 1988; Gumbiner, 1996). Certain collagen molecules assemble into long cylindrical structures, the collagen fibrils, with diameters ranging from 30 nm to 500 nm. Collagen fibrils play a dominant role in maintaining the structure of both hard tissues, such as bones, and soft tissues, such as tendons, ligaments, cartilage and the airways.

Bone is a family of tissues, which posses a composite structure composed of mineralized collagen fibrils immersed in a matrix of mineralized noncollagenous proteins (Fratzl et al., 2004; Launey et al., 2010). The interaction of these elements provide bone with its characteristic stiffness and toughness, which are important mechanical properties that enable bone to protect vital internal organs (such as the lungs, the heart and the brain) and provide support to the body.

In tendons and ligaments, the interaction between collagen fibrils and proteoglycans provides these tissues with increased ductility and energy storage (Fratzl, 2003). These mechanical properties allow tendons and ligaments, in cooperation with muscles and bones, to facilitate motion and skeletal integrity. In cartilage, aggrecan molecules bind water generating an osmotic swelling pressure, which counteracts the tense collagen fibril network (Stolz et al., 2009). This allows cartilage to withstand compressive forces during

motion. The extracellular matrix of the airways is composed of fibrous and structural proteins embedded in a hydrated polysaccharide gel, which forms a resilient framework (Holgate, 2009), important for breathing.

The aforementioned tissues possess complex hierarchical architectures, whose levels of hierarchy span from the nanoscale (e.g. molecules, mineral nanocrystals, proteins) to the macroscale (tissues and organs) (Weiner and Wagner, 1998; Fratzl and Weinkamer, 2007). Bone and tendon, for example, are composed of seven (7) and four (4) levels of structural hierarchy, respectively. The individual mechanical properties of the structural components at the nanoscale (collagen fibrils, minerals, proteoglycans) and their interactions determine the mechanical functionality of biological tissues at the macroscale (Rho et al., 1998; Currey, 2005; Fratzl and Weinkamer, 2007).

The mechanical functionality of biological tissues can be compromised due to ageing and due to pathology. A number of pathologies are related to impaired functionality of bone or lungs. Some of these pathologies, such as osteogenesis imperfecta and asthma, are then developed as a result of mutations of collagen genes or due to alterations of tissue remodelling, respectively.

Osteogenesis imperfecta (OI), also known as the "brittle bone disease", is an example of a hereditary disorder affecting mainly bones. Collagen gene mutations in OI result in abnormal biosynthesis of collagen fibrils which has been associated with impaired mechanical functionality of bones (Rauch and Glorieux, 2004). It is estimated that 6 to 7 per 100,000 people worldwide are affected by OI (Pagon et al., 2005). People with this condition suffer from multiple bone fractures in their lifetime (Paterson et al., 1984) or even before birth (King and Bobechko, 1971). Current treatment for OI focuses in increasing bone strength to prevent bone fractures and maintain mobility. Treatment with bisphosphonates increases bone mass and reduces bone pain. In severe cases of OI, bones are surgically corrected and rods are placed inside the bones (Rauch and Glorieux, 2005).

Asthma is an example of a lung disorder that is characterized, amongst other features, by tissue remodelling. Tissue remodelling in asthma alters the structure and composition of the extracellular matrix of the lungs (Holgate, 2009). In particular, the increased synthesis and deposition of collagen fibrils have been associated with impairment of the lung function (Kuwano et al., 1993; Carroll et al., 1993). Asthma is one of the most prevalent respiratory disorders affecting 1 in 8 children and 1 in 12 adults in the United Kingdom (Asthma, 2001). The World Health Organization estimates that 235 million people are affected by asthma worldwide. Common symptoms of asthma are shortness of breath, coughing, wheezing and tightness in the chest. Asthma symptoms might be the consequence of environmental factors, such as dust mites, pollen, animal fur and tobacco smoke or caused by chemicals, but may be also caused by non–environmental irritants, such as anxiety (Martinez, 2007; Gold and Wright, 2005) and vigorous breathing while

exercising (McFadden Jr and Gilbert, 1994). Bronchodilators are most commonly used to suppress the symptoms (Weinberger, 2004). When bronchodilators fail to restore the normal lung function, corticosteroids are usually prescribed (Weinberger, 2000).

Although, the mechanical properties of bone and the airways have been studied in OI and asthma, little is known regarding the association of these pathologies with the mechanical properties of collagen fibrils. Focusing on the mechanical properties of collagen fibrils will help understand the development of these pathologies.

1.2 Hypothesis

The structure bone, tendon and the airways are closely related with their mechanical properties. Structural changes at different hierarchical levels affect the mechanical properties and the overall functionality of the tissue. In OI, the mutations of the collagen gene affect the primary structure of the collagen molecules and most likely their assembly into collagen fibrils. In addition, structural changes at the molecular level of collagen may also affect the cross–linking of collagen fibrils.

Collagen fibril cross–linking (covalent bonds formed within the collagen fibril) is modified over the life course of biological tissues (Bailey, 2001). These modifications have been associated with changes in the mechanical properties of healthy tissues such as bovine skin and rat tail tendon (Bailey, 2001). Such modifications have also been found to occur in osteoporosis and diabetes mellitus (Saito and Marumo, 2010), pathologies that affect bone mechanical functionality (Dickenson et al., 1981; Currey, 2003; Coats et al., 2003). The above suggest that (i) the mechanical properties of collagen fibrils at the nanoscale are associated with the impaired functionality at the tissue level and that (ii) changes in the structure and cross–linking of collagen fibrils alter their mechanical properties. Yet, there is no evidence to directly associate structural and cross–linking changes with the mechanical properties of collagen fibrils.

This study is based on the hypothesis that the mechanical properties of collagen fibrils are altered in pathological tissues and that mechanical alterations are associated with changes in the structure and cross–linking of collagen fibrils.

1.3 Objectives and scope

The mechanical properties of collagen fibrils have been experimentally investigated with a number of techniques. Misof et al. (1997b) have used *in situ* mechanical testing with time–resolved small angle x–ray diffraction to investigate the structural changes in the rat tail tendon collagen fibrils during tensile loading (loading parallel to the long axis of fibrous specimens). Although this technique provides simultaneous measurements of

structural changes at the macroscopic, fibrillar and molecular level of collagen (Gupta et al., 2004), the results are based on oversimplified assumptions regarding the internal structure of collagen fibrils and on parameters that are not accurately determined (Misof et al., 1997b). Microelectromechanical systems (MEMS) have also been used to apply direct tensile loading on collagen fibrils (Shen et al., 2008; Eppell et al., 2006). During this approach, a MEMS device was used to test a single collagen fibril (Shen et al., 2008). The loading–unloading time was 7 min and the samples could not be immersed in aqueous solution (Shen et al., 2008). This has important limitations on the time and experimental efficiency of the technique, although MEMS can assess the tensile strength of collagen fibrils. Atomic force microscopy cantilever–based nanoindentation (AFM–cbN), also known as indentation–type AFM, has also been used to assess the mechanical properties of collagen fibrils (Heim et al., 2006; Wenger et al., 2007; Grant et al., 2008). AFM–cbN is, perhaps, the only technique at hand that can provide measurements of the mechanical properties of collagen fibrils under a variety of environmental conditions (temperature, aqueous solution). This mechanical testing approach involves indentation of a tip (with a radius of about 10 nm) onto the surface of a collagen fibrils. During indentation, the reaction force and displacement is recorded and measurements of elastic modulus can be determined. To derive the elastic modulus, it is important to normalize the applied force over the contact area between the tip and the sample. Therefore, knowledge of the contact area is required.

Although, a number of experiments have been carried out to investigate the mechanical properties of collagen fibrils and their contribution in tissue mechanical properties, these studies were focused on healthy tissue. In this thesis I have used the AFM–cbN as a tool to assess the mechanical properties of collagen fibrils in pathology.

The initial focus of the current thesis was to perform a reliability test on the determination of the contact area of the AFM tip. The reliability test was performed by comparing results from AFM–cbN with conventional nanoindentation, a well established indentation technique used widely in thin film metrology (Fischer-Cripps, 2012), on polymers with known mechanical properties. The scope of the reliability test was to develop and optimize a protocol for nanomechanical assessment of murine and human collagen fibrils. The protocol was applied to (i) investigate changes in the mechanical properties of collagen fibrils and (ii) study the association of cross–linking with the mechanical properties of collagen fibrils. A mouse model of osteogenesis impefecta was used to investigate changes in the mechanical properties of collagen fibrils. Chemically treated collagen fibrils from a healthy mouse (wild–type mouse) and collagen fibrils from asthmatic individuals were used to study the association of cross–linking with the mechanical properties of collagen fibrils.

1.4 Structure of the thesis

Chapter 2 introduces the reader to the main structural and mechanical properties of collagen fibrils and collagen–based tissues. In this chapter the structural and mechanical alterations in bone from *oim* mouse and the structural changes in asthmatic airways are also discussed.

Chapter 3 is dedicated to AFM and how it is employed to assess the mechanics of collagen fibrils. The basic imaging modes used in AFM are described. In addition the cantilever–based nanoindentation technique performed with the AFM is further described together with the two basic analysis methods used, the Hertzian model and the Oliver–Pharr method.

Chapters 4 to 6 describe the experimental work: Chapter 4 presents the study conducted to test the reliability of atomic force microscopy cantilever–based nanoindentation for nanomehcanical assessment on murine and human collagen fibrils (with diameter ranging from 30 nm to 200 nm). Chapter 5 compares the nanomechanical properties of collagen fibrils from *oim* mice and their wild type littermates. Chapter 6 shows the effect of the amount and type of cross–linking on collagen fibril mechanics. In this chapter the potential association between the mechanical properties and cross–linking of collagen fibrils is discussed.

Chapter 7 summarizes the findings of the current thesis and suggests future directions towards providing a better understanding of collagen–related pathologies.

Chapter 2

Collagen structure and mechanics in health and pathology

2.1 Basic nomenclature

Collagens represent a family of chemically distinct but closely related molecules. Collagen molecules are made up of three inter–coiled polypeptide chains forming a rope–like conformation.

The polypeptide chains are termed α–chains[1]. The α–chains with different primary structure (i.e. amino acid sequence) are numbered with arabic numerals, e.g., $\alpha 1$, $\alpha 2$ etc. The most commonly used terminology of the distinct collagens is "collagen types". The collagen type is numbered with a roman numeral, which is added in parentheses following the arabic numerals and indicates the order of discovery. For example, the composition of type I collagen, the most common and abundant collagen type, is written as $[\alpha 1(\mathrm{I})]_2\alpha 2(\mathrm{I})$. This indicates that the type I collagen molecule is composed of two identical $\alpha 1(\mathrm{I})$ chains and one $\alpha 2(\mathrm{I})$. Chains with same arabic number but different roman one are not identical and possess different primary structure i.e. $\alpha 1(\mathrm{I})$ and $\alpha 1(\mathrm{II})$. Collagen molecules composed of three identical α–chains (same arabic and roman numbers) are known as homotrimeric whereas collagen molecules composed of up to three distinct α–chains (different arabic but same roman numbers) are known as heterotrimeric (Kucharz, 1992; Hulmes, 2008; Myllyharju and Kivirikko, 2004).

The collagen molecule is synthesized by a precursor protein. Precursor proteins are inactive form of proteins that through post–translational modification can become active. The polypeptide chains in the nascent form are termed pre–pro–collagen and abbreviated as pre–pro α followed by the corresponding arabic numeral. The signal peptide is cleaved to form pro–collagen chains. After being subjected to a number of post–translational

[1] Not to be confused with the alpha helix, which has a right–handed spiral conformation.

modifications, three pro–collagen chains are assembled into the pro–collagen molecule. The collagen molecule is then formed by cleavage of the pro–peptides on the two ends of the molecule. In total, six telopeptides are removed. The final molecule is termed collagen, synonym to tropocollagen, and is the basic unit of collagen fibrils and other collagenous structures (Kucharz, 1992; Hulmes, 2008).

Depending on the supramolecular architecture of collagen molecules, they are further classified as transmembrane (Types XIII, XVII, XXV), fibril–forming (Types I, II, III, V, XXIV, XXVII), fibril associated collagens with interrupted triple helices (or FACITs, Types IX, XII, XIV, XVI, XIX, XX, XXI, XXII), beaded filament (Type VI), network–forming (Type IV, VIII, X) and anchoring fibrils (Khoshnoodi et al., 2006).

Type I collagen molecules make up about 90% of the total collagen content in the body (Lodish et al., 2000). In this chapter I will focus on the structure and mechanical properties of type I collagen molecules and fibrils. I will also describe, in brief, the hierarchical structure of bone, tendon and bronchial airway walls in respect of the type I collagen fibril organization and their interactions with other structural elements.

2.2 Synthesis of collagen molecules and fibrils

Generally, protein synthesis involves two basic events, the transcription of DNA into mRNA and the translation of mRNA into a polypeptide, the primary structure of a protein. The polypeptide chains are made up of linear chains of amino acids. Consecutive amino acids bind with peptide bonds (strong covalent bonds), formed between the carboxyl group (-COOH) of one amino acid and the amine group ($-NH_2$) of the next amino acid. This results in a free amine group (N–terminal) and a free carboxyl group (C–terminal) on the polypeptide chain. Finally, a number of post–translational modifications result in the three dimensional conformation and structure of the synthesized protein[2].

The synthesis of collagen has been extensively studied in respect to fibril–forming collagen molecules and involves a number of intracellular and extracellular post–translational modifications. In collagen synthesis, the transcription of mRNA results in the formation of the pre–pro–peptide (Prockop et al., 1979; Kadler et al., 1996). The post–transaltional events result in the formation of pro–collagen molecules made up of three α–chains forming triple helical structures with N– and C–telopeptides (Myllyharju and Kivirikko, 2004). Assembly of pro–collagen molecules into collagen fibrils initiates extracellularly, with the cleavage of N– and C– telopeptides from the pro–collagen molecules resulting in the formation of collagen molecules of about 300 nm in length and 1.5 nm in diameter. The ultra high aspect ratio of collagen molecules is thought to be responsible for the

[2]General knowledge in protein synthesis found in textbooks of biology.

ability of these molecules to self–assemble into long fibrils (Myllyharju and Kivirikko, 2004).

Collagen molecules self–assemble into collagen fibrils by aggregating in both lateral and longitudinal directions. The fibrillar structure is stabilized by inter–molecular covalent bonds formed in the lateral direction of the fibril structure (Kadler et al., 1996; Eyre and Wu, 2005). An illustration of collagen fibril assembly is shown in Figure 2.1.

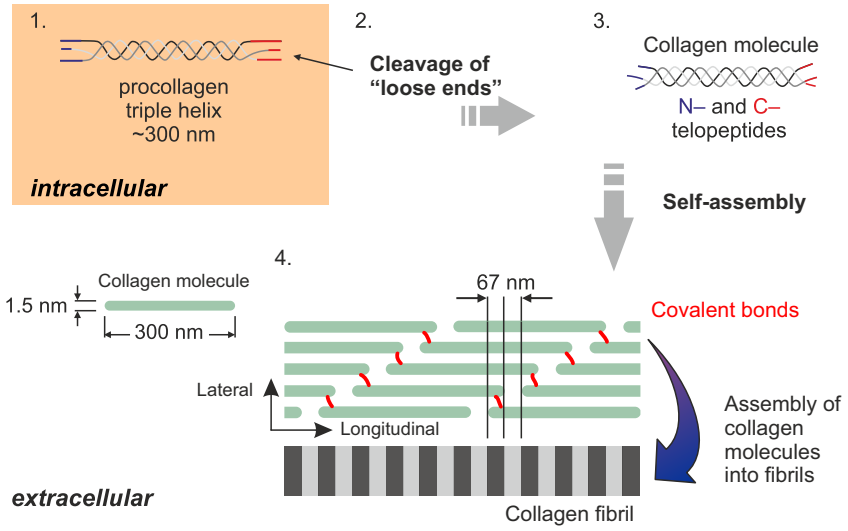

Figure 2.1: Pro–collagen molecules are formed intracellularly (1). Collagen molecules result from cleavage of the "loose ends" of pro–collagen. The collagen molecule (pale green thick line) self–assembles into fibrillar structures that range from 10 μm to 100 μm in length and have a characteristic D–period (4).

2.3 Collagen cross–linking

The type of collagen cross–links are divided into two main categories depending on the origin of their formation. The enzymatic and non–enzymatic cross–links, which are divalent and trivalent inter–molecular bonds.

2.3.1 Immature and mature enzymatic cross–links

The enzymatic cross–links are first to form during the fibrillar assembly of collagen. These cross–links are important to stabilize the newly formed fibrillar structure of collagen (Khoshnoodi et al., 2006). Enzymatic cross–links are initiated by enzymes, such as the lysyl oxidase and hydroxylase. Lysyl oxidase and hydroxylase act on specific molecular segments deaminating the lysine and hydroxylysine residues located at the telopeptides. This results in the formation of a divalent Schiff base inter–molecular cross–link between the non–helical and helical domains of adjacent molecules, as illustrated in Figure 2.2. During time, the divalent cross–links undergo chemical reactions

resulting in the formation of trivalent cross–links. These trivalent cross–links are termed mature cross–links are bridging a third collagen molecule, as illustrated in Figure 2.2.

2.3.2 Non–enzymatic cross–links

The non–enzymatic cross–links occur later in time from the formation of the collagen fibril. Non–enzymatic cross–links result from instantaneous chemical reactions between collagen and glucose. The process initiates with a Maillard reaction which is a reaction between amino acids and sugar (Maillard, 1912). Further oxidation leads to the formation of advanced glycation end products (AGEs). The non–enzymatic cross–links can form anywhere between the helical domains of adjacent collagen molecules, as illustrated in Figure 2.2.

Studying the type and amount of collagen fibril cross–linking has been the focus of a number of researcher in a need to understand how the cross–linking is associated with changes in the mechanical properties of tissues. This will be discussed further in section 2.7

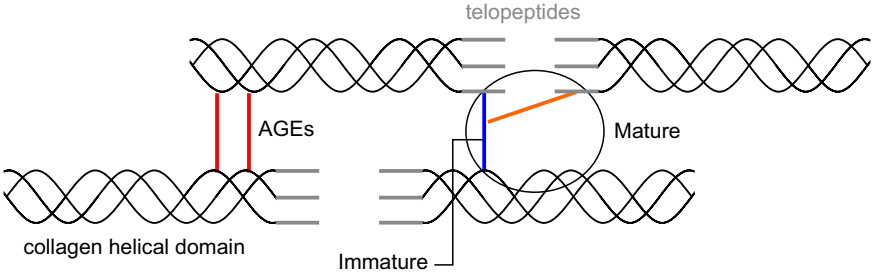

Figure 2.2: Enzymatic (immature and mature) and non–enzymatic (advanced glycation end products; AGEs) cross–links in type I collagen fibril.

2.4 Structure and tissue organization of collagen molecules and fibrils

2.4.1 The triple helical structure of collagen molecule

The triple helical structure was discovered on the basis of x–ray diffraction by Ramachandran and Kartha (1954). The helical formation results from the high content of glycine (Gly) residues in the α–chain and the position of these residues in the core of the collagen molecule.

Each α–chain in type I collagen molecule possesses a left–handed twist and is characterized by the Gly–X–Y motif. This motif follows either the pattern Gly–Pro–Y or

Gly–X–Hyp (Pro: proline, Hyp: hydroxyproline residues), in either case of which X and Y can be any other amino acid (Ottani et al., 2001). The α–chains consist of a sequence of about 300 [Gly–X–Y] motifs, where the Gly residues are located in the core and the X and Y are exposed towards the surface of the molecule (Jones and Miller, 1991), as shown in Figure 2.3. The small size of Gly residues and its location in the core are responsible for the close packing of the three α–chains. The three left–handed α–chains are coiled into a right–handed molecule, as shown in Figure 2.3.

The triple helix is stabilized by the hydroxylation of the prolyl and lysyl residues (Kivirikko and Prockop, 1967). Hydroxyproline has been suggested to enhance stability by the formation of extra hydrogen bond (Ramachandran et al., 1973).

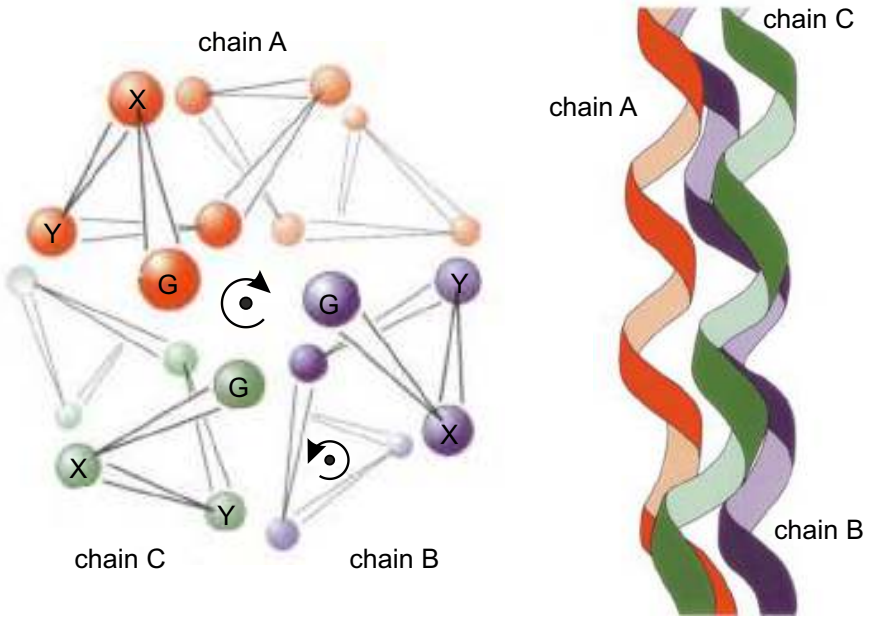

Figure 2.3: Transverse and longitudinal perspectives of collagen triple helix. Three left–handed coiled α–chains are coiled into a right–handed super–helix. Adapted from (Beck and Brodsky, 1998) with permission. Copyright (1998) Academic Press.

2.4.2 Fibrillar structural models of collagen

The fibril structure involves the lateral and longitudinal organization of collagen molecules. A number of models have attempted to describe the structure of collagen fibrils on the basis of the characteristic D–periodicity on the fibril surface, (Figure 2.4).

The D–periodicity was revealed by staining collagen fibrils with sodium phosphotungstic acid and recording electron migrograph images of the stained samples (Williams et al., 1978; Chapman et al., 1990). The (EM) images revealed dark and white zones on the

fibril surface (Williams et al., 1978). The dark zones corresponded to lower and the white zones to higher density. This resulted in the hypothesis that there are gap regions (dark zones), where the density of molecular packing is decreased, and overlap (white) regions, where the density of molecular packing is increased. The length of a continues dark and white pattern (gap + overlap region) was 67 nm appearing along the fibril longitudinal direction.

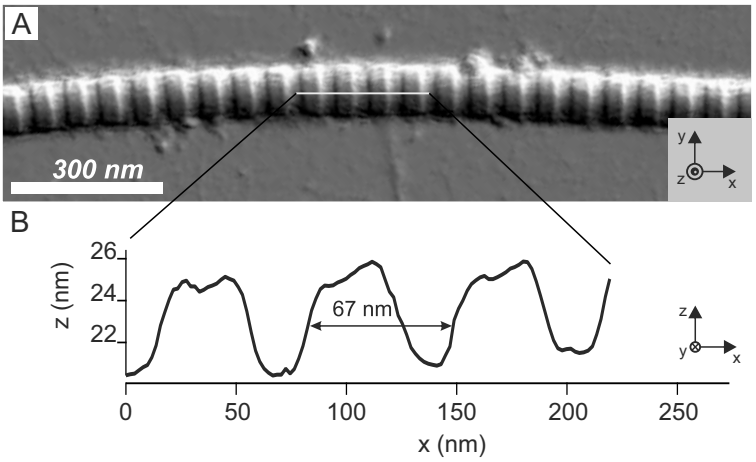

Figure 2.4: (A) Atomic force microscopy image and (B) section analysis of human bronchial collagen fibril showing the characteristic D–banding.

Petruska and Hodge (1964) attempted to describe the D–periodicity of collagen fibrils by presenting a two dimensional model of collagen fibril subunit. According to this model the collagen molecules are staggered on top of each other by an offset in the longitudinal direction of 234 residues, as shown in Figure 2.5 (Petruska and Hodge, 1964; Kühn, 1986). This staggered arrangement results in overlap regions, where all five molecules overlap and in gap regions, where there is an empty space, as illustrated in Figure 2.5. Although this model helps to explain the origin of D–periodicity, it fails to reconcile the longitudinal rearrangements and the three dimensional conformation of collagen molecule into a fibrillar structure.

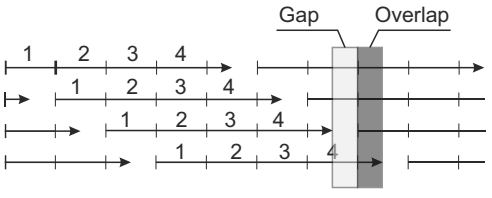

Figure 2.5: The collagen molecule is represented by an arrow segmented in four portions, labelled from 1 to 4. Each portion corresponds to 234 residues. The total length of the molecule is one–third of one portion larger than the overall length of all four portions.

The models, attempted to describe the fibrillar sub–structure of collagen, are divided into two groups depending on the proposed structure.

In the first group, a microfibril structure is suggested to be the fundamental building block of collagen fibrils. These models suggest a crystalline packing of collagen molecules into fibrils. The microfibril is composed of five–stranded collagen molecules which lie on a pseudo–hexagonal lattice (Smith, 1968). Trus and Piez (1980) refined the five–stranded model suggesting a compressed structure which allows quasi–hexagonal lateral packing. Fraser et al. (1983); Wess et al. (1995) suggested that microfibrillar structures interconnect. Figure 2.6 illustrates the electron density (Figure 2.6A) and the triclinic unit cell of the microfibril (Figure 2.6B). More recently, Orgel et al. (2006) suggested a right–handed supertwisted microfibrillar structure.

In the second group, collagen molecules form a quasi–crystalline three dimensional array. This model was initially proposed by Hulmes and Miller (1979). In addition to the quasi–hexagonal array models, Silver et al. (1992) developed a cylindrical model to explain the fibrillar structure of collagen in the lateral packing direction. The model was then refined to the concentric ring model by Hulmes et al. (1995). This model suggests a mix of ordered and disordered structure of the fibril. These results were corroborated with x–ray diffraction patterns that suggested a structure which varies between a crystal and a liquid–crystal.

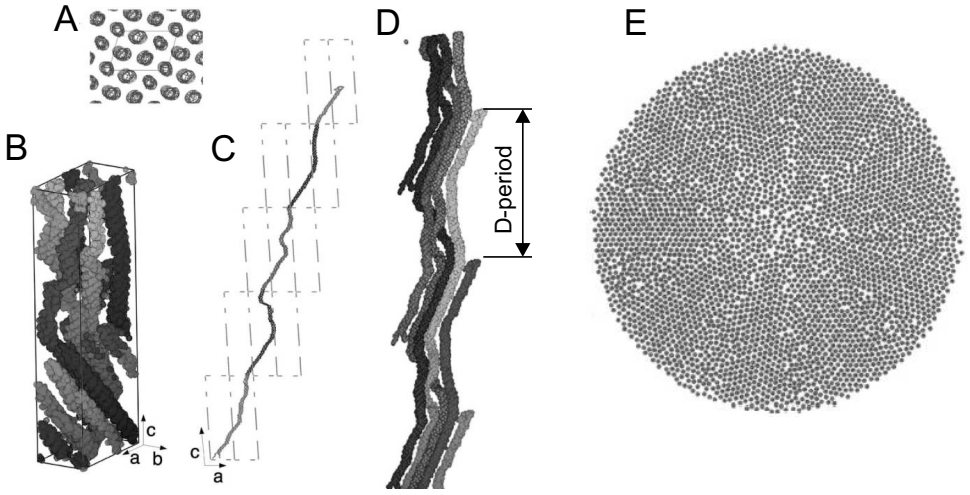

Figure 2.6: (A) a–b plane of the unit cell showing the electron density of molecular segments packed in a quasi–hexagonal manner. (B) Single unit cell with carbon atoms of backbone of collagen molecules shown as spheroids. The microfibril has a triclinic unit cell (a $\approx$ 40.0 Å, b $\approx$ 27.0 Å, c $\approx$ 678 Å, $\alpha \approx 89.2^o$, $\beta \approx 94.6^o$, $\gamma \approx 105.6^o$). The molecules are densely packed in the overlap regions and more flexible in the gap regions. (C) Path of collagen molecule through unit cells in the a–c plane. The molecule is segmented into different grayscale level, each of which denotes which segment of the molecule is included in the microfibril unit cell. (D) Illustration of molecular kinks. (E) Radially packed cylindrical structure suggesting a cascaded structure of crystal and liquid–crystal. Each dot corresponds to the collagen molecule cross–section. (A-D) Adapted from (Orgel et al., 2006) with permission. Copyright (2006) National Academy of Sciences, U.S.A. (E) Reprinted from (Hulmes et al., 1995) with permission. Copyright (1995) The Biophysical Society.

2.4.3 Organization of collagen fibrils at the tissue level: The structure of bone, tendon and bronchial airway walls

Collagen fibrils are packed into fibres and form complex structure with the inclusion of supplementary biological materials, such as proteoglycans or mineralized nanoparticles. Below, a brief overview of the basic structural organization of bone, tendon and bronchial airway walls, is give.

2.4.3.1 The structure of bone

Bone is a remarkable lightweight and robust material with a hierarchical architecture. The different levels of hierarchy include the basic structural elements of bone and the structural entities that these elements form through their interactions. The bottom up hierarchical structure of bone is described below, which is illustrated in Figure 2.7.

Levels 1–3: Levels 1 to 3 refer to the bone nanostructure. Type I collagen fibrils (of about 100 nm in diameter), mineral nanocrystals (calcium–based hydroxyapatite), non–collagenous proteins and water are the structural elements of bone at the nanoscale. Mineralization takes place during collagen fibrils formation and is an important process, responsible for the increased stiffness of bone, during bone formation. The process is characterized by inter–molecular and inter–fibrillar deposition of minerals Landis et al. (1993). Non–collagenous proteins are thought to participate in the mineralization process due to their ability of binding calcium (Eanes, 1992). Mineralized collagen fibrils are embedded in a matrix of mineralized non–collagenous proteins (Fantner et al., 2006) forming larger collagen fibres (of about 1 μm in diameter) (Weiner and Wagner, 1998).

Level 4 and 5: Mineralized collagen fibres are then organized into "sheets" (of 3 μm to 7 μm in width), termed lamellae. Lamellae are the basic building blocks of bone micro– and macro–structure (Rho et al., 1998). Bone lamellae are concentrically arranged around blood vessels forming osteons (Weiner and Wagner, 1998; Rho et al., 1998).

Level 6 and 7: The two major types of bone tissue are the cortical (or compact) bone and the trabecular (or cancellous) bone. Cortical bone is dense, consisting of osteons and lamellar bone (lamellar bone does not form concentrically but rather parallel and is found between osteons) (Rho et al., 1998). Trabecular bones is porous and consists of trabecular packets (Rho et al., 1998). Finally, level 7 corresponds to the whole bone structure and refers to the geometrical features of the bone.

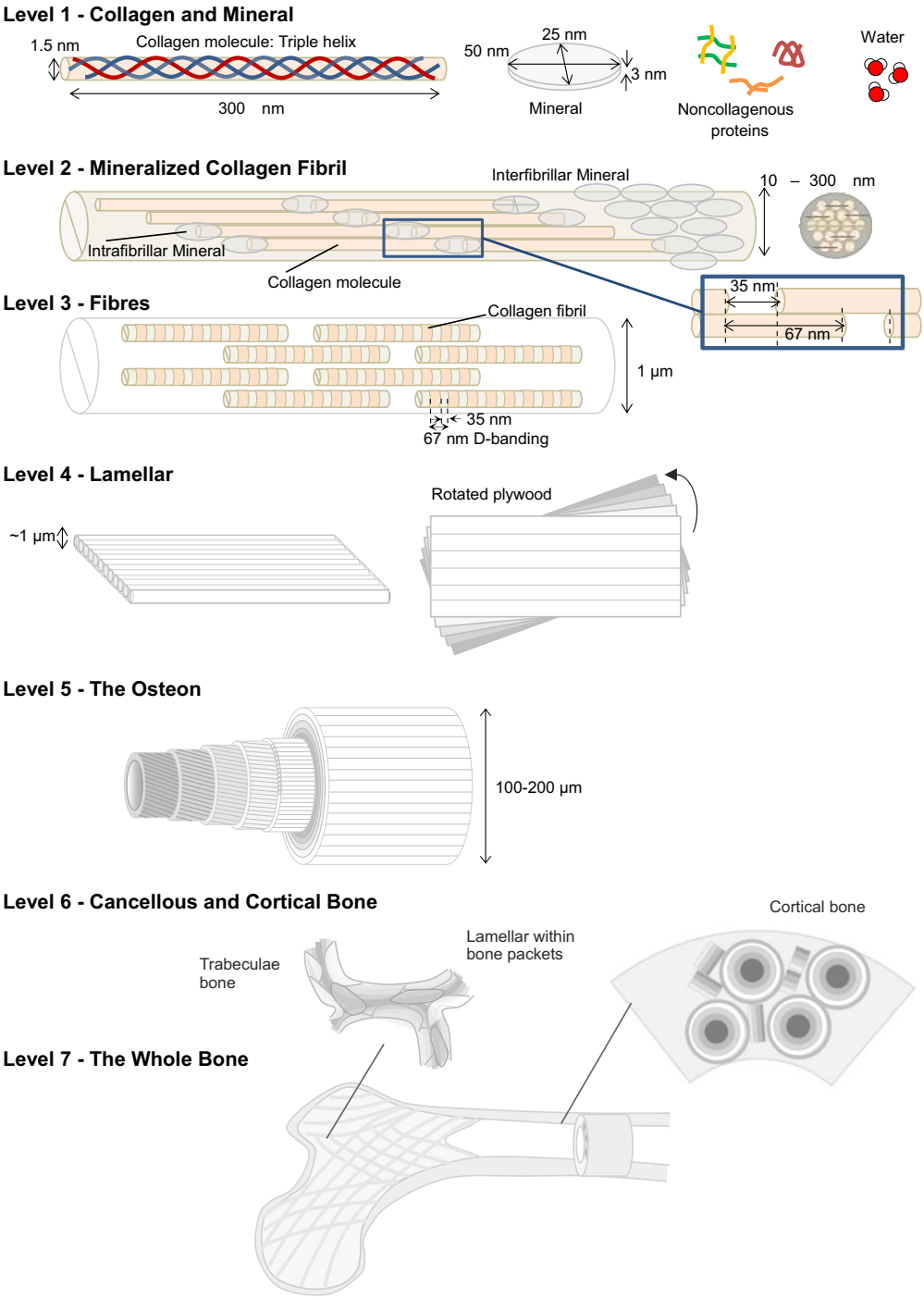

Figure 2.7: The basic building blocks of bone are collagen molecules, minerals, noncollagenous proteins and water. These assemble into mineralized collagen fibrils. Minerals are deposited in the intrafibrillar and interfibrillar space. Then collagen fibers are formed and compose the lamellar structure of bone. Lamellar bone forms into larger structures called osteons which compose both trabeculae and cortical bone. These are the characteristics structures of whole bones. Figure courtesy of T. Jenkins.

2.4.3.2 The structure of tendon

Tendon possesses a slightly less complex structure than bone. Similar to bone, the basic structural elements compose the nanostructure of tendon and those are type I collagen fibrils (with a wide range diameter distribution from 50 nm to 500 nm), proteoglycans and water. Collagen fibrils are embedded in a hydrophilic non–collagenous matrix containing proteoglycans, mainly biglycan, decorin, glycoproteins and glycosaminoglycans (Scott et al., 1981; Kannus, 2000). Smaller fibrils are formed in the vicinity of the larger fibrils, which increases lateral packing in tendon (Ottani et al., 2001). The close packing of collagen fibrils result in the formation of fibril bundles, which compose larger structures, the fascicles (ranging from 50 μm to 300μm), as illustrated in Figure 2.8. The fascicles are then assembled into the tendon fibre, which ranges from 100 μm to 500 μm (Fratzl, 2003).

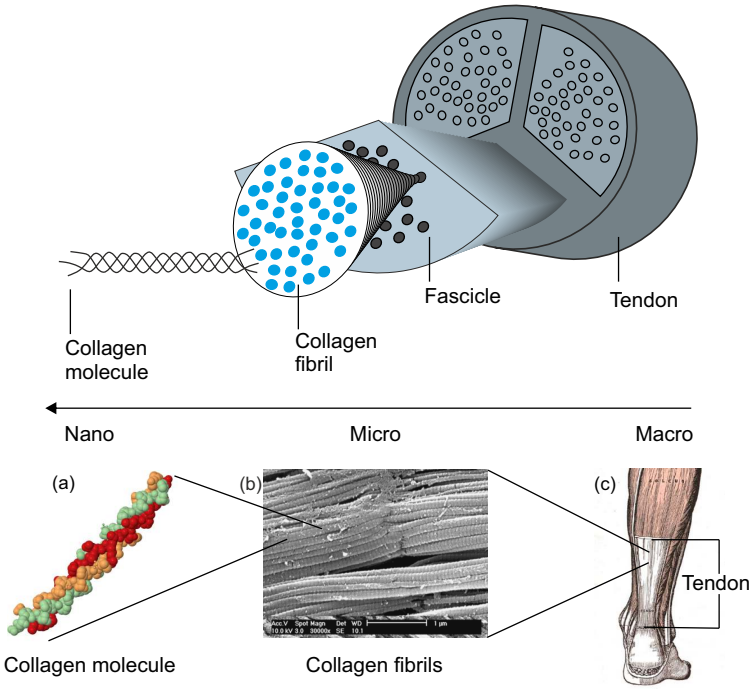

Figure 2.8: Cartoon illustration of the architecture of tendon from the molecular up to the tissue level. Panel a shows a collagen molecule, panel b shows a scanning electron microscope image of collagen fibrils from Achilles tendon and panel c shows the Achilles tendon in the human body. Panel a was printed from the Protein Data Bank (PDB) using the structure of 1BKV (PDB ID) via the Jmol software. Panel b was reprinted from Franchi et al. (2007) with permission. Copyright (2010) Journal of Anatomy. Copyrights for panel c have expired.

2.4.3.3 The structure of bronchial airway wall in the lung

Bronchial airways possess a fractal geometry, similar to a tree, that begins from a single feature that splits to branches with decreasing diameter. Bronchial airways are tube–like structures allowing the air to pass through to reach the alveoli, where gas exchange takes place. Figure 2.9 shows an illustration of the hierarchical architecture of bronchial airway wall.

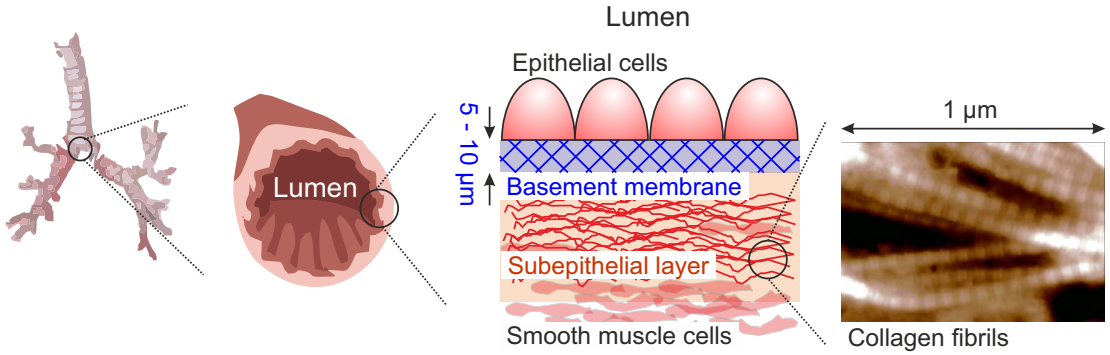

Figure 2.9: (*From left to right*): Cartoon illustration of the bronchial three, bronchial airway section and structure of bronchial tissue. Atomic force microscopy height image of bronchial collagen fibrils from healthy airway bronchial tissue.

The basic structural elements of the airway wall are fibril–forming collagen molecules (type I, III and V), the network–forming collagen molecule type IV, all of which are embedded in a hydrated polysaccharide gel made of laminin and proteoglycans (Leblond and Inoue, 1989; Holgate, 2009).

A summary of the major constituent of the extracellular matrix of the bronchial airway wall is shown in Table 2.1. Collagen type I fibrils predominate (60% of protein mass) and together with collagen type III and V fibrils comprise the subepithelial layer of the airway wall. The collagen fibrils in the subeptithelial layer possess a rather narrow fibril distribution of 30 nm, based on findings from this thesis, which could be explained by the presence of type III collagen molecules (Birk and Mayne, 1997). The type II collagen fibrils compose the extracellular matrix of cartilage that is present in the surrounding of bronchial airways (Mendler et al., 1989). Type IV collagen molecules form a network (Myllyharju and Kivirikko, 2004), which composes the basement membrane of the airway wall. Type V collagen fibrils are also found in the border between the subepithelial layer and the basement membrane (Clark et al., 1983). The basement membrane is found between the subepithelial layer and the epithelial cells, as illustrated in Figure 2.9.

Collagen	
Type I	Subepithelial layer
Type II	Bronchial and tracheal cartilage
Type III	Co–localization with type I collagen
Type IV	Basement membrane
Type V	Basement membrane,
Elastin	Subepithelial layer
Proteoglycans	Basement membrane
Laminin	Basement membrane
Fibronectin	Basement membrane

Table 2.1: Major extracellullar matrix constituents of bronchial airway wall. Adapted from (Godfrey, 2009).

2.5 Basic mechanical properties of biological tissues

The different structural properties among bone, tendon and bronchial airways, provide these tissues with a variation of mechanical functions. Investigating the mechanical properties of biological materials is important to understanding their structural–mechanical relationship. Below I will introduce the most common mechanical properties of biological materials before discussing the mechanical properties of collagen.

The mechanical properties of biological tissues is determined by measuring the reaction displacement caused by an external force (panel A from Figure 2.10). The force–displacement curve in Figure 2.10A is characterized by a linear and a non–linear part. The slope of the linear part corresponds to the stiffness (S) of the biological tissue. The stiffness describes the magnitude of the force that the tissue can transmit relative to the total deformation caused. Biological tissues with high stiffness can transmit the forces and resist displacement (or deformation), unlike less stiff ones. The non–linear part of Figure 2.10A corresponds to permanent deformation and damage of the tested biological tissue. The ultimate force (Fu) corresponds to the maximum force reached at which point the material is damaged (Figure 2.10A). The damage can be described as the discontinuity caused in a portion of the volume of the tissue. This portion of the tissue experiences the highest deformation. The ultimate displacement (du) corresponds to the maximum deformation at the fracture point (Figure 2.10A). The area under the force–displacement curve (grey area in Figure 2.10A) corresponds to the energy needed to break the sample.

A tensile force causes elongation to the tissue, as shown in Figure 2.10B. With known the dimensions of the tissue sample, the force–displacement curve can be normalized to provide the stress–strain curve (Figure 2.10C). Stress measurements result from normalizing the applied force by the projected area of contact. Strain measurements correspond to the percentage of elongation. The stress–strain curve is divided into two regions, the elastic (linear part) and the plastic region (non–linear part). The slope of the linear

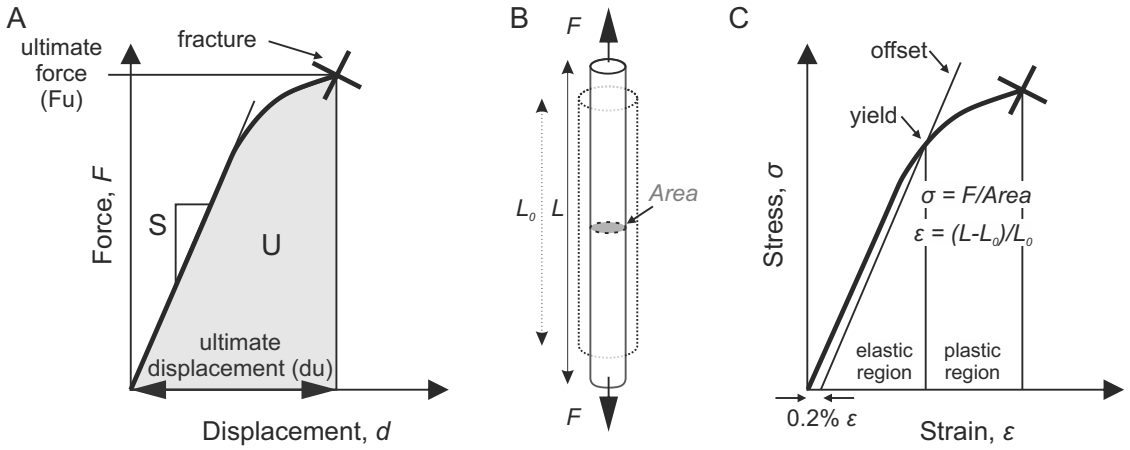

Figure 2.10: Panel A shows a force–displacement curve to the four basic mechanical properties of (biological) materials. Panel B is a schematic illustration of a tensile force resulting in elongation of a material. Panel C illustrates a stress–strain curve showing the elastic, plastic regions and the yield point. S: stiffness; U: work of fracture; L_0: initial length; L: final length. Panel A was adapted with permission from (Sato et al., 1999). Copyright (1999) American Chemical Society.

part of the stress–strain curve corresponds to the elastic modulus. The elastic modulus is a property of the elastic deformation of the tissue. During elastic deformation the tissue returns to its initial dimensions after removal of the applied force, unlike a plastic deformation where there is permanent deformation. The transition from elastic to plastic deformation occurs at the yield point. In materials science, the yield point can be determined by an offset of 0.2% of the strain, as illustrated in Figure 2.10B. The area under the stress–strain curve provide measures of toughness. Toughness is the measure of the ability of the tissue to absorb energy up to fracture. An important measure of toughness is the *fracture toughness*. Fracture toughness describes the ability of a tissue to resist the propagation of a crack across the volume of the tissue.

The deformation mechanisms of bone, tendon and bronchial airways are discussed below. Bone, tendon and bronchial airways have been chosen to discuss the effect of their different structural extracellular matrix organization (cf. §2.4.3) on the mechanical properties of the tissues.

Bone

The high elastic modulus of bone minerals (≈100 GPa) is responsible for the high stiffness of bone. Collagen fibrils, withstand larger deformations, are responsible for the increased toughness of bone. The large aspect ratio of mineral crystals (Landis et al., 1993) increases the contact area between collagen molecules and crystals which provides additional resistance against plastic deformation (Buehler, 2007). Additional deformation occurs between the extrafibrillar minerals in bone. Jäger and Fratzl (2000) have

suggested that load transfer between extrafibrillar minerals occurs in the organic matrix by shear transfer.

Based on *in situ* tensile loading with synchrotron x–ray diffraction measurements, Gupta et al. (2006) investigated the strains at three hierarchical levels of the structure of bone. During tensile loading of fibrolamellar bone sheets, Gupta et al. (2006) measured the average maximum value of mineral strain to be between 0.10% to 0.20%. The 5:2 ratio of fibril to mineral strain suggests that there is a load transfer between the mineral crystals and the mineralized collagen fibrils (Gupta et al., 2006). The authors observed differences between experiments of wet and dry bone. From their results, Gupta et al. (2006) suggested that a stiffer organic matrix (the dry collagen fibrils) would cause the composite to be stiffer. This stiffening, due to more effective load transfer between minerals and collagen fibrils in bone, may also be the cause of increased fracture risk in some bone diseases, such as osteogenesis imperfecta. However, such effects have not been elucidated.

Tendon

The large amount of type I collagen fibrils, the presence of elastin and proteoglycans provide tendon with increased toughness and the ability to store energy during loading.

During tensile loading, elastin is deformed at lower stresses contributing to lower deformation strain of the tissue (Oxlund and Andreassen, 1980).Collagen fibrils are stiffer and withstand larger deformation than elastin. Proteoglycans are found around the periphery of collagen fibrils (Scott, 1980) and allow inter–fibrillar sliding, as illustrated in Figure 2.11.

A typical stress–strain curve of tendon is shown in Figure 2.12. The macroscopic crimp, illustrated in Figure 2.12A, of about 100μm, is removed at low applied forces corresponding to the toe region (Diamant et al., 1972). Straightening of the kinks in the gap region is believed to account for the heel region (Misof et al., 1997b). Finally, inter–molecular sliding of collagen, occurring at higher applied forces, may account for the linear region of the stress–strain curve of the tendon.

Moreover, incorporation of small collagen fibrils would increase the surface to volume ratio promoting more inter–fibrillar binding. Since tendon failure can occur by either tear or creep, the smaller fibrils are thought to enhance creep resistance whereas the larger fibrils provide strength to the tissue (Ottani et al., 2001).

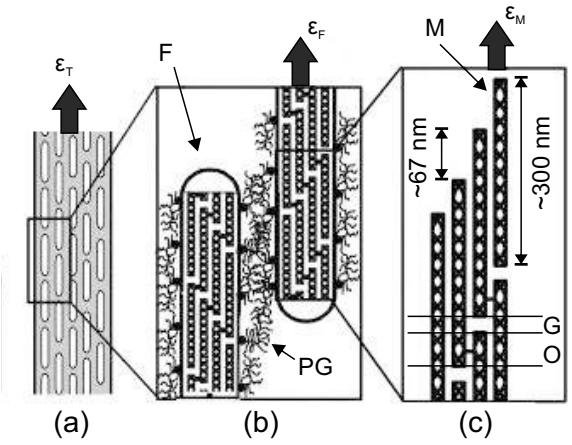

Figure 2.11: During tensile loading, the tendon fascicle, shown in panel a, is subjected to strain ε_T and collagen fibrils slide past each other. A portion of the tendon strain is taken up by the deformation of the proteoglycan matrix and the remaining strain (ε_F) from the collagen fibrils, illustrated in panel b. Similarly, collagen molecules also take up part of the fibril strain, as illustrated in panel c. This strain is $\varepsilon_M.\varepsilon_T$: tissue strain; ε_F: fibril strain; PG: proteoglycans; F: collagen fibril; M: collagen molecule ε_M: molecular strain; Adapted from Fratzl (2003) with permission. Copyright (2003) Elsevier Science Ltd.

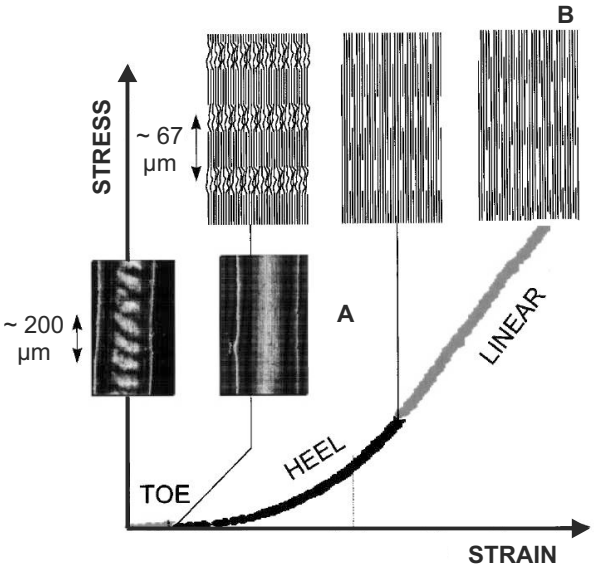

Figure 2.12: Qualitative illustration of the different regions in a typical stress–strain curve of a rat tail tendon. Reprinted from Fratzl et al. (1998) with permission. Copyright (1998) Academic Press.

Bronchial airways: The stiffness of bronchial airways is predominantly accounted to the subepithelial layer. The stress bearing elements of the subepithelial layer is collagen and elastin. The longitudinal modulus of elasticity of collagen is one order of magnitude larger than elastin (collagen is ≈1 GPa; elastin is ≈0.3 MPa) (Burton, 1954). It has been

suggested that deformation of elastin and collagen occurs at different stress levels due to the large heterogeneity of their elastic properties (Maksym and Bates, 1997). During deformation of lung tissue, elastin bears loading at low strain and collagen accounts for stiffening of the tissue at higher strains. The relative contribution of elastin and collagen in lung tissue results in a non–linear behaviour of the stress–strain curve (Maksym and Bates, 1997). Digestion of both elastin and collagen, with elastase and collagenase respectively, resulted in softening of lung tissue (Yuan et al., 2000). In fibrosis, lung tissue is characterized by increased deposition of collagen and elastin (Hoff et al., 1999).

The ability of collagen fibrils to take up large deformations without fracturing makes collagen fibrils important in respect to mechanical properties. For this reason, I will discuss below the mechanical properties and deformation mechanisms of collagen at the molecular and fibrillar level.

2.6 The mechanical properties and deformation mechanisms of collagen at the molecular and the fibrillar level

A summary of the elastic modulus and deformation mechanism of collagen at different hierarchical levels is provided in Table 2.2.

Development of experimental as well as computational techniques have enhanced our understanding of collagen deformation and elastic properties from the molecular and subfibrillar level (Molecular dynamics; (Buehler, 2008; Gautieri et al., 2011)) to the fibrillar level of collagen (Experiments; (Heim et al., 2006; Eppell et al., 2006; van der Rijt et al., 2006)).

2.6.1 Mechanical properties at the molecular level of collagen

The close packing (Beck and Brodsky, 1998) of the triple helix promotes the formation of hydrogen bonds (H–bonds) between α–chains, as illustrated in Figure 2.13A. Based on molecular dynamics, Gautieri et al. (2009a) have studied the mechanical behaviour and deformation mechanisms of segment of a collagen molecule under tensile force (loading force parallel to the long axis of the molecule).

At strains lower than 10% the collagen molecule rotates resulting in the formation of more H–bonds. The increasing amount of H–bonds results in a non–linear increase of the resulting force, needed to break the H–bonds (10 to 20% of strain). Beyond this point, stretching of the backbone structure, which is supported by strong covalent bonds, results in a further non–linear increase of force versus strain (Gautieri et al., 2009a).

Harley et al. (1977) obtained the elastic modulus data of collagen molecules from rat–tail tendon by means of Brillouin scattering spectra. The authors suggested an elastic modulus of 9 GPa. Further studies, based on Brillouin scattering spectra, suggested a lower elastic modulus, of 5.1 GPa, for the hydrated collagen molecule (Cusack and Miller, 1979). This results are corroborated from more recent findings on elastic modulus of collagen molecule, ≈7 GPa, based on computational methods (molecular dynamics) (Buehler, 2006).

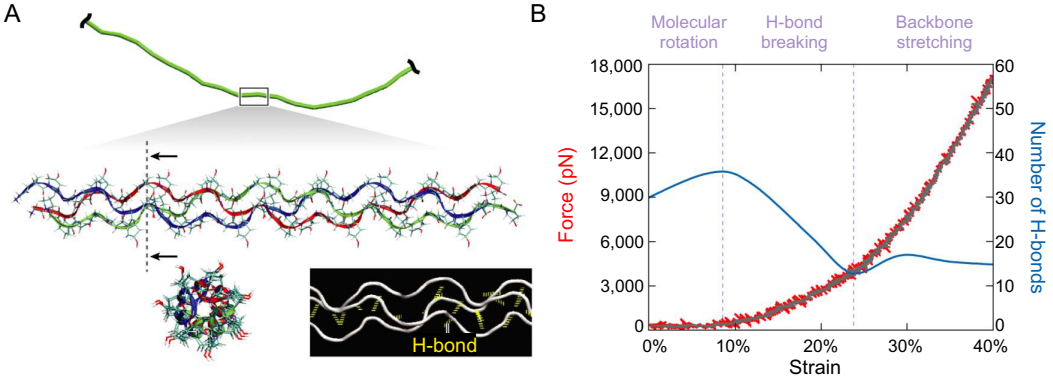

Figure 2.13: (A) A portion of the collagen molecule (green line) is magnified to reveal the right–handed coil of the triple helix. The backbone of the three α–chains is coloured in green, red and blue. (Black–background panel)Inter–chain hydrogen bonds stabilize the triple helix of collagen molecule. (B) Number of hydrogen bonds as a function of strain while extending a molecule. Reprinted from Launey et al. (2010) with permission. Copyright (2010) Annual Reviews.

Collagen hierarchical level	**Maximum strain**	**Deformation & failure mechanisms**	**Elastic modulus**
Single molecule, *molecular dynamics* (Buehler, 2006)	≈40%	H–bond breaking, backbone stretching	≈7 GPa
Microfibril, *molecular dynamics* (Gautieri et al., 2011)	≈25% (wet), ≈10% (dry)	Molecular straightening, stretching and sliding	0.3–1.2 GPa, 1.8–2.3 GPa (dry)
Fibril, *AFM* (Svensson et al., 2013)	≈20% (wet)	Molecular straightening and sliding, Possible breaking of inter–molecular cross–linking	2.2–5.7 GPa (hydrated)
Fibre (Misof et al., 1997a)	≈16% (wet)	Inter–fibrillar sliding, breaking of inter–molecular cross–links	Max stress ≈0.1 GPa (hydrated)

Table 2.2: Deformation and failure mechanisms of collagen at different hierarchical levels.

2.6.2 Mechanical properties at the fibril level of collagen

Gautieri et al. (2011) have recently investigated the deformation mechanism of the collagen microfibril (Orgel et al., 2006) by means of molecular dynamics. Gautieri et al. (2011) used full length, ≈300 nm, collagen molecules with their non–helical telopeptides attached at the ends of each molecule implemented in the microfibril unit cell of collagen as proposed by Orgel et al. (2006). At small strains, the disordered segments, or also termed as kinks, of the collagen molecules at the gap regions of the microfibril are aligned and straightened parallel to the direction of the tensile force. This deformation mechanism has also been suggested by Fratzl et al. (1998) based on synchrotron x–ray scattering on tendon sections. The force needed to straighten the molecular segments of collagen at the gap regions is lower compared to the force needed to stretch the backbone structure, which is stabilized by strong inter–atomic covalent bonds. At strains >20%, higher forces transmit causing stretching of the backbone structure of the collagen molecule and also inter–molecular sliding, Figure 2.14.

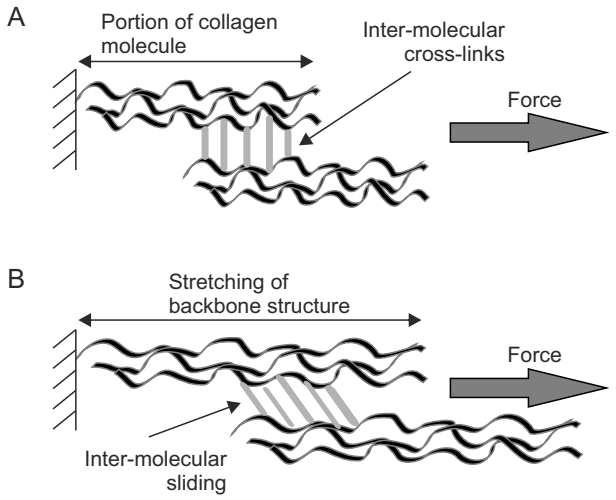

Figure 2.14: At >20% strains the backbone structure of collagen molecule stretches. This deformation mechanism is accompanied by inter–molecular sliding. Portion of the collagen molecule is illustrated with ribbon and the inter–molecular cross–links with grey thick lines. The direction of the applied force is parallel to the longitudinal axis of the collagen molecules and therefore the collagen fibril.

Experimental studies were focused on determining the elastic modulus of individual collagen fibrils under different loading scenarios. These include tensile loading employing microelectromechanical systems (MEMS) (Eppell et al., 2006; Shen et al., 2008) and atomic force microscopy (AFM) (van der Rijt et al., 2006; Svensson et al., 2010); three–point bending employing AFM (Yang et al., 2007); and AFM cantilever–based nanoindentation (Heim et al., 2006; Wenger et al., 2007; Grant et al., 2008). Tsthe elastic modulus determined by these studies varied from 1 MPa to 15 GPa. The loading case scenarios, the experimental and loading conditions, the hydration state of the samples,

the tissue origin and the state of cross–linking may all play a significant role on the measured elastic modulus. Table 2.3 summarizes the elastic modulus of collagen fibrils determined with the various experimental techniques and loading scenarios mentioned above.

Approach	**Loading scenario**	**Origin, Collagen type I**	**Elastic modulus**
X–ray diffraction (Gupta et al., 2004)	Tensile	Turkey leg–tendon	1 GPa
MEMS (Eppell et al., 2006; Shen et al., 2008)	≫	*Cucumaria frondosa*	0.84 ± 0.45 GPa (low strains), 6 GPa (high strains)
AFM (van der Rijt et al., 2006)	≫	Bovine Achilles tendon	5 ± 2 GPa (dry), 0.2 ± 0.5 GPa (hydrated)
AFM (Yang et al., 2007)	Bending	Bovine Achilles tendon	1 to 25 GPa (dry, values depend on boundary conditions), 60–70 MPa (hydrated)
AFM (Heim et al., 2007)	≫	*Cucumaria frondosa*	10 5 GPa (dry)
AFM (Heim et al., 2006)	Indentation	*Cucumaria frondosa*	1 to 2 GPa (dry)
AFM (Wenger et al., 2007)	≫	Rat tail tendon	5 to 15 GPa (dry)
AFM (Grant et al., 2008)	≫	Bovine Achilles tendon	1.9 ± 0.5 GPa (dry), 1.25 ± 0.1 MPa (hydrated)

Table 2.3: Elastic modulus of collagen type I measured in tension, bending and indentation under different loading conditions.

Collagen fibrils are often modelled as isotropic materials (Yang et al., 2007; Grant et al., 2008), but they are recognized to be transversely isotropic due to the high aspect ratio of collagen molecules (≈1.5 nm in diameter and ≈300 nm in length) that are oriented along the longitudinal axis of the fibril. The anisotropy in the collagen fibril structure has been supported by evidence of the non–uniform shape of residual imprints produced by AFM cantilever–based nanoindentation (AFM–cbN) (Wenger et al., 2007), shown in Figure 2.15. The longitudinal elastic modulus of collagen fibrils has been found to be about 300 MPa (van der Rijt et al., 2006) (hydrated collagen fibrils from Bovine Achilles tendon). Although, direct compression tests have not been conducted on collagen fibrils to provide with transverse elastic modulus data, the elastic modulus was found to be 1.25 MPa by employing AFM cantilever–based nanoindentation experiments. From this point onwards I will refer to indentation modulus as the elastic modulus determined by applying indentation–type loading to discriminate it from the transverse elastic modulus (which is determined by employing compression experiments). Grant et al. (2008) have measured a much lower indentation modulus, by employing AFM–cbN, of about 1.25 MPa, compared to the longitudinal elastic modulus of 300 MPa reported by van der

Rijt et al. (2006). Additionally, the indentation modulus of bone, which possesses an anisotropic structure, has been suggested to be influenced by both the longitudinal and transverse elastic modulus (Rho, 1996; Swadener et al., 2001).

During axial loading, the deformation mechanisms may involve straightening, stretching and sliding of collagen molecules. During indentation–type loading, is most likely that straightening may not occur, although collagen molecules may separate and compressed during the indentation of the AFM tip. The difference between longitudinal elastic modulus and indentation modulus is most likely because of the different deformation mechanisms as a result of the structural anisotropy of collagen fibrils.

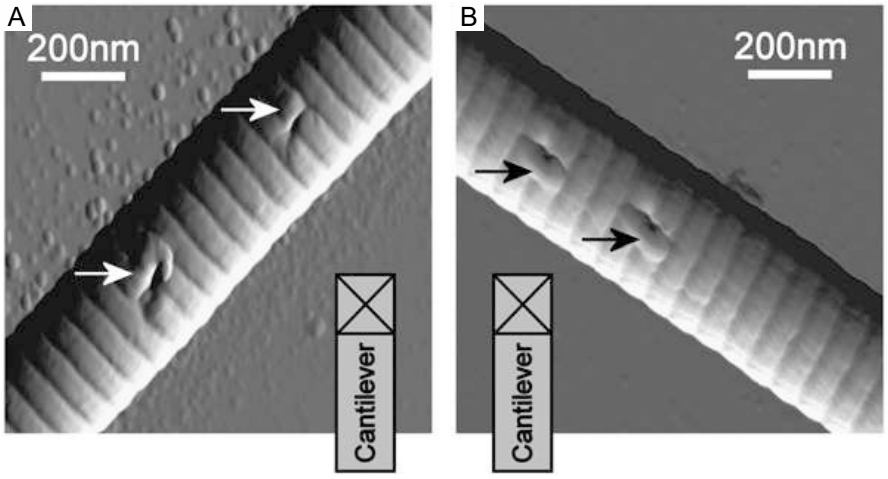

Figure 2.15: Non–uniform shape of residual imprints (arrows) from indentation–type loading on the surface of two similar collagen fibrils with different orientation in respect to the AFM cantilever. Reprinted from Wenger et al. (2007) with permission. Copyright (2007) The Biophysical Society.

2.7 Changes in cross–linking, mechanical and structural properties of collagen in healthy tissues and pathology

2.7.1 Ageing–related changes

The cross–linking of collagen fibrils evolves overtime, as mentioned in section 2.3. Based on bovine skin collagen, Bailey and Shimokomaki (1971) observed a decrease in immature cross–linking with ageing while mature cross–linking increased. This implied that the mature cross–links and non–enzymatic ones (or advanced glycation end products – AGEs) were responsible for the tissue structural and mechanical integrity. Later, Bailey (2001) showed that the stiffness and strength increased with age, in rat tail tendon. These studies were carried out on different systems (i.e. collagen from bovine skin and rat tail tendon) with different development rates. Figure 2.16 presents the results from Bailey and Shimokomaki (1971) and Bailey (2001).

Cross–linking evolved over a period of 6 years, in collagen from bovine skin (Bailey and Shimokomaki, 1971). The strength and stiffness increased over a period of 24 months, in rat tail tendon (Bailey, 2001). Although, the ageing disparity between bovine skin and rat tail tendon, the results suggest that the mechanical properties at the tissue level are associated with the cross–linking at the collagen fibril level. However, little is known about the direct effect of cross–linking at the collagen fibril level.

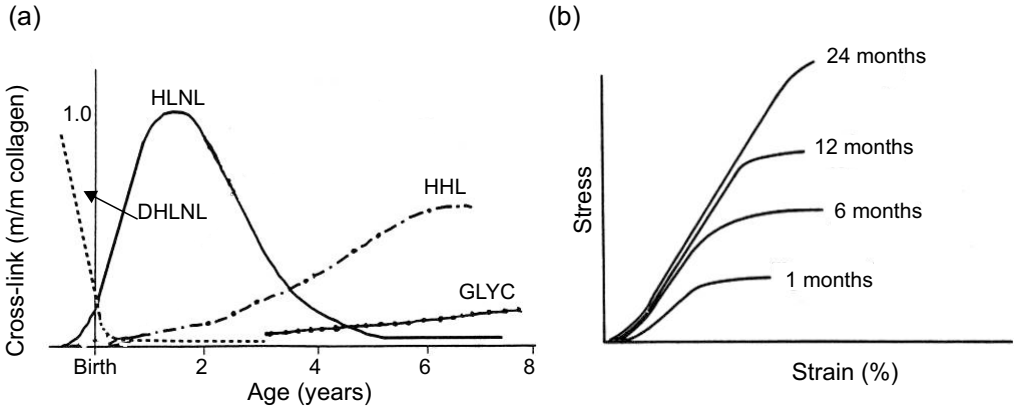

Figure 2.16: Cross–link and stiffness changes with age. (a) Collagen cross–link type of bovine skin collagen changes with age. The immature divalent DHLNL (hydroxylysinonorleucine) cross–links decrease with an increase of the immature HLNL (dihydroxylysinonorleucine). At about 1 year, the decrease in HLNL is followed by an increase in the mature trivalent HHL (histidino-hydroxlysinonorleucine) cross–links. At about three years there is also an of the glucose–related cross–links (hexosyl-lysine and GLYC) with a parallel increase of the mature trivalent HHL (histidino-hydroxlysinonorleucine) cross–links. (b) The strength (maximum stress) and stiffness (slope of linear region) of rat tail tendon increases with age. Adapted from Bailey (2001) with permission. Copyright (2001) Elsevier Science Ireland Ltd.

2.7.2 Changes in pathology: osteogenesis imperfecta and asthma

2.7.2.1 Osteogenesis Imperfecta

Mutations in the the COL1A1 and COL1A2 genes are the primary cause of bone fragility in osteogenesis imperfecta. COL1A1 and COL1A2 genes encode the type I α1– and α2–chain, respectively.

In humans, these mutations result in substitution of Glycine residues by other amino acids (Byers et al., 1991; Prockop, 1995). Such structural changes at the molecular level could potentially affect the structure and therefore the mechanical function of collagen fibrils (Gautieri et al., 2009b). Gautieri et al. (2009c), based on molecular dynamics, showed that substitution of Glycine residues decreased the longitudinal elastic modulus of collagen molecules. Further studies by (Gautieri et al., 2009b) suggested an

increase in the intermolecular equilibrium spacing. With increased intermolecular spacing and structural the cross–linking is most likely to be affected. (Gautieri et al., 2009b) suggested decreased cross–link density at the fibril level of collagen from osteogensis imperfecta.

A number of mice models present similar phenotype with osteogenesis imperfecta in humans (Kamoun-Goldrat and Le Merrer, 2007). From these mice models, the *oim* mouse simulates moderate to severe cases of ostegenesis imperfecta (Chipman et al., 1993).

The *oim* mouse model does not express the COL1A2 gene and therefore the the α2(I)–chain is not synthesized. In absence of α2(I)–chains, homotrimer collagen molecules are formed in favour of thermal stability (Kuznetsova et al., 2003). Chang et al. (2012) suggested that the type I homotrimeric (homotrimer) collagen molecule is characterized by more unfolded regions and kink formations than the type I heterotrimeric (heterotrimer). In addition, these authors showed that the type I homotrimeric collagen molecule is more flexible due the kink formations (Chang et al., 2012). By applying tensile loading on both the heterotrimeric and homotrimeric collagen molecules, Chang et al. (2012) obtained the stress–strain behaviour the collagen molecules. Figure 2.17 compares the structural conformation and stress–strain behaviour between heterotrimeric and homotrimeric collagen molecules.

The aforementioned studies show the effects of the mutation in COL1A2 gene on the structure and mechanical properties of collagen molecules. At the tissue level, the lateral packing of collagen fibrils in *oim* tendon found to be altered (McBride et al., 1997). In *oim* bones, the toughness is decreased by 50% and the stiffness by 33% (Miller et al., 2007).

All of the above studies suggest that the *oim* mice has distinct structural and mechanical changes at the molecular level of collagen. These changes in *oim* mice affect the structure–mechanical function at the tissue level of collagen, in the case of tendon (McBride et al., 1997; Misof et al., 1997a), and of bone. The above suggests that the structure–mechanical function of *oim* collagen fibrils is altered. However, such alteration at the fibril level of *oim* collagen have not been studied to date.

2.7.2.2 Asthma

Diagnosis of asthma

Asthma is a long term respiratory disorder. It is characterized by airway wall inflammation, obstruction and remodelling. These features eventually lead to decreased lung function. The ability of bronchial constriction and dilation is two of the. Lung funtion is assessed by employing spirometry tests that measure the volume of inhaled and

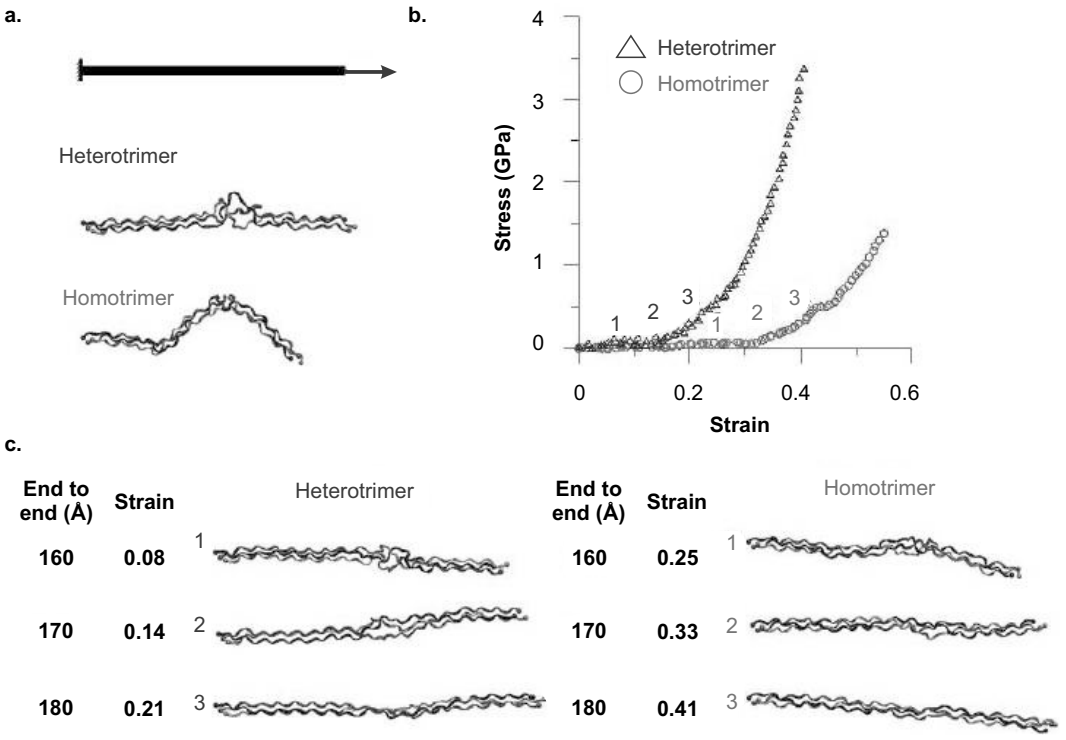

Figure 2.17: Stress–strain behaviour of heterotrimeric (wt) and homotrimeris (*oim*) collagen molecules under tensile loading. (a) Illustration of tensile loading on collagen molecule. (b) Stress–strain curve of heterotrimer and homotrimer collagen molecules. Homotrimer collagen appears softer compared to heterotrimer. The homotrimeric has larger entropic elasticity (stresses less than 100 MPa) due to local kink formations. These local kinks result in lower end to end distance and homotrimer appears more flexible compare to heterotrimer collagen molecules. (c) Strain level of homotrimer are about twice as much as the ones observed in heterotrimer for the same applied stresses. Reprinted from Chang et al. (2012) with permission. Copyright (2012) Biophysical Society.

exhaled air and the air flow rate. The total volume of air exhaled (Force Vital Capacity; FVC) and the volume of air exhaled at the first second (Forced Expiratory Volume in 1 seceond; FEV1) are the most common measurements that assess lung function. Such measurements cannot be an explicit indicator of diagnosis of asthma. Diagnosis is accomplished in combination with other tests. These include airway responsiveness, inflammation and allergy tests.

Remodelling features in asthmatic airways

The most common feature of asthma is thickening of the airway wall. Airway wall thickening results from impaired remodelling of the airways and has been associated with inadequate bronchoconstriction and bronchodilation (Tschumperlin et al., 2003). Holgate et al. (2010) suggested the hypothesis that the mechanical strain caused by

repeated smooth muscle contraction is associated with progressive deposition of extracellular matrix proteins (Black et al., 2003). This could initially increase the stiffness of the subepithelial layer to prevent narrowing of the lumen (James et al., 1989; Holgate et al., 2010). In the long term, excessive extracellular matrix deposition could be responsible for airflow obstruction, characteristic feature of impaired lung function in chronic asthma (Holgate et al., 2010).

In addition, changes in the structural and mechanical properties of the extracellular matrix could affect lung mechanobiology (Tschumperlin et al., 2003). Over the last decade, support the hypothesis of altered cell behaviour due to changes in the elastic modulus and stiffness of the matrix, on which cell are embedded (Pelham and Wang, 1997; Lo et al., 2000; Yeung et al., 2005; Discher et al., 2005; Engler et al., 2006; An et al., 2009). Fibroblasts, collagen producing cells, from asthmatics increased collagen deposition (Roche et al., 1989) and accumulated in the tissue (Nihlberg et al., 2006) compared to fibroblasts from non–asthmatic.Figure 2.18 illustrates an artistic impression of the changes in the airways wall of asthmatic compared to non–asthmatic (normal) ones.

[!htb]

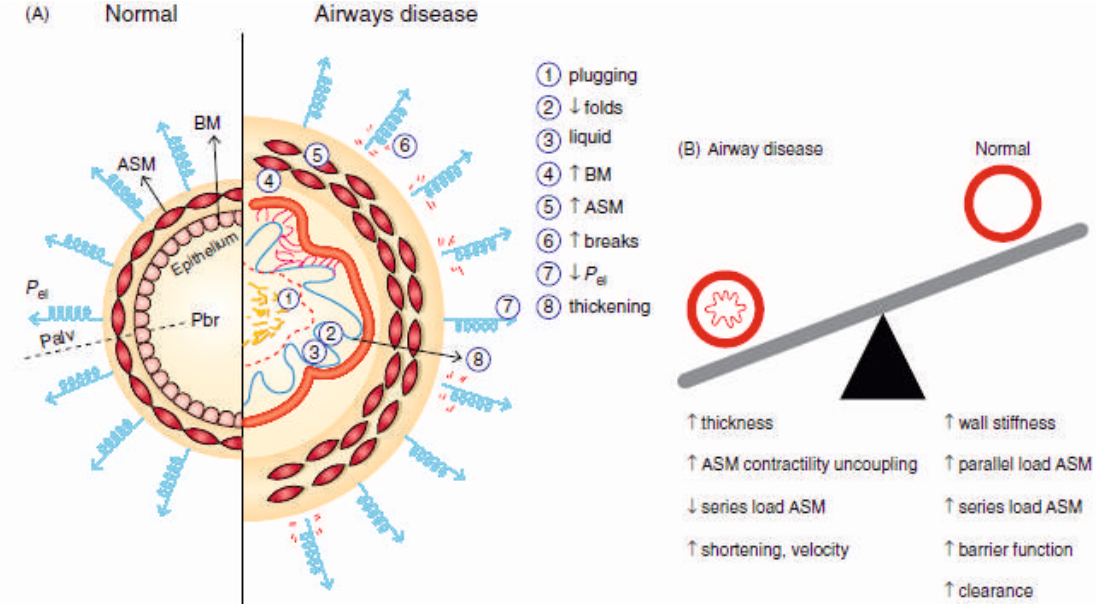

Figure 2.18: (A) Schematic representation of the cross–section of the bronchial airway in a normal and an asthmatic individual. Aberrations that occur in asthmatic airways include: (1) Plugging of the airways with debris, (2) decrease in number of mucosal folds (Lambert, 1991), (3) liquid in luminal folds of epithelium, (4) thickening of the basement membrane (Ward et al., 2002), (5) airway smooth muscle contractility and size increases, (6) rise of alveolar , (7) reduced elastic recoil, (7) airway wall thickening. Pel: forces of elastic recoil; Palv: alveolar pressure; Pbr: pressure in the lumen of the bronchiole; ASM: airway smooth muscle. Reprinted from Irvin (2009) with permission. Copyright (2009) Elsevier Ltd.

To date, the stiffness of the subepithelial layer and its structural elements has not, to the best of our knowledge, been investigated. Understanding the mechanics at the nanoscale and macroscale of these tissues as a consequence of both structural and biochemical changes will provide further insights on the underlying mechanisms in asthma and potentially other lung disease characterized by impaired function.

2.8 Motivation for nanomechanical assessment of biological materials

A number of studies investigated the mechanical properties of bones from ostegenesis imperfecta. Researchers employed experiments to understand the effects of ostegenesis imperfecta in human bones (Vetter et al., 1991; Traub et al., 1994; Rauch et al., 2005; Folkestad et al., 2012) and other researchers on *oim* mice bones (Fratzl et al., 1996; Miller et al., 2007; Vanleene et al., 2012). Additionally, researchers studied the structure and mechanics of collagen molecules and mice tail tendon sections. However, there are studies on the structural and mechanical properties of *oim* collagen fibrils. In addition to osteogenesis imperfecta, the multiple mechanical and structural features of asthmatic airways have been investigated at the tissue level. Similarly, the mechanical properties collagen fibrils from asthmatic airways are yet to be understood.

Assessing the mechanical properties at the fibril level of collagen becomes important because of the changes occurring at this level. Additionally, collagen fibril samples can readily be prepared with minimum sample preparation making this system easy to access. Investigating the mechanical properties can provide a better understanding of the development of collagen–related diseases. In tissue engineering, this could further help manufacture grafts with properties that match the targeted replacing tissue. Potentially this would provide the basis of novel treatment development for collagen–related diseases (Prockop and Kivirikko, 1984; Myllyharju and Kivirikko, 2001).

Beyond understanding the development of diseases and provide novel treatment, nanomechanical assessement of collagen fibrils could provide measurements to validate current models in the toughening mechanisms of bone (Gupta et al., 2006). Finally, basic insight into the structure–function relationships can be gained by linking collagen structure and cross–linking to its mechanical properties.

Several techniques have been used to assess the mechanics of collagen fibrils, such as microelectromechanical systems, *in situ* tensile with x–ray diffraction and atomic force microscopy (AFM). The versatile capability of AFM has made the technique popular. AFM has been widely used to assess the mechanical and structural properties at the nanoscale because of its ability to image and directly assess the mechanical properties of structures at the nanoscale in both dry and hydrated conditions. The following chapter

(Chapter 3) discusses the principles of AFM and the nanomechanical assessment of collagen fibrils by employing atomic force microscopy cantilever–based nanoindentation.

Chapter 3

Atomic force microscopy imaging and nanoindentation experiments

3.1 Atomic force microscope

The atomic force microscope (AFM) is a member of a family of microscopes known as the scanning probe microscopes (SPM).

Scanning probe microscopy began in the '80s when Binnig and Rohrer (1983) invented the scanning tunnelling microscope (STM). The impact of their invention was great in surface sciences and, Binnig and Rohrer were awarded the Nobel prize in 1986. The same year Binnig et al. (1986) announced the invention of the new member of the SPM family, the atomic force microscope (AFM).

The microscopes of the SPM family resolve the surface of specimens by "feeling" rather than by "looking". The conventional far field microscopes visualize the surfaces by collecting the reflected or transmitted radiation from the sample. The electron microscopes generate images of the surface using high energy electrons. The SPMs measure the interaction between a sharp probe and the sample surface while the probe scans the surface. The changes in the magnitude of the interaction between the probe tip and the surface of the sample are used to obtain SPM images. Therefore, the resolution of the SPM microscopes depends on the probe tip sharpness and the accuracy of the probe positioning relative to the sample.

3.2 The basic compartments of an AFM

Figure 3.1 is an artistic impression of the basic compartments of an AFM. The basic compartments are (i) the cantilever and tip, (ii) the piezoelectric transducers and (iii)

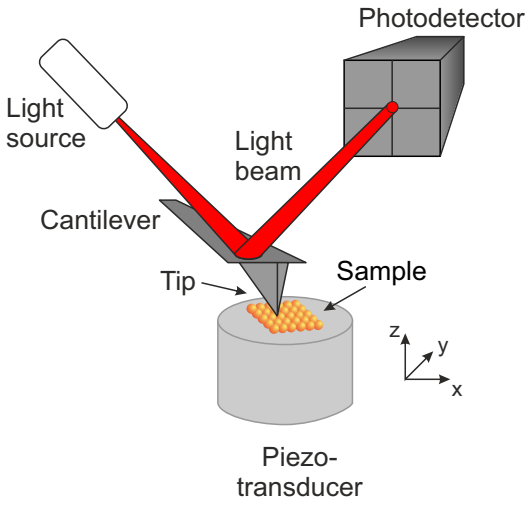

Figure 3.1: A light beam, generated from the light source, reflects off a cantilever and finally hits on a photodetector. The cantilever bends due to topographical changes of the sample surface causing a movement of the light spot on the photodetector.

the components of the detection method.

3.2.1 The AFM cantilever and tip

The AFM cantilever is a microfabricated structure and can be found a number of geometrical features. The most common cantilevers are rectangular and triangular. The triangular AFM cantilevers are termed as V–shaped. Figure 3.2 shows optical images of a rectangular and a V–shaped AFM cantilever. In addition, AFM cantilever have stiffness values from 0.006 N/m to 85 N/m depending on the geometrical characteristics of the cantilever (lenght, width, thickness). Softer AFM cantilevers are used to image softer samples and provide high resolution being sensitive to small changes in the topography. Similarly, stiffer AFM cantilevers are used to probe the topography of stiffer samples.

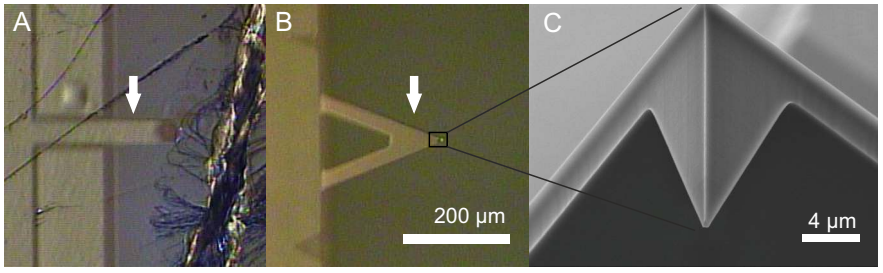

Figure 3.2: Optical image of a rectangular, shown in panel A, and a V–shaped AFM cantilever, shown in panel B.

The AFM tip is a sharp spike microfabricated on the edge of the AFM cantilever. The AFM tip ranges in geometry and size. The most common AFM tips are three–sided (as shown in panel C of Figure 3.2) and four–sided pyramids, with tip radius that varies from 5 nm to 100 nm and tip height from 3 μm to about 20 μm. The choice of AFM tip is closely related to the geometrical features of the surface of the sample. This is because the AFM tip radius, height and side wall angles can considerably affect the AFM image. The resulting topographical feature is a convolution of the geometry of the AFM tip and the geometry of the topographical feature. The most common convolution effect between the AFM tip and the sample is the "envelope" effect (Ricci and Braga, 2004). The "envelope" effect is an artefact observed on the lateral direction of the sample, as illustrated in Figure 3.3.

Consequently, recording the width is not a reliable measurement of the radius of a cylindrical or a spherical feature. Such measurements are overestimations of the actual width, and thus the radius. In this case, recording the height provides more accurate measurements. However, artefacts in height measurements could also result from the compressibility of the sample (Allen et al., 1992), or due to adhesion of the AFM tip on the surface of the sample (Van Noort et al., 1997).

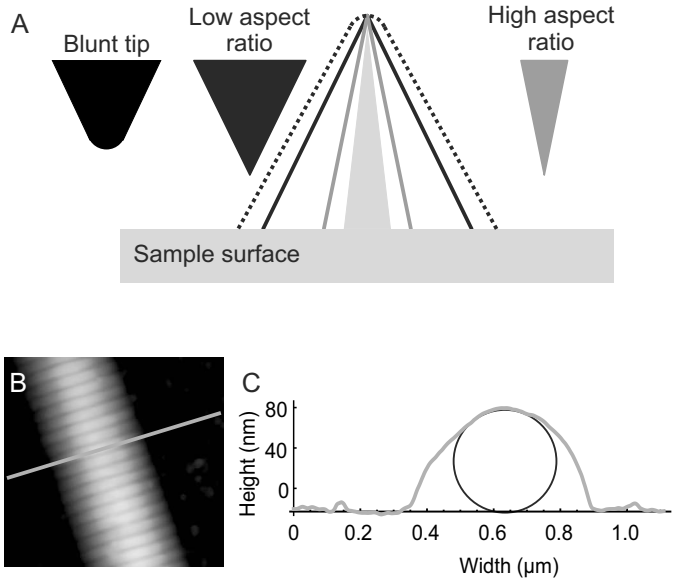

Figure 3.3: (A) Traces resulted from a blunt AFM tip (dashed trace) and from tips with low (black solid trace) and high (grey solid trace) aspect ratio. (B) AFM height image of a type I collagen fibril from wild-type mouse tail tendon and (C) the corresponding profile of the cross-section (grey line) compared to a perfect circle which is assumed to be the actual cross-section of the collagen fibril.

3.2.2 The piezoelectric transducers

The scanning mechanism of AFMs relies upon piezoelectric transducers. The *piezoelectric effect* is the generation of potential difference across the opposite faces of a non–conducting crystal, known as piezoelectric crystal, as a result of the application of external stress. The opposite effect is called *reverse piezoelectric effect* and is the one that AFM scanners employ to scan the surface. By applying voltage the piezoelectric scanner moves to preferred directions allowing the surface to move relatively to the position of the AFM tip.

3.2.3 The detection method

The detection method is divided into two main categories: the optical and the electronic. The *optical detection methods* are then divided in (i) the light beam deflection and (ii) the interferometry method. The *electric detection methods* are divided in (i) the electron tunnelling, (ii) the capacitance and (iii) the piezoelectric cantilevers. Here I will discuss the optical methods and mostly the interferometry detection method.

3.2.3.1 The light beam deflection

The simplest detection method is the light beam deflection method. A light beam reflects off the back of the probe and hits on a photodetector, as illustrated in Figure 3.4. The photodetector is a photodiode, a semiconductor device turning light into an electrical signal. The lighter the beam the more electrical signal is generated. The photodetector in equally segmented into four quadrants, each of which generates a voltage proportional to the amount of the incident light. Therefore and simplified, the deflection that occurs due to topographical changes of the surface is given as the difference in voltage generated in the top and bottom halves of the detector.

3.2.3.2 The interferometry method

The interferometry detection method used an optical interferometer in the optical path of the light beam. The incident light passes through the optical interferometer and splits into two light beams. The one reflects off the backside of the AFM probe and the other travels towards the photodetector. This approach leads a phase change between the reflected beam and the one that travel towards the photodetector. The phase shift represents the relative displacement of the AFM cantilever. This approach advances over the light beam deflection method due to the high signal to noise ratio and also because of its ability to resolve larger geometrical features

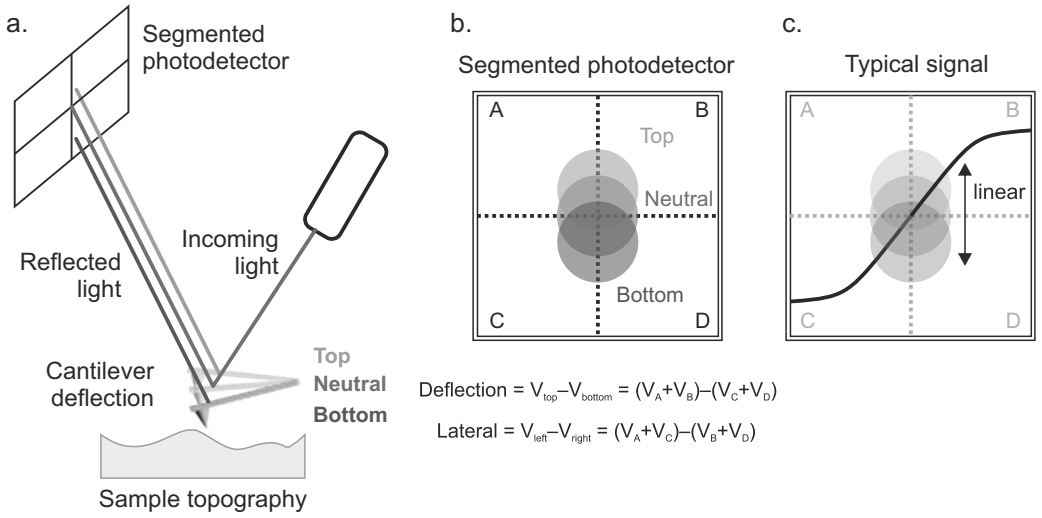

Figure 3.4: The incoming light beam reflects off the deflected cantilever (a). The reflected beam hits on a segmented photodetector and changes position as the cantilever moves vertically (a,b). This results to a typical signal which is linear at ±2.5 Volts (c).

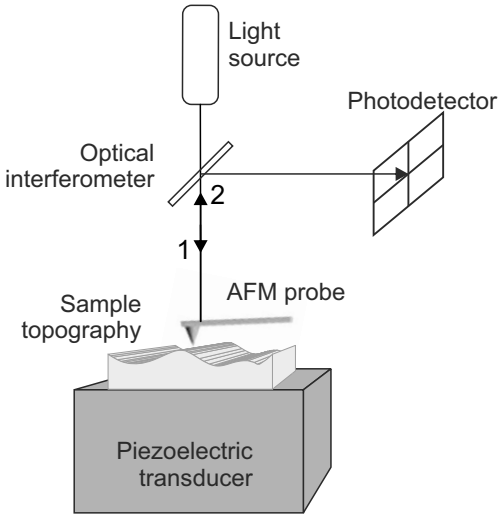

Figure 3.5: The incident light passes through the optical interferometer and splits into two light beams. The one reflects off the backside of the AFM probe and the other travels towards the photodetector. This approach leads a phase change between the reflected beam and the one that travel towards the photodetector.

3.3 Feedback loop and the basic AFM imaging modes

The AFM scans the region of interest on the surface of the sample in a raster fashion. The sample or the AFM tip covers a line aloing the x direction and then moves in the y direction to cover the next x line and so on. While scanning, the AFM tip encounters changes in the topography of the surface and the cantilever begins to bend. At this

point, a signal is generated which aims to maintain the deflection of the AFM cantilever constant to a predefined (by the user) level, the set point. The signal is fed back to a control system which adjusts the piezoelectric transducer in the z direction between the surface and the tip accordingly to maintain the deflection at the set point level. The AFM image is generated by plotting the z correction distance against the x and y directions, resulting in a three dimensional perspective of the surface of the sample.

Below, the feedback loop operation and the three basic AFM imaging modes are described.

3.3.1 Feedback loop

The most basic form of control system in feedback loop operation is the on–off control. The on–off control is unable to achieve the set point level. Instead, the signal oscillates around the set point level. This control operation is undesirable during AFM imaging. To achieve an accurate control operation, mathematical terms are added to the control signal; the proportional (P), the integral (I) and the derivative (D).

To establish a size of the correction signal, the proportional control amplifies the error between the set point and the measured value by defining a proportional band, as shown in panel B of Figure 3.6. The proportional band is a percentage of the total span of the controller. The actual percentage is the gain of the system. For example, the proportional gain is 5 when the proportional band is 20% and a gain of 20 corresponds to 5% proportional band. The higher the gain the smaller the proportional band. The size of the band determines the magnitude of the response of the controller. The proportional control results in an offset of the signal from the actual set point, as shown in panel B of Figure 3.6. The offset can, in theory, be minimized by increasing the proportional gain. However, this results to an unstable (oscillation) response of the controller.

The integral term integrates the deviation from the set point over a period of time removing, in this way, the offset. The time period is limited by the time response of the piezoelectric scanner. It the time is made too small then oscillation will occur and the response is unstable.

The derivative term is applied to reduce the tendency of the controller to erratic behaviour. Although the derivative control helps to achieve stability, an excessive derivative gain may cause instability. For this reason, it is most often not used and set to zero.

3.3.2 Contact mode

In contact (DC) mode, the AFM tip is brought into direct contact with the surface of the sample, resulting in a repulsive interaction between the AFM tip and the sample.

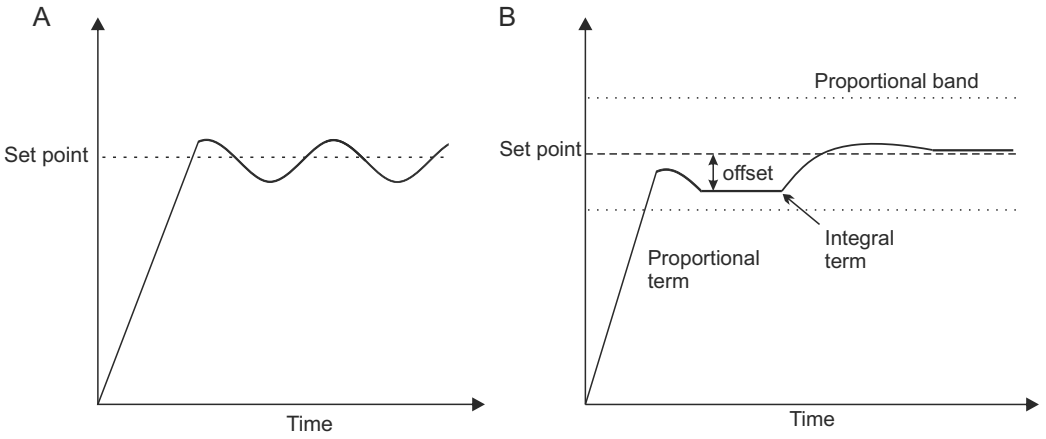

Figure 3.6: The on–off control operation is unable to achieve the set point level (panel A). The limitation is overcome by applying mathematical terms to the control signal. The response of the controller after applying a proportional and an integral term is shown in panel B.

The AFM cantilever maintains a constant deflection over the sample, i.e., a constant force is applied on the surface of the sample. The larger the deflection of the cantilever is, the higher the applied force on the surface of the sample. Increasing the force could cause damage on the surface or contaminate the AFM tip with biological tissue.

AFM imaging in contact mode of collagen fibrils can be achieved in both dry and under liquid employing AFM cantilevers with stiffness of about 0.5 N/m. Stiffer AFM cantilevers are not appropriate for imaging soft biological tissue, because they cause damage to the surface and the generated images have low resolution.

3.3.3 Intermittent mode

In intermittent mode, the AFM cantilever oscillates while scanning the surface of the sample (Garcia and San Paulo, 1999). The AFM tip bounces over the surface and therefore spends less time on the surface of the sample, resulting in reduction of the lateral forces. This is important for macromolecules which can be imaged with minimum distortion. In addition, the AFM tip is trapped in the water film, present on dried surfaces. This reduces artefacts due adhesion caused by the capillary forces. Intermittent mode can also be employed in both dry and under liquid.

3.3.4 True non–contact mode

In the true non–contact mode, the AFM tip never contacts the surface of the sample (Garcia and San Paulo, 1999). The AFM cantilever oscillates above the surface of about 5 nm. The long range van der Waals attractive force between the AFM and the sample

produce a dampening effect on the oscillating cantilever. This results in reduction the the oscillating amplitude of the AFM cantilever when it encounters a protruding feature on the sample. This dampening effect is used by the instrument software to generate an three dimensional impression of the topography.

3.4 Nanoscale mechanical evaluation of individual collagen fibrils

The AFM images are generated on the bases of force interactions between the AFM cantilever and the surface of the sample. The force interactions can be used to assess the mechanical properties of nanostructures. To achieve this, the AFM cantilever can be used to applied load on a sample and provide with force–displacement curves.

The AFM has been extensively used to assess the mechanical properties of collagen fibrils employing a number of loading scenarios, such as tensile (van der Rijt et al., 2006; Svensson et al., 2010), three–point bending (Yang et al., 2007) and indentation (Heim et al., 2006; Grant et al., 2009; Wenger et al., 2007). Figure 3.7 illustrates the tensile and three–point bending experiments carried out by employing atomic force microscopy.

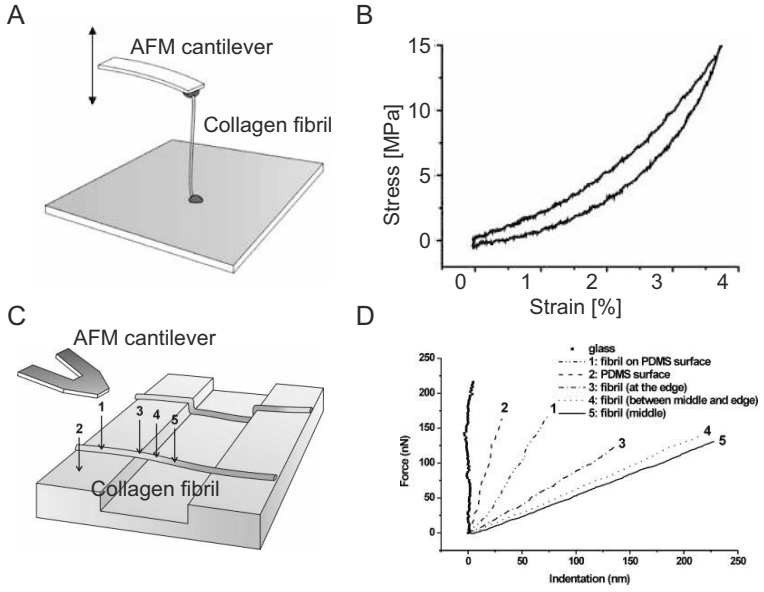

Figure 3.7: Tensile (panel A) and three–point bending (panel C) of collagen fibrils. The tensile stress–strain curve of a collagen fibrils is shown in panel B. Panel D shows a number of force–indentation (or force–displacement) curves taken at different regions on a collagen fibril. Panels A and B were adapted from van der Rijt et al. (2006) with permission. Copyright (2006) Macromolecular Bioscience. Panels C and D were adapted from Yang et al. (2007) with permission. Copyright (2007) Journal of Biomedical Materials Research.

Researchers have employed experiments directly at the fibril level of collagen with the development of MEMS and AFM. Specifically, Eppell et al. (2006) and Shen et al. (2008) have applied direct tensile loading on collagen fibrils, with diameters ranging from 150 nm to 470 nm, by means of MEMS. However, AFM has been widely used to assess the mechanics of collagen fibirls. A number of researchers, have investigated the mechanical properties and fracture under tensile loading . In brief, tensile loading of collagen fibrils with AFM has been achieved by attaching one part of a fibril with a glass slide and another with the AFM tip with epoxy resin. While retracting from the surface the cantilever bends downwards as the fibril deforms. Provided that fibril diameter is easily measured by AFM imaging, the resulting deflection vs. z–displacement data are transformed into force–displacement and therefore stress–strain.

Three point bending of collagen fibrils has also been performed by Yang et al. (2007). This has been achieved by depositing collagen fibrils on PDMS substrates with microchannels of known width and depth in the order of 5 μm and 1 μm respectively. Finally and perhaps the most frequently used technique in AFM nanomechanical assessment of collagen is cantilever–based nanoindentation (Heim et al., 2006; Grant et al., 2009; Wenger et al., 2007). This is most likely because of its ease of use and minimum sample preparation that is needed. The technique uses the AFM tip apex to indent the surface of the sample. Such experiments provide true force–indentation curves, similarly to conventional nanoindentation (Fischer-Cripps, 2012), that can be analysed to provide with the elastic modulus of collagen fibrils. AFM cantilever–based nanoindentation and the current analysis methods used in collagen fibrils mechanics research are further discussed in detail in the next section.

3.5 AFM cantilever–based nanoindentation

The hardness test performed by Johan August Brinell in 1900 is the origin of AFM cantilever–based nanoindentation (AFM–cbN). In material science, the hardness was determined by pressing an indenter on the surface of the sample and measuring the impression depth. Oliver and Pharr (2004) have refined and adapted this classical hardness to a lower scale to measure the elastic properties of thin films (about 100 μm in thickness). This technique is well known as conventional nanoindentation because the indentation depth is in therms of nanometers, although the force is in terms of microneatons. Figure 3.8 illustrates an indenter (or tip) indenting a flat surface.

In conventional nanoindentation, the projected area of contact between the indented and the sample depends on the size of the indenter. A number of indenters are available with different geometrical features (Fischer-Cripps, 2012). The Berkovich tip (indenter) is a three–sided pyramid with 65.3^o half opening angle and 100 nm tip radius, as shown in panel A of Figure 3.9. Although the small size of the Berkovich indenter, and

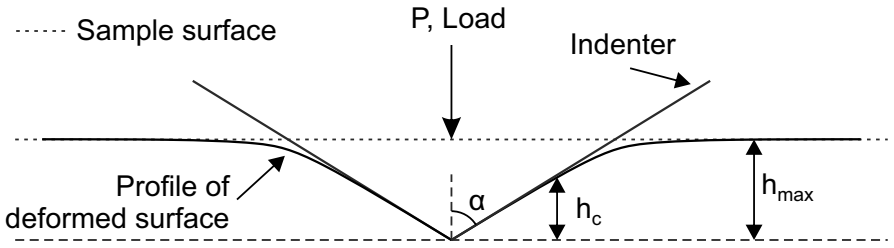

Figure 3.8: Schematic representation of a tip indenting a flat surface. h_{max}: Maximum indentation depth; h_c: Contact indentation depth; α: Half opening angle.

other indenters used in conventional nanoidentation, they cannot be used to assess the mechanical properties of collagen fibrils. Instead, the AFM tip of an AFM cantilever is used to indent biological tissues such as collagen fibrils. Figure 3.9 shows the Berkovich and AFM tips together with their projected area of contact function. The contact area function of an AFM tip apex is about 25 times smaller compared to the Berkovich one. The lower contact area function and the ability of the AFM to detect several nanometers of the cantilever deflection makes AFM tips appropriate for nanomechanical characterization of collagen fibrils of 100 nm in diameter.

During AFM cantilever–based nanoindentation, the sharp AFM tip indents the sample surface at a predefined loading rate until a maximum deflection of the cantilever is reached. At maximum deflection (i.e. force), a holding time can also be applied to allow for transition processes such as creep or stress relaxation to equilibrate. Then the tip retracts and the deflection is removed. Such an experiment results in a force–displacement curve by recording the vertical deflection and of the cantilever and the displacement in the z direction. The force is calculated by the Hooke's law:

$$Force(N) = k(N/m) * Deflection(m) \tag{3.1}$$

where k is the force constant or the spring constant or the stiffness of the AFM cantilever measure in newtons (N) per meters (m).

The indentation modulus (elastic modulus) can be determined by post analysis of the force–displacement curves, as suggested by Oliver and Pharr (2004). Calculation of the indentation modulus requires the determination of the projected area of contact at the point of contact between the tip and the sample. Below I will present the two basic analysis methods that have been used in calculations for indentation modulus of collagen fibrils.

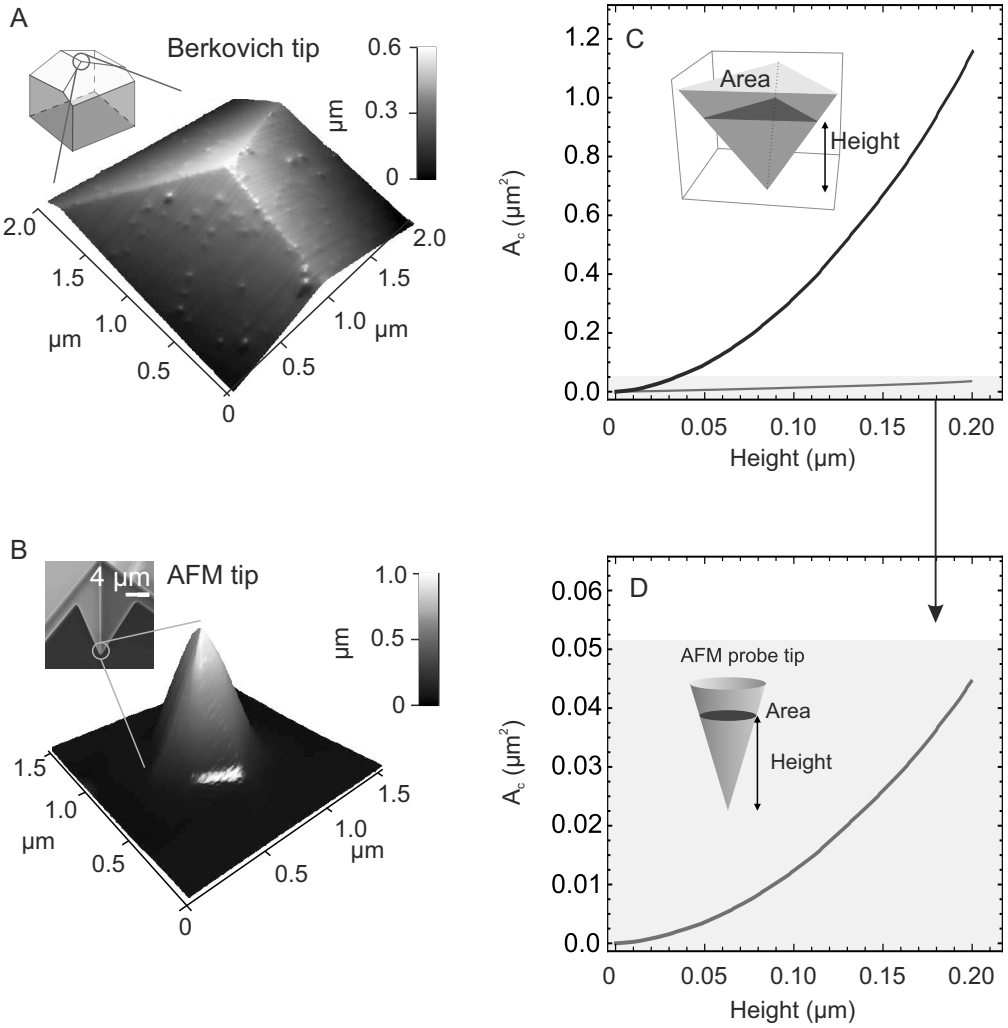

Figure 3.9: Three dimensional illustrations of a (A) Berkovich indenter used in conventional nanoindentation and a (B) tip apex of an AFM cantilever used in AFM cantilever–based nanoindentation. (C and D) The corresponding projected contact area functions of the two indenter types. Note the substantial lower contact area of the AFM tip apex compare to the Berkovich indenter.

3.5.0.1 Determination of projected area of contact

Determination of indentation modulus data requires the acquisition of projected area function of contact between the indenter and the sample. The area function of the indenter used in conventional nanoindentation is determined by direct imaging of the Berkovich tip with an AFM (Barone et al., 2010; Gadelrab and Chiesa, 2012) or by measuring the depth and geometry of the residual imprint. In the case of direct AFM imaging, the indenter must be mounted firmly and expose the tip apex towards the AFM tip. Post imaging analysis deliver the projected area function which can be expressed with a polynomial function as the one shown below:

$$A_c(h_c) = ah_c^2 + bh_c \tag{3.2}$$

where A_c is the of projected area $9m^2$) at a given depth, h_c (nm) is the contact depth and a (dimensionless) and b (m) are the fitting parameters.

The contact depth is determined by (Oliver and Pharr, 2004):

$$h_c = h_{max} - \varepsilon \frac{F_{max}}{S} \tag{3.3}$$

where the value of ε is a constant that depends on the indenter geometry. The constant ε is 0.75 for a Berkovich indenter, 1 for a flat punch, and 0.73 for cone shaped indenters.

Other analysis methods assume a spherical contact. The area function of a sphere in contact with a flat surface is given by:

$$A_c(h_c) = \pi \left(2R_{eff}h_c - h_c^2\right) \tag{3.4}$$

where R_{eff} is the effective radius of contact. In the case of individual collagen fibril indentation, the effective radius of contact is approximated by assuming contact between a sphere (tip apex) and an infinitely long cylinder (collagen fibril) which is given by:

$$R_{eff} = \sqrt{\frac{R_{tip}^2 R_f}{R_{tip} + R_f}} \tag{3.5}$$

or by assuming contact between two spheres. The effective radius of two spheres in contact is:

$$\frac{1}{R_{eff}} = \frac{1}{R_{tip}} + \frac{1}{R_f} \tag{3.6}$$

Schematics of the contact between two spheres and between a sphere and a cylinder are shown in Figure 3.10.

Equation 3.4 has been used by Wenger et al. (2007), Equation 3.5 has been used by Heim et al. (2006) and Equation 3.6 has been used by Grant et al. (2008). In addition, the analysis method used by these authors for determining the indentation modulus varies. Specifically, Heim et al. (2006); Grant et al. (2008) have used the Hertzian theory and Wenger et al. (2007) have performed the Oliver–Pharr method. These analysis methods are discussed below.

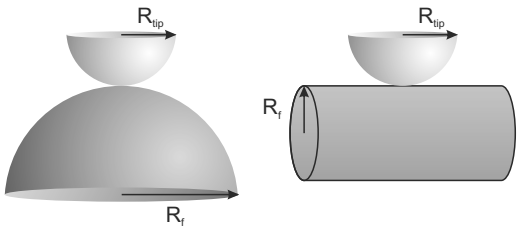

Figure 3.10: Schematics of contact between two spheres and between a sphere and a cylinder.

3.5.0.2 Determination of indentation modulus

Oliver–Pharr method:

AFM–nanoindentation experiments produce loading and unloading curves of force–displacement. The applied force is determined by Hooke's Law Equation 3.1. The z-displacement corresponds to the total vertical displacement of the cantilever towards the sample surface. Subtracting the cantilever deflection from z–displacement provides measurements of the indentation depth of the tip. The unloading part of the curves is analysed to avoid plastic contributions Oliver and Pharr (2004); Loparic et al. (2010) and values of indentation modulus were determined for each individual fibril. The unloading curve is characterized by a power law function:

$$F = m\,(h - h_0)^n \tag{3.7}$$

where h_0 is the permanent indentation depth after unloading, m (N/m^n) and n (dimensionless) are fitting parameters along with h_0 (Oliver and Pharr, 2004). The slope of the upper 75% of the unloading curve provides the contact stiffness ($S_c = dF/dh$) (Figure 3.11).

Both bodies can deform when in contact. The following equation gives the reduced modulus which takes into account deformation of both bodies:

$$E_r = \beta \frac{\sqrt{\pi}}{2} \frac{S_c}{\sqrt{A_c}} \tag{3.8}$$

where β is a dimensionless parameter that varies with indenter shape ($1.0226 < \beta < 1.085$) (Oliver and Pharr, 2004), 1.034 was used for the Berkovich tip. For AFM cantilever–based nanoindentation on collagen fibrils the correction factor was taken as 1. The reduced modulus $_r$ of two elastic bodies in contact is (Puttock and Thwaite, 1969):

$$\frac{1}{E_r} = \frac{1 - \nu_s^2}{E_s} + \frac{1 - \nu_i^2}{E_i} \tag{3.9}$$

where ν_s and ν_i the Poissons ratio of the sample and indenter respectively and E_s and E_i the indentation and elastic modulus of the sample and indenter respectively. The elastic modulus of the silicon (Hopcroft et al., 2010) AFM tip is much larger than any of the samples used in the current work ($E_i = 169$ GPa and E_s ranges from 1 to 10 GPa). In the case of $E_i \ll E_s$ Equation 3.9 takes the form:

$$\frac{1}{E_r} = \frac{1 - \nu_s^2}{E_s} \tag{3.10}$$

By substitution of Equation 3.10 in Equation 3.8 the indentation modulus of the sample is:

$$E_s = \beta \frac{\sqrt{\pi}}{2} \left(1 - \nu_s^2\right) \frac{S_c}{\sqrt{A_c}} \tag{3.11}$$

with A_c the projected area function and S_c the contact stiffness.

Hertzian theory:

Hertzian contact theory assumes pure elastic deformation between two bodies. The indentation modulus according to the Hertzian contact theory is given by:

$$E_= \frac{3F_{max}}{4\sqrt{R_{eff}}} {h_{max}}^{-3/2} \tag{3.12}$$

where F_{max} is the maximum applied load, h_{max} the maximum indentation depth and R_{eff} the effective radius. As mentioned above, the effective radius has been determined by Equation 3.5 or Equation 3.6 depending on the assumptions made for the geometry of the two bodies in contact.

In the current thesis the Oliver–Pharr method was used, as this eliminates issues with plastic deformation. Analysing the unloading part provides with the elastic properties of the test samples. To obtain true contact stiffness values, the calculated slope of the upper 75% of an indentation curve was corrected with the reference slope that indicates the stiffness of the cantilever Figure 3.11. The latter was simply subtracted from the uncorrected contact stiffness. To minimize errors amplification due to noise, during analysis, the deflection (nm)–displacement (nm) data were used. The reference slope was taken as the mean slope of ten (10) unloading curves taken on a hard surface, in this case on the glass slide next to the collagen fibril of interest. Together with the known projected contact area (Equation 3.2) the indentation modulus was calculated from Equation 3.11 assuming a Poissons ratio of 0.5 for collagen fibrils (Wenger et al., 2007; Grant et al., 2008).

On the basis of a validation study on the applicability of AFM–cbN on collagen fibrils, the data were analysed with both analysis methods (chapter 4) to show how different analysis methods change the resulting indentation modulus.

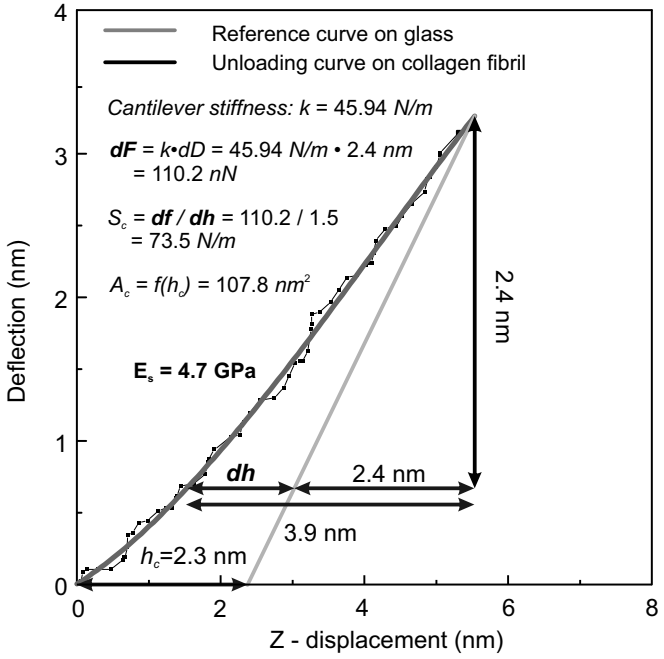

Figure 3.11: Analysing deflection versus z–displacement unloading curves recorded via AFM cantilever–based nanoindentation.

Chapter 4

Nanomechanical assessment of collagen fibrils using atomic force microscopy cantilever–based nanoindentation

4.1 Background and motivation

Continuous indentation measurements on a fused silica are performed to determine the indenter area (Oliver and Pharr, 2004). The same approach in not applicable for the determination of an AFM tip. This is mainly because the AFM tip will be damaged after a few indentation tests on the fused silica. In addition, the AFM tip will not indent on the surface of the fused silica, because of its high elastic modulus (72 GPa). Currently, a gold standard method to determine the AFM tip area function is not available. Performing a comparative study between conventional and AFM cantilever–based nanoindentation on polymer samples with known elastic modulus together with comparing different analysis tools could move one step towards a gold standard technique. One part of this study was to perform a reliability test on the determination of AFM tip area function by comparing conventional and AFM cantilever–based nanoindentation on PMMA (polymethylmethacrylate) and PP (polypropylene). The determination of the AFM tip area was accomplished by a reconstruction procedure, as suggested by Sader et al. (1999).

The other part of this study was to investigate further limitations arose from AFM–cbN on collagen fibrils. In both AFM imaging and mechanical assessment by employing AFM–cbN, the sample must be immobilized on a stiff substrate. The maximum indentation depth is limited within 10% (Bueckle's rule (Buckle et al., 1973)) of the sample

thickness (distance from the substrate). If the maximum depth is more than the 10% of the thicknes, the results vary with the indentation depth to thickness ratio (Buckle et al., 1973). The Bueckle's rule applies for all indentation instruments. However, the effect of substrate has not been investigated when testing collagen fibrils with AFM–cbN. The second part of the study was test the 10% Bueckle's rule by performing repeatable measurements with increasing applied force (i.e. indentation depth) to validate the effect of substrate on the measure indentation modulus of collagen fibrils.

The ultimate aim of this study is to investigate the applicability of AFM–cbN on collagen fibrils with substantially lower diameter from the tested to date. Collagen fibril from the bronchial airways are 30 nm in diameter with a very narrow distribution ranging from 30 nm to 40 nm.

4.2 Materials and Methods

4.2.1 Polymer samples and collagen sample preparation

4.2.1.1 Polymers

Polypropylene (PP) and Polymethylmethacrylate (PMMA) were used for both conventional and cantilever–based nanoindentation. The samples were obtained in the form of 1 mm thick sheets (GoodFellow, UK) and then cut into 10 mm x 10 mm pieces. To ensure stable sample support during data acquisition via cantilever–based nanoindentation the polymers were glued on glass slides (Agar Scientific, Stansted, UK)

4.2.1.2 Human and murine collagen fibrils

Human:

Bronchial biopsies were obtained from the primary bronchi of volunteers by fibreoptic bronchoscopy after ethical approval and informed consent. Fibreoptic bronchoscopy was performed by Prof. Peter H. Howarth[1] at the University Hospital Southampton. Collagen fibrils were extracted from biopsies by incubating the samples in separate wells for 24 hours into 0.1M Sorensens phosphate buffer (pH 7.2) containing 1 mg/ml bovine hyaluronidase and 1 mg/ml trypsin. After incubation, samples were washed with deionized water (Millipore) then placed and smeared out on glass slides to reveal areas with individual fibrils. All biological products were left in an incubator to dry in 37^oC overnight after deposition on the glass slides and then kept in a storage box with silica

[1]The Brooke Laboratories, Division of Infection, Inflammation and Immunity, Faculty of Medicine, University of Southampton, SO16 6YD, Southampton, UK.

gels. Sample preparation from human bronchial biopsies was performed by Ms Wiparat Manuyakorn[1].

Murine:

Murine type I collagen fibrils were obtained from tail tendon of a rat and a wild mouse. The harvested tail tendon was sectioned with the use of scalpel and tweezers and directly placed onto glass slide. To reveal individual collagen fibrils the sectioned tendon was smeared out on the glass slide surface with a scalpel and tweezers.

4.2.2 Nanoindentation experiments

4.2.2.1 Conventional nanoindentation on polymers

Conventional nanoindentation experiments on polymers were performed by Dr. Jurgita Zekonyte[2] and Mr. Sebastien Farbi[3].

A NanoIndenter module, attached to the head of an MFP–3D AFM (Asylum Research, Santa Barbara, CA, USA), was used for conventional nanoindentation on polymer samples.

The NanoIndenter module transforms the AFM into an instrumented indenter that uses conventional nanoindentation tips, such as the Berkovich tip. The assembly drives the indenting tip perpendicular to the surface. The displacement of the indenting flexure is performed using the z–piezo actuator and is measured from the optical deflection signal produced by the NanoIndenter module. The force is computed digitally as the product of the spring constant and the measured indenter flexure displacement. In our experiments, a low force NanoIndenter flexure was used with determined spring constant of 648 N/m, resonant frequency of 300 Hz and maximum available load of 4 mN. For nanoindentation experiments carried out on the MFP3D NanoIndenter modulus three applied loads were set Nanoindents were performed at 50 N, 500 N and 1000 N maximum load, with both loading and unloading time set to 50 sec. Holding time of 10 seconds was provided to allow creep relaxation of the polymers. In total, 20 indents were performed for each maximum force. Data acquisition and analysis were performed using IGOR Pro 6.05 software by WaveMetrics supplied together with the MFP–3D system and OriginLab respectively.

[2]National Centre of Advanced Tribology at Southampton, Faculty of Engineering and the Environment, University of Southampton, SO17 1BJ Southampton, UK.

[3]Bioengineering Science Research Group, Faculty of Engineering and the Environment, University of Southampton, SO17 1BJ Southampton, UK.

4.2.2.2 AFM imaging and cantilever–based nanoindentation

AFM experiments were performed using the MFP–3D atomic force microscope in dry ambient conditions in a temperature ((20.7 ± 0.7) ^oC) and humidity ((47.9 ± 6.7) %) controlled room. Cantilever–based nanoindentation was conducted in contact mode with the AC160 (Olympus, <10 nm tip radius and 42 N/m spring constant), AC200 (Olympus, 7 nm tip radius and 9 N/m spring constant) and with the NSC (MicroMasch, 10 nm and 40 N/m spring constant) cantilevers. The AFM images presented here were all conducted in tapping mode, with the sharper AC200 and AC160 cantilevers. Spring constant values were measured using the thermal noise method (Sader et al., 1999) and found to be about 28 N/m for the AC160, (8.3 ± 1.8) N/m for the AC200 and (44.5 ± 5.6) N/m for the NSC.

Calibrations were performed prior to experiments. In brief, the Virtual Deflection in Optical Path was calibrated by performing a force curve in air away from the stiff substrate. The slope of the curve was set as the Virtual Deflection Line value. Then the Inverse Optical Lever Sensitivity (InvOLS) was determined by performing ten force curves on a stiff surface (glass slide). The mean of the ten inverse gradients of the resulting retract signal was set as the cantilever sensitivity (Figure 4.1).

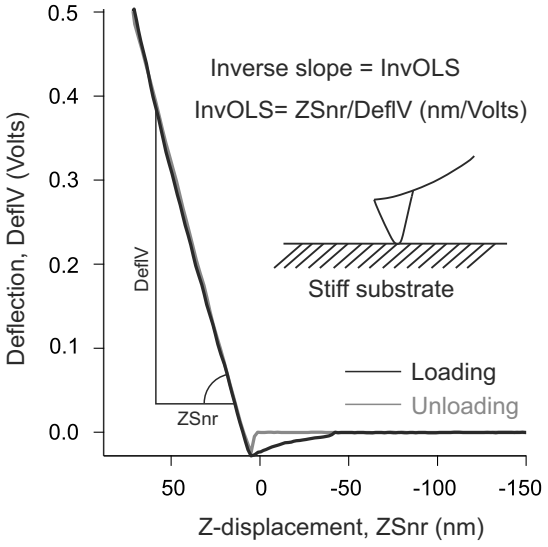

Figure 4.1: The cantilever is brought into contact and deflect over a stiff flat substrate, such as a glass slide or mice. This produces a deflection (Volts) versus displacement (nm) curve. The inverse slope of the curve represents how many nanometers (nm) of deflection corresponds per Volts of deflection. DeflV: Deflection in Volts; ZSnr: Vertical displacement of piezocrystal (sensor).

Polymers:

For cantilever–based nanoindentation on PP and PMMA three AFM cantilevers with different spring constants were used. The AFM cantilever were used to indent the samples at the a number applied loads ranging from 0.03 to 5 N.

More specifically, the AC160 cantilevers were used to perform indentation tests for applied loads at 1 , 2 and 5 N. A sample image of 15 m x 15 m was scanned and 9 indentation positions were defined with 5 m separation distance. Loading and unloading time were set to 10 sec and holding time at maximum load for 10 sec to minimize creep relaxation effects. Then an image was recorded to confirm the presence of indents. These experiments were performed by Dr. Jurgita Zekonyte and Mr. Sebastien Fabri.[4]

The AC200 and NSC/CSC were used in testing both polymers and collagen fibrils. The applied loads in these experiments were set at 30 nN (same as in bronchial airway collagen fibrils) and 150 nN (same as in murine collagen fibril). For these tests we performed Force Volume (FV) maps over a 2 m x 2 m area with resolution of about 30 points x 30 lines. The scan rate was set to 50 nm/sec and no holding time was applied.

Collagen fibrils:

Unless otherwise specified, the AC200 and NSC cantilevers were used for cantilever–based nanoindentation on collagen fibrils. AFM imaging, prior to nanomechanical data acquisition, allows the user to discriminate individual collagen fibrils deposited on a flat stiff surface (glass slide) from fibril bundles, as illustrated in Figure 4.2. This is important because results from testing on a fibril bundle will most probably not be representative of a single fibril.

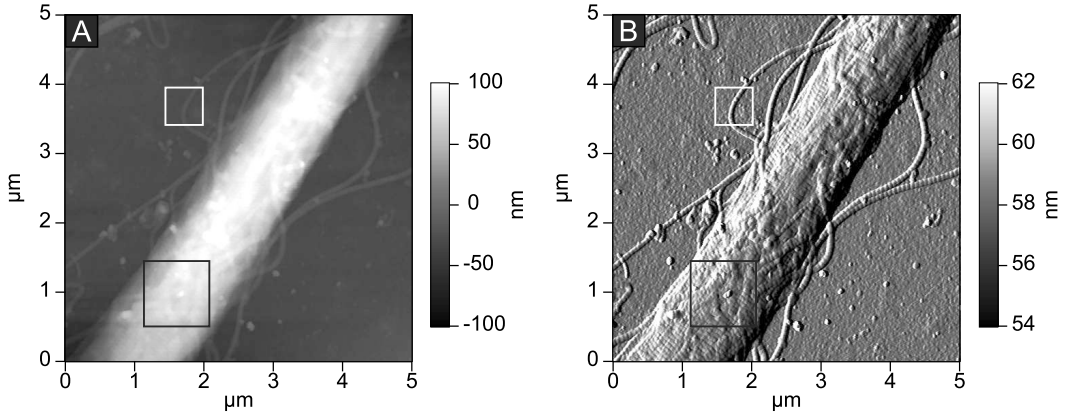

Figure 4.2: AFM (A) height and amplitude (B) image of individual collagen fibril deposited on the stiff glass slide (white rectangle) and collagen fibrils arranged into a fibril bundle (black rectangle).

During AFM cantilever-based nanoindentation on individual collagen fibrils it is important to avoid substrate effects but also to ensure sufficient cantilever deflection. In conventional nanoindentation of thin films the maximum indentation depth that can be achieved before the substrate affects the resulting force curves is limited to 10% of the total thickness of the sample (Persch et al., 1994). For nanoindentation testing on individual collagen fibrils, this was accomplished by setting an applied load of 150 nN for murine samples (where the diameter of tested fibril was larger than 80 nm) and 30 nN

[4] Affiliations are shown in the footnote of page 51.

for collagen obtained from bronchial biopsies (where fibril diameter was approximately 30 nm). This choice of the applied load was achieved after testing a fibril over a range of applied loads and comparing the maximum indentation depth with the overall height of the fibril from the substrate as well as the derived indentation modulus.

A region of interest (ROI), including both a portion of the fibril and the glass slide surface, was initially imaged. For ease of data collection the fibril long axis was aligned to the fast scan direction. After offsetting the fibril on the centre of the image window a Force Volume (FV) map was recorded. Each pixel of the FV map corresponds to a single force–indentation test. The size of ROI depended on the fibril size and the intended resolution (number of pixels) of the FV map. It was aimed to keep the time low to minimize thermal drift effects of a recorded FV low and obviously this cannot be achieved with high resolution FV maps. To obtain the least possible resolution but sufficient to provide meaningful data we needed to consider the size of the fibril (width) and the window length of ROI. Another important consideration was to record data on the very crest of the fibrils. This minimized systematic errors of improper contact between the tip and the fibril due to the cylindrical fibril geometry. We have empirically found that a minimum of 10 lines per fibril width are sufficient to produce data on the fibril crest. We also propose below a simple function that returns the number of FV pixel resolution:

$$PixelResolution = W\frac{n}{D} \tag{4.1}$$

considering the known fibril width, D, the window length of ROI, W and the favoured total number of force curves, n. As illustrated in Figure 4.3, for 10 lines to be recorded transversely within a 400 nm (D = 400 nm) wide fibril over a 2 m x 2 m area the resolution (W = 2000 nm) should be 50 points x 50 lines (i.e. $PixelResolution$ = 50).

To test the repeatability and the effect of the glass slide substrate on the indentation modulus of collagen fibrils twelve (12) points were selected on a collagen fibril originated from WTM tail tendon (deposited on the surface of the glass slide) as shown in Figure 4.4. The odd numbered points in Figure 4.4 correspond to single force–indentation curve at 150 nN applied load. On the other hand, nine consecutive force–indentation curves, with increasing applied load at 30 nN, 90nN, 150 nN, 210 nN, 270 nN, 330 nN, 500 nN, 1000 nN and 2000 nN, were recorded on each of the six even numbered points.

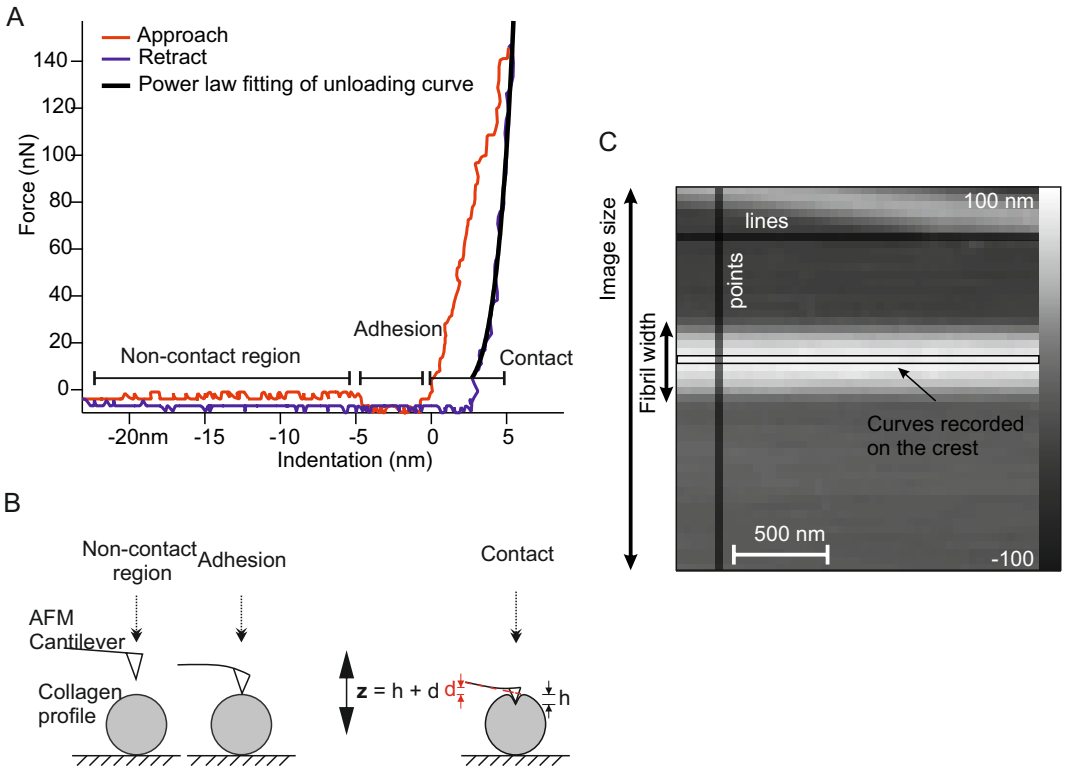

Figure 4.3: (A) Typical force–indentation curve from AFM cantilever–based nanoindentation on a collagen fibril. (B) Schematic of the experiment on a collagen fibril. (C) Force Volume map of a collagen fibril recorded with the fast scan axis parallel to the long axis of the fibril with a resolution of 50 points x 50 lines. The image size was 2 μm x 2 μm and the width of the fibril approximately 400 nm. z: total vertical displacement; h: indentation depth; d: cantilever deflection.

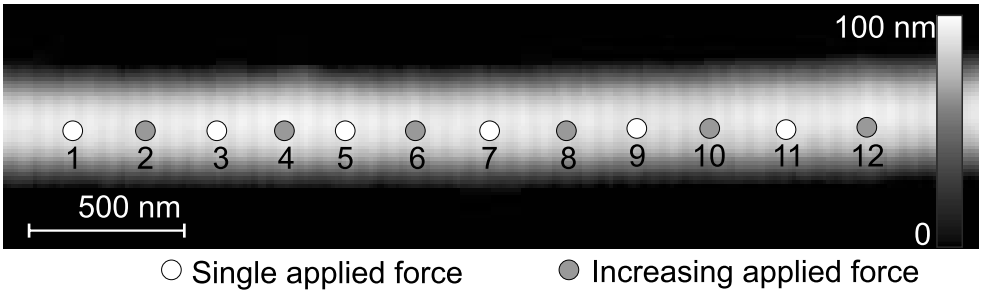

Figure 4.4: Odd numbered points correspond to preselected positions where single force–indentation curves were performed at 150 nN maximum applied force. Even numbered points correspond to preselected positions where nine force–curves were selected at each point with increasing maximum applied force from 30 nN to 2000 nN.

4.2.3 Data analysis

4.2.3.1 Projected area function and indentation modulus determination

The recorded data were analysed as described in subsection **??**. In brief, we performed the Oliver–Pharr method for calculations of indentation modulus. For deriving a function of the contact area we first reconstructed the AFM tip apex and then delivered the area function using a built–in function in the AFM control package within the IGOR Pro 6.05 software, as described in subsections 4.2.3.2 and 4.2.3.3.

4.2.3.2 AFM tip reconstruction

To obtain the contact area function for the AFM tip apex, it is important to be able to know the geometrical features of the tip. Some have This can be achieved by several reconstruction methods. proposed by Keller and Franke (1993).

Initially an AFM image of a silicon spike from a calibration grating (TGT1, NT-MDT) was recorded. The resulting image is a convolution of the tip–spike geometrical features. A deconvolution image of the tip shape is then generated from a reconstruction algorithm programmed in Matlab assuming the spikes to be cones with an opening angle of 50 degrees and a tip radius of 5 nm (as proposed by the manufacturer). The projected area function was extracted from the reconstructed image of the tip using a built-in function of the Igor Pro software (Igor Pro 6.22A, v.101010 0723, Asylum Research). The extracted data, of projected area and height of the tip, were then fitted with Equation 3.2. Figure 4.5 shows the three dimension perspectives of the convoluted and reconstructed AFM height images and their corresponding area functions of contact.

4.2.3.3 Determination of projected area of contact

Determination of indentation modulus data requires the acquisition of projected area function of contact between the indenter and the sample. The area function of the indenter used in conventional nanoindentation is determined by direct imaging of the Berkovich tip with an AFM (Barone et al., 2010; Gadelrab and Chiesa, 2012). For AFM imaging, the indenter must be mounted firmly and expose the tip apex towards the AFM tip. Post imaging analysis deliver the projected area function of the indenter (using a built–in function in the AFM control package within the IGOR Pro 6.05 software).

4.2.3.4 Statistical analysis

All statistical analysis was performed in OriginLab. One way analysis of variance (ANOVA) was performed to test differences between groups. To correct for unequal

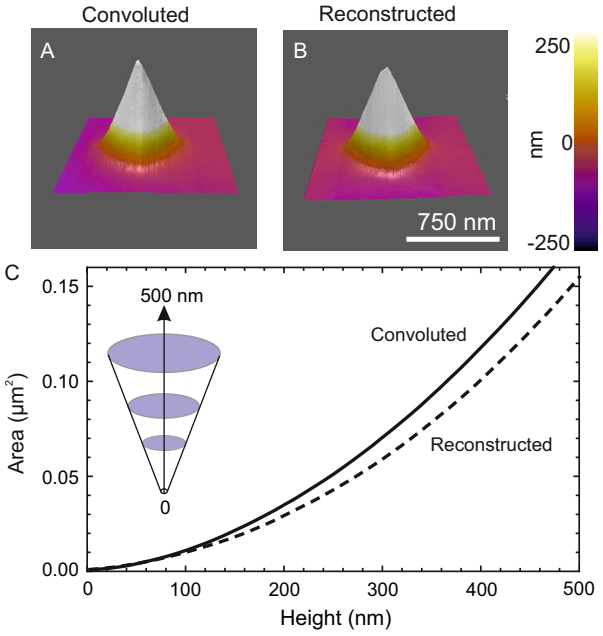

Figure 4.5: Three dimensional perspectives of (A) the convoluted and (B) the reconstructed AFM height images. (C) Area functions of convolution and reconstructed images.

variance among the data, transformations were applied appropriately such as normal logarithm or square root (Wilson and Worcester, 1945). Results were considered to be significant for P–value <0.05. Unless otherwise specified, data are presented as mean ± standard deviation.

4.3 Results and Discussion

4.3.1 Conventional versus AFM cantilever–based nanoindentation of PMMA and PP

Typical loading and unloading force–indentation curves of PP and PMMA recorded by AFM cantilever–based nanoindentation within a range of applied forces (30 nN to 5) are shown in Figure 4.6. Average indentation modulus values of both polymers at 50 N, 100 N and 1000 N applied loads determined via conventional nanoindentation tests were not significantly different, as presented in Figure 4.7.

The indentation modulus of PP determined via AFM cantilever–based nanoindentation, E_{PP-AFM} = (1.29 ± 0.34) GPa), did not differ significantly (P–value = 0.13) from the one determined via conventional nanoindentation, $E_{PP-Conv}$ = (1.66 ± 0.08) GPa. One the contrary, the indentation modulus of PMMA determined via AFM cantilever–based nanoindentation, $E_{PMMA-AFM}$ = (3.46 ± 0.72) GPa, was significantly lower (P–value = 0.03) compared to the one determined with conventional nanoindentation, $E_{PMMA-Conv}$

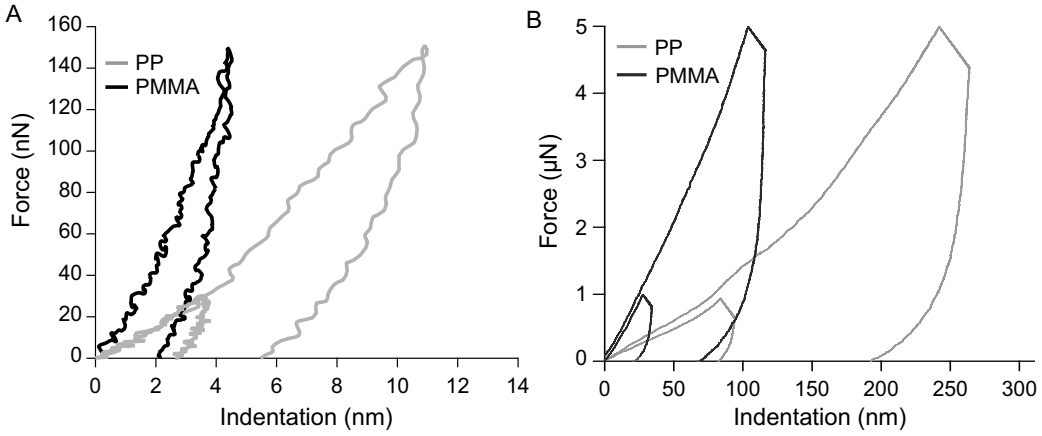

Figure 4.6: Typical force–indentation curves recorded with AFM cantilever–based nanoindentation on PMMA and PP for a range of applied loads. Note that the units of force in panel A are nanonewtons (nN) and that in panel B are micronewtons (μN).

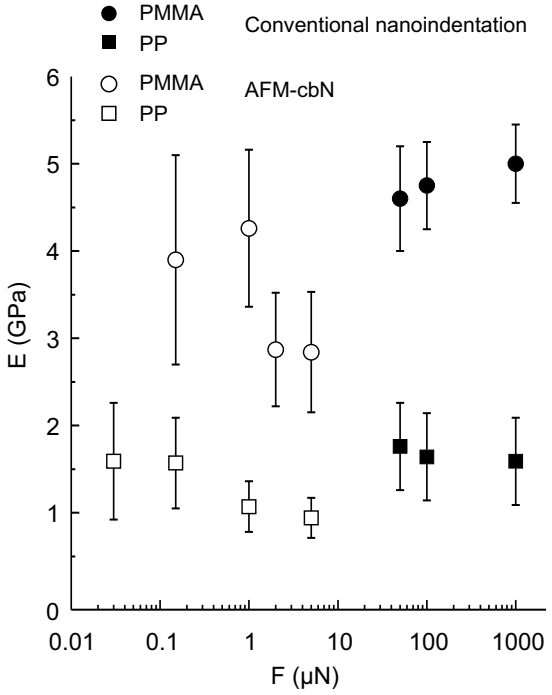

Figure 4.7: Indentation modulus values of PMMA and PP determined via AFM cantilever-based and conventional nanoindentation at a range of applied loads from 0.03 μN to 1000 μN.

= (4.78 ± 0.20) GPa. The coefficient of variation (CoV) of PP and PMMA suggests that AFM cantilever–based nanoindentation on both polymers has larger variability – CoV_{PP} = 17% and CoV_{PMMA} = 36%, compared to conventional nanoindentation – CoV_{PP} = 5% and CoV_{PMMA} = 12%.

In conventional nanoindentation, the indentation depth of PMMA and PP ranged between 77 nm to 394 nm and 150 nm to 730 nm respectively. In AFM cantilever–based nanoindentation the indentation depth of ranged between 5 nm to 122 nm for PMMA and 4 nm to 247 nm for PP. It is possible that lateral sliding of the AFM probe might occur during small penetration depths in AFM cantilever–based approach. This could lead to systematic errors of the measured indentation modulus and increased variability. Additionally, the chemical state of the polymer surface could also be responsible for the larger variability of the data. It is well known that surface properties of polymers can differ from bulk ones. Hence, indentation modulus may change with increasing the applied load (i.e. increasing indentation depth) due to different degrees of cross–linking on the surface and below this layer, as well as surface mechanical and chemical aberrations. Surface changes usually lead to a stiffer outer layer compared to the layers of the bulk material (Grunlan et al., 2001).

Material composition (i.e. the ratio of crystalline and amorphous regions) could be most likely responsible for the variation in indentation modulus, with increasing the applied load, in PMMA (Clifford and Seah, 2005). Crystalline regions are denser than amorphous ones, hence resulting in a larger indentation modulus. Further, segregation of low molecular weight species and less densely packed amorphous regions at the surface area (within the top 40 nm 200 nm) of PMMA (Satomi et al., 1999; Kawana and Jones, 2001) would result in a lower indentation modulus at applied loads lower than 10 μN, as shown in Figure 4.7. In the current study, the penetration depths in both PMMA and PP ($\approx$122 nm for PMMA and $\approx$247 nm for PP) are comparable to the size of the amorphous segregation regions on the surface. Additionally, AFM cantilever–based nanoindentation provides rather localized measurements. Considering this and that both crystalline and amorphous regions are present, we can explain why we observe higher variability of the indentation modulus in data obtained from AFM cantilever–based indentation.

Another source of error in nanoindentation experiments is associated with surface roughness. The determination of contact area between the tip and the sample is affected by the presence of asperities, in particular if their size is comparable to the indenter size (Fischer-Cripps, 2012). This can largely influence the derived indentation modulus. To study the effect of roughness we tested two areas in PP, one with 40 nm and the other with 10 nm RMS roughness. AFM height images, their corresponding FV maps and box plots of indentation modulus are shown in Figure 4.8. The rougher area (RMS = 40 nm) shows a larger variability – (2.27 $\pm$ 2.11) GPa, CoV = 93% – compared to the smoother area (RMS = 10 nm) - (1.56 $\pm$ 0.85) GPa, CoV = 54%. Still the area with the lower surface roughness show considerable variability. This can be explained by the size of the AFM tip radius of about 10 nm, which is comparable to the RMS roughness of 10 nm.

The effect of roughness can be reduced by introducing a larger tip radius and also higher applied loads to reach larger indentation depths. Clifford and Seah (2005) have shown

a lower variation in indentation modulus compared to our data. The authors of this study used AFM cantilevers with a tip radius of 176 nm, which is about ten times larger compared to the ones used in the present study. Additionally Clifford and Seah (2005) applied loads more than 3 μN reaching indentation depths from 10 nm to about 500 nm. Results presented in Figure 4.8 are limited in 150 nN applied loads and the tip radius was not more than 20 nm. This explains why our data show larger variability from those in literature. For the same reason, the variation of indentation modulus determined via AFM cantilever–based nanoindentation presented in Figure 4.7 is larger than the one presented by Clifford and Seah (2005).

We tested the polymer samples at low applied forces, i.e. similar to the ones applied with the same AFM cantilevers on collagen fibrils. Distributions of indentation modulus determined with AFM cantilever–based nanoindentation at low applied forces (30 nN and 150 nN) of PP and PMMA are shown in Figure 4.9. More specifically, the indentation modulus distributions of PP resulted from applying two different loads (30 nN and 150 nN) using the same AFM cantilever (AC200). On the other hand, the distribution of PMMA data is a result of using the same load (at 150 nN) with two different AFM cantilevers (AC200 and NSC). The AC200 has a lower spring constant (8.3 $\pm$ 1.8 N/m) compared to the NSC (44.5 $\pm$ 5.6 N/m). Both results from PP and PMMA suggest reproducibility. Although the indentation modulus values for PMMA show larger variation, as discussed above, it is possible to obtain reliable measurements of samples with different indentation modulus values using AFM cantilever–based nanoindentation. Yet it might be sensible for bulk samples, to either reduce surface roughness as much as possible, or to selectively only analyse data points obtained from flat locations on the surface.

4.3.2 Collagen mechanics at the individual fibril level

4.3.2.1 Nanoelasticity of human and murine collagen fibrils

The mean indentation modulus of collagen fibrils from human bronchial biopsies (HBB) was (1.3 $\pm$ 0.4) GPa, from rat and wild type mouse tail tendon (RTT and WTM respectively) was (2.8 $\pm$ 0.9) GPa and (8.4 $\pm$ 1.7) GPa respectively. Results are presented in Figure 4.10. Individual values represent the mean indentation modulus of:

- Each donor (n=7 donors) for HBB samples. Three fibrils were tested from each donor and about 20 to 30 curves were recorded on each fibril.
- Each fibril tested for RTT (n=3 fibrils) and WTM (n=8 fibrils) tail tendons. Samples were harvested from one animal from each species.

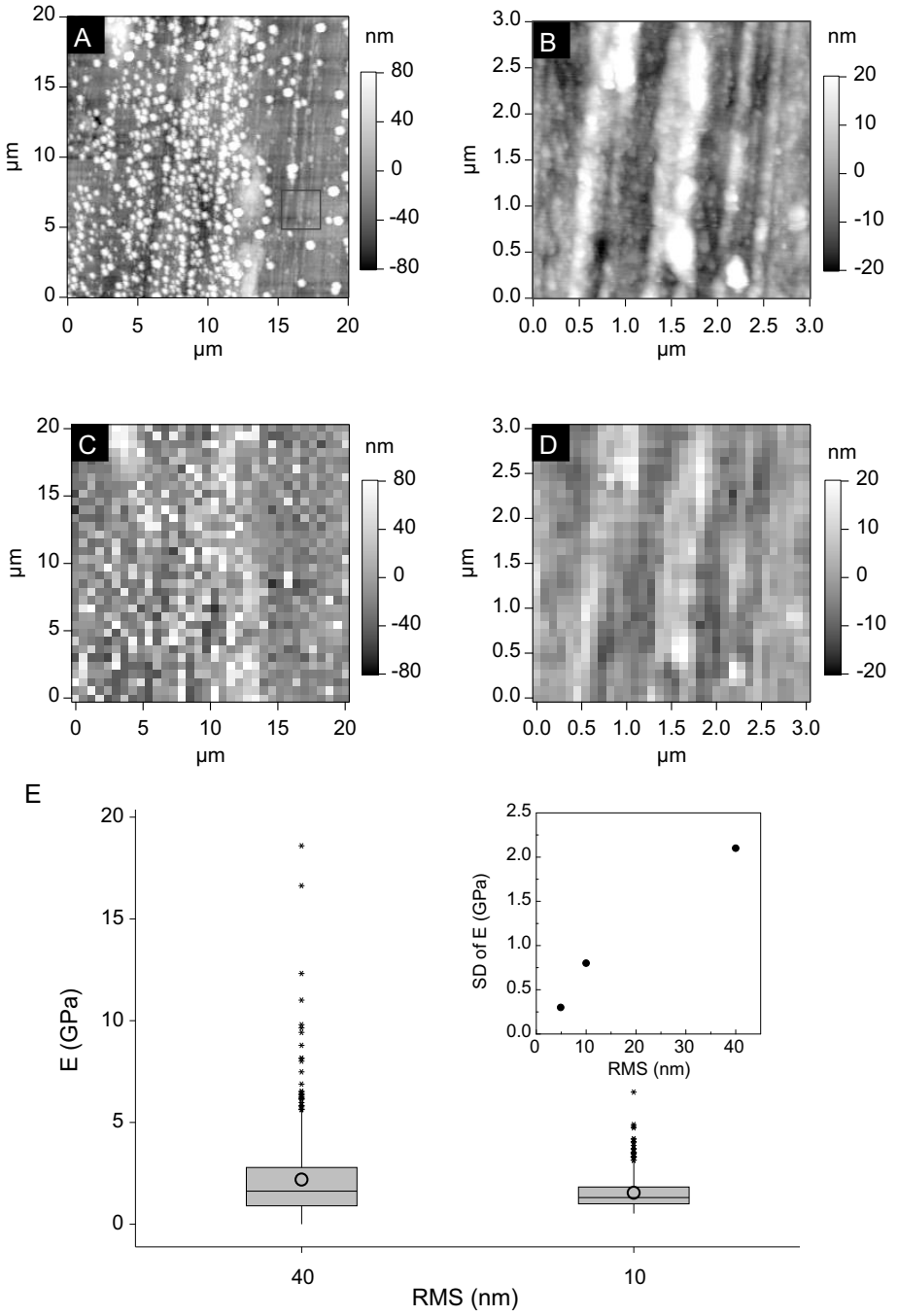

Figure 4.8: AFM height images of a (A) 20 μm x 20 μm and a (B) 3 μm x 3 μm area on PP. Corresponding force maps of the two areas (C, D) and (E) box plots of indentation modulus against the RMS roughness values. The median values are shown with a horizontal line, the mean values with a circle and the first and third quartiles (Q1 and Q3) are the bottom and top of range of the box plot respectively.

Statistical significant differences (P–value <0.01) were detected between all samples. The nature of the difference could be a result of the chemistry of collagen cross–linking. Variation in cross–link chemistry of collagen have been suggested to be tissue and

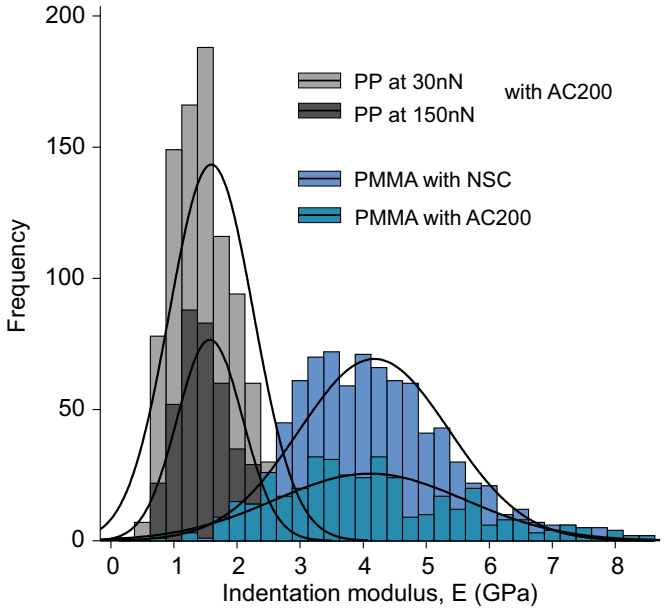

Figure 4.9: PP was tested with the AC200 cantilevers in the same area but with applied forces of 30 nN and 150 nN. PMMA was tested with two different cantilevers, the AC200 and NSC, at same applied force of 150 nN. Indentation modulus values were found to be (1.59 ± 0.66) GPa (n=959, 30 nN) and (1.57 ± 0.52) GPa (n=400, 150 nN) for PP and (4.17 ± 1.19) GPa (n=828, NSC) and (4.11 ± 1.15) GPa (n=390, AC200) for PMMA.

collagen–type specific rather than species specific (Eyre and Wu, 2005; Avery and Bailey, 2008).

The structure of fibrillar collagens is maintained by the formation of covalent cross-links between the telopeptides of adjacent collagen molecules. These collagen cross–links are regulated the hydroxylation of telopepeptide lysine (Lys) and hydroxylysine (Hyl) residues (Eyre and Wu, 2005). Hydroxylation of Lys and Hyl residues is induced by the enzymes lysyl oxidase and hydroxylase respectively. The tissue–specific differences in the chemistry of collagen cross–links (Robins and Bailey, 1977; Avery and Bailey, 2008) depend on the degree of hydroxylation of these residues (Yamauchi and Shiiba, 2008). Differences in the indentation modulus of collagen originated from the bronchi and tail tendons may be partly explained by change in the chemistry of collagen cross–links between these tissues.

Another source of different type of cross–linking could be the ratio of collagen types. Type I collagen predominates in murine tail tendons and bronchial airway walls. However, type I collagen fibrils are not explicitly constituted of collagen type I molecules. In fact, collagen types III and V molecules form co–fibrils with collagen type I during the formation of type I collagen fibrils (Kadler et al., 1996). Specifically, collagen V molecules are known to be responsible for initiating fibril formation (Birk, 2001). During tendon formation, the increase of collagen fibril diameter has been associated with a decrease in expression of type III collagen (Birk and Mayne, 1997). On the other

hand a significant amount of collagen type III has been detected in the subepithelial membrane of bronchial airways (Godfrey, 2009). This may explain changes in the type of cross–linking resulting in lower indentation modulus.

In addition to enzymatic cross–links there are also the non–enzymatic reactions in the collagen fibrils that occur with time. These reactions result in the accumulation of glucose mediated inter–molecular cross–links (Reiser, 1991). An increase of tissue stiffness is observed with increasing the amount of glucose mediated cross–links (Sims et al., 2003; Bank et al., 1998; Reihsner and Menzel, 1998). Thus, stiffening may also occur on the individual collagen fibril level, which could also explain the differences in modulus we observe between the different species.

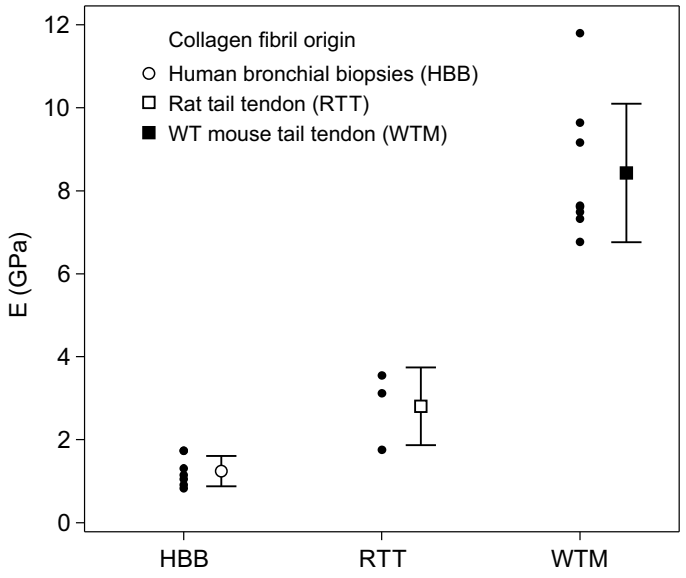

Figure 4.10: Indentation modulus of collagen fibrils from human bronchial biopsies (HBB), rat (RTT) and wild-type mouse (WTM) tail tendon. The individual markers in HBB correspond to the mean indentation modulus of individual volunteers, whereas the markers in RTT and WTM correspond to mean indentation modulus of individual fibrils. The mean indentation modulus is significantly different (P–value <0.01) between all samples.

4.3.2.2 Repeatability test and effect of substrate

The corresponding force–indentation curves with increasing applied force are shown in Figure 4.11. The loading part of force–indentation curves from 0.03 to 0.33 N lie on top of each other. Force–indentation curves recorded at 0.5 N to 2 N overlap only in the lower part (up to about 300 nN) and beyond this point the slope increases resulting in non–overlapping regions. The non–overlapping regions are most likely due to the substrate affecting the cantilever deflection. At large indentation depths the

stiff substrate prevents the tip from further penetration, resulting in increased relative deflection and therefore force.

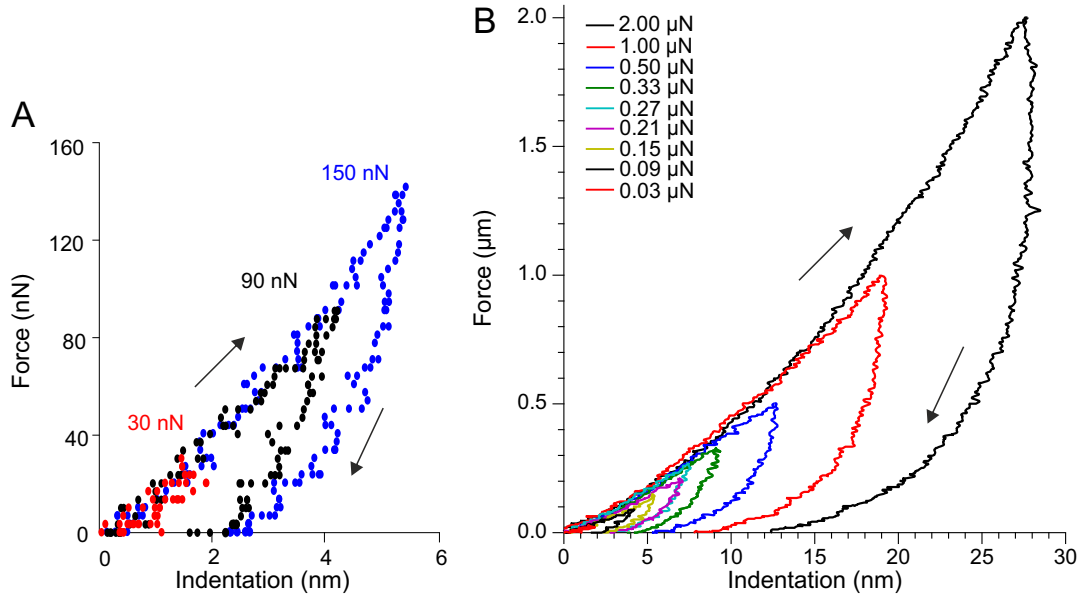

Figure 4.11: Force–indentation curves from repeatability test on a collagen fibril.

Indentation modulus values are presented versus the maximum applied load in Figure 4.12A and the maximum indentation depth (h_{max}) normalized to the fibril height in Figure 4.12B. For 30 nN and 90 nN applied loads (i.e. indentation depths) the mean indentation is higher with a larger variation compared to the one determined at 150 nN. In fact the mean indentation modulus at 150 nN is the lowest with the smallest variation compared to all the other measurements. For applied loads from 150 nN to 500 nN the indentation modulus increases gradually from 2.8 GPa to 3.3 GPa. For 500 nN to 2000 nN applied loads indentation modulus increases to 6.6 GPa. A summary of the results of mean indentation modulus and coefficient of variation are presented in Table 4.1.

Load (nN)	**Indentation depth (nm)**	**Indentation modulus (GPa)**	**CoV (%)**
30.0	1.4 (0.2)	4.0 (1.5)	38
90.0	3.4 (0.7)	3.0 (0.9)	30
150.0	4.8 (0.7)	2.8 (0.5)	18
210.0	5.9 (0.9)	2.9 (0.7)	24
270.0	7.0 (0.9)	3.1 (0.9)	29
330.0	7.9 (1.2)	3.2 (0.8)	25
500.0	10.1 (1.8)	3.3 (0.9)	27
1000.0	17.4 (2.6)	4.0 (0.7)	18
2000.0	26.3 (2.6)	6.6 (2.1)	32

Table 4.1: Summary of results from the repeatability test.

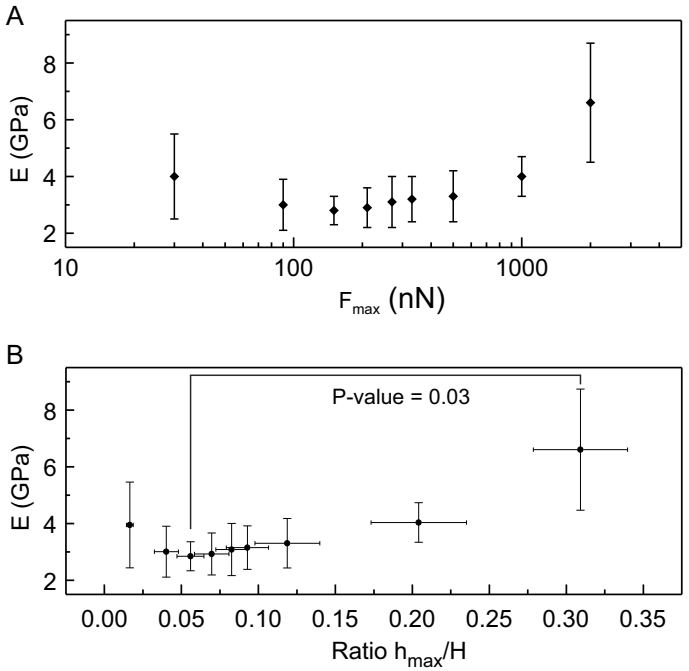

Figure 4.12: Indentation modulus plotted against the applied load in panel A and against the ratio of indentation depth and height of the collagen fibril. The lowest point was observed at 150 nN applied load. The indentation modulus increases gradually beyond 150 nN of applied load. However, only the indentation modulus at 2000 nN applied load was statistically significant different from the one determined at 150 nN applied load. From panel B we can conclude that the 10% rule, of maximum indentation depth without the substrate affecting the indentation modulus values, must be followed although maintaining the maximum indentation depth to 6% of the collagen fibril height is ideal for minimizing the standard deviation.

The larger mean value and variation of indentation modulus that was determined at 30 nN and 90 nN applied loads could be attributed to the relatively rough surface of collagen fibrils compared to the tip radius (R_{tip}) and the small indentation depths (h). The possible effect of collagen surface roughness is discussed in Appendix A.

A larger difference of indentation modulus (160%) has been observed between the overlap and gap regions along the collagen fibril, with the overlap regions being stiffer (Grant et al., 2012). This differencehas been attributed due to the density disparity of these regions (Grant et al., 2012). Researchers from this group performed dynamic mechanical analysis, by indenting collagen fibrils driving the AFM cantilever at a range of frequencies from 0.5 Hz to 2 Hz with oscillatory force as low as (30 ± 15) nN. Unravelling the bimodal distribution of indentation modulus in the present study was not possible as we used static instead of dynamic loading in combination with the lower resolution of the recorded FV maps (i.e. number of force curves recorded along a fibril).

Another potential issue during indentation is the cylindrical geometry of collagen fibrils. Indenting on the crest of the fibril minimizes errors associated with improper contact

between the AFM tip and the sample, and as explained, care was taken in the present study that analysed indents were indeed always placed on the crest of a fibril. Contact on the sides of the fibril results in force–indentation curves that deviates from the ones taken on the crest. A comparison of force–indentation curves taken on the crest and on the side of the fibril are presented in Figure 4.13.

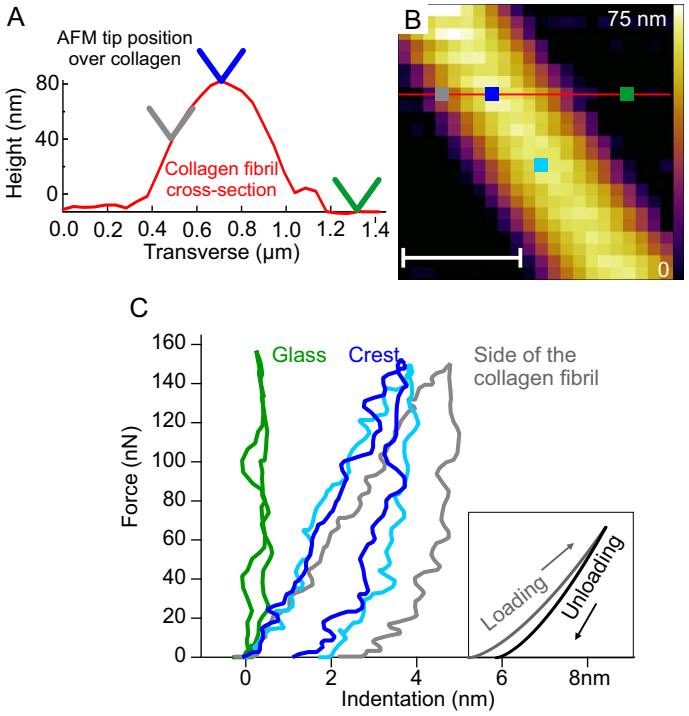

Figure 4.13: Panel A shows a cross–section graph (red line) of a collagen fibril and three cases of point of contact the tip (shown in **V**) and cross–section. Panel B shows a force volume map of the corresponding collagen fibril. In panel C, the force-indentation curves retrieved at different point of contacts are compared to each other. The green graph in panel C corresponds to the green pixel in panel B and to the green . The force-indentation curve is influenced by the position of the point of contact on the collagen fibril. .

Point and shoot operation gives the opportunity to the user to selectively perform force–indentation tests around the sample by selecting points on the previously recorded image. However, experience showed that this operation should be used with great care because of thermal drift issues. In fact this effect could have been partly responsible for the variation of the data shown in Figure 4.4. The experience from this study suggests that the use of FV maps is a better approach the point–and–shoot unless the specific loading protocol makes FV maps infeasible.

Residual imprints were visible in AFM imaging only beyond 200 nN applied load, even though force–indentation curves recorded at 90 nN load already indicated a small plastic deformation of about 2 nm (intersection of unloading curve with x-axis in force–indentation curves). There could be several possible explanations why we could not image the residual imprints after indentation at loads less than 200 nN:

a. Masking of the imprints during AFM imaging with an AFM tip radius (≈10 nm) larger than the size of the imprints, ranging between 2–3 nm.

b. Relaxation after unloading. Viscoelastic behaviour under tensile loading is a known mechanical property of collagen fibrils (Shen et al., 2011). Although our experiments were conducted in air (environmental dry conditions) and under indentation loading, it is possible that collagen molecules rearrangement occurs after unloading at low applied forces.

c. Collagen fibril has surface topographical features, as shown in the error image (Amplitude AFM image; Figure 4.14), that could render the decision of describing a feature as a residual imprint difficult.

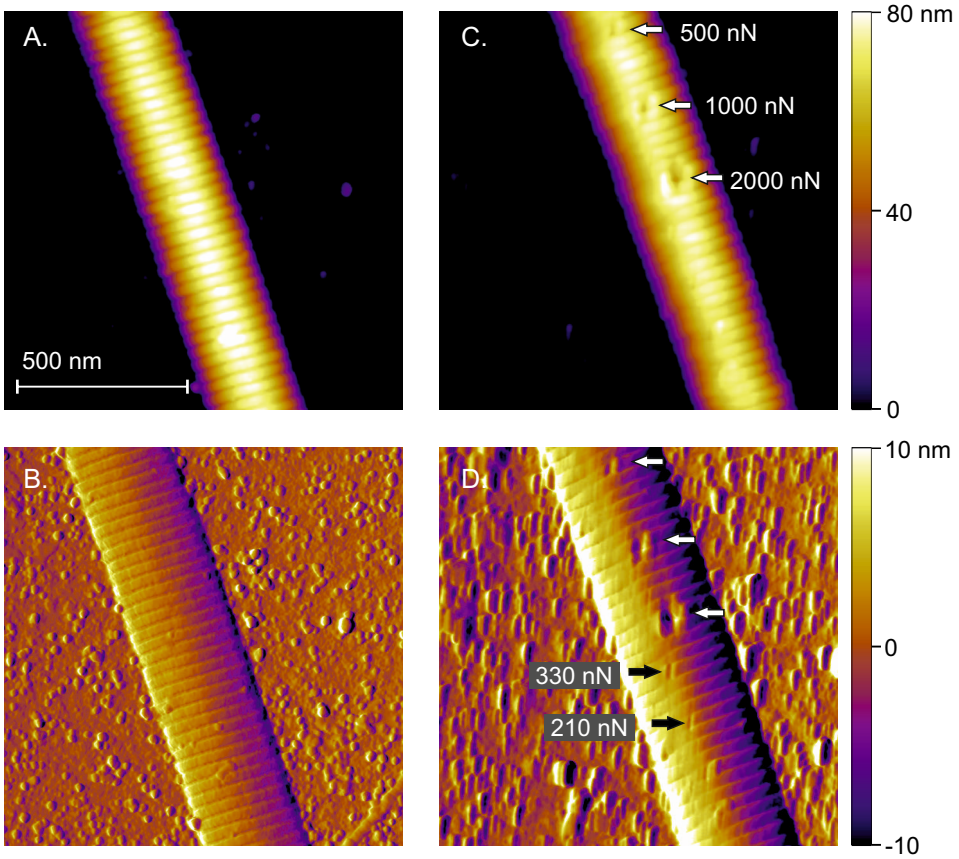

Figure 4.14: The height (A, C) and amplitude (B, D) AFM images of a collagen fibril before and after indentation tests illustrate the shape of residual imprints at different applied forces. Residual imprints were observed at maximum applied forces larger than 200 nN.

Additionally, the geometry of residual imprints recorded at applied force of 4 μN (Figure 4.15) provides insight on the anisotropic nature of collagen fibrils. Imprints possess an ellipsoid shape (major axis of about 200 nm and minor axis of about 40 nm), the major axis of which lies along the fibril longitudinal axis, which is along the long axis of the collagen molecules. Similar ellipsoid geometry of imprints was observed in the

collagen fibril shown in Figure 4.14. Interestingly, pile–up (indicated with white arrows; Figure 4.15) was present in the lateral direction of the fibril axis. This is most likely because of collagen molecules being compressed from the sides of the AFM tip apex. This would create tension loading on the collagen molecules located at the peripheral of the pile–up regions. However, no pile–up was observed along the major axis of the residual imprint (indicated with black arrows; Figure 4.15). This is most likely because splitting is the dominant deformation mechanism along the fibril axis. Splitting would follow after breaking of intermolecular cross–links located at the tips of the ellipsoid (blue arrow; Figure 4.15B).

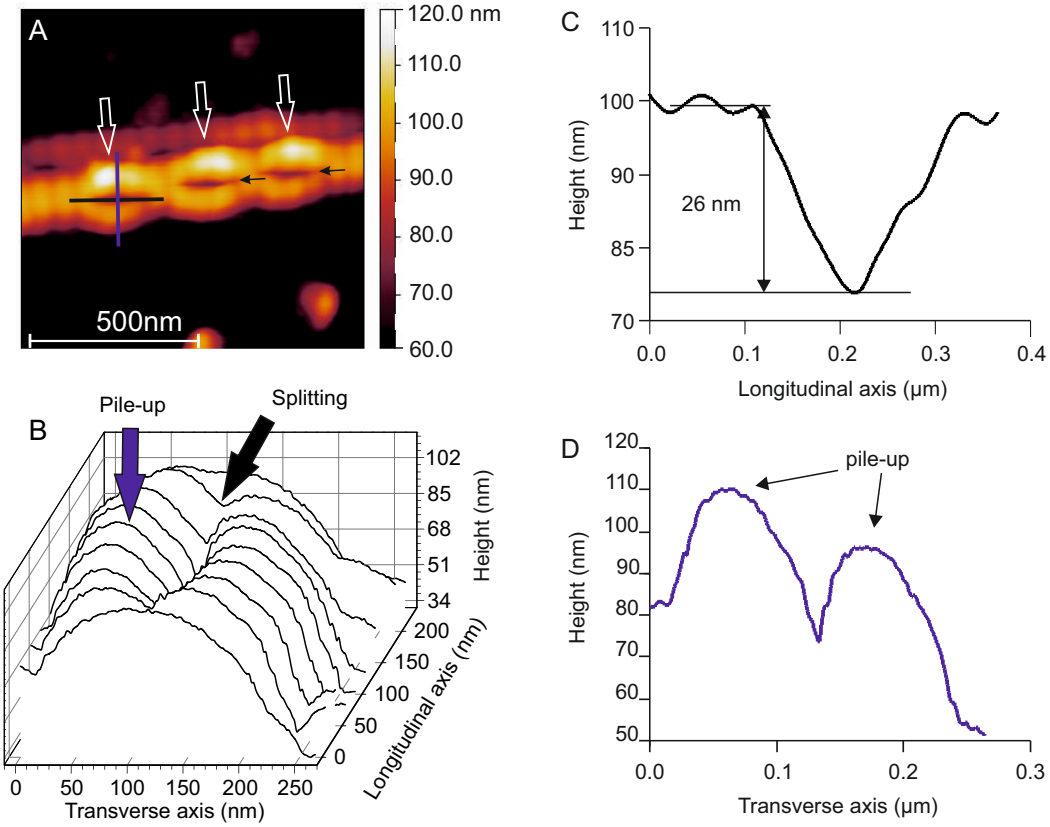

Figure 4.15: Residual imprints at 4 μN applied load. (A) AFM image of height topography of a collagen fibril originated from mouse tail tendon showing the residual imprints after loading at 4 μN. (B) Three dimensional illustration of a residual imprint. Pile–up is present only on the lateral direction of the fibril axis while it seems that splitting dominates as deformation mechanism along the longitudinal axis. (C, D) Line profiles of the imprint along the major and minor axis of the ellipsoid shape, respectively.

4.3.2.3 Effect of fibril diameter

Mean values of indentation depth, h, and indentation modulus, E, are plotted against the fibril (originated from WTM) diameter in Figure 4.16. There was no statistically significant correlation of the indentation modulus (P–value = 0.632) and depth (P–value

= 0.848) with fibril diameter. This finding would suggest that interpretation of data from a comparative study is feasible as long as indentation depth remains below the threshold of about 10% of fibril height.

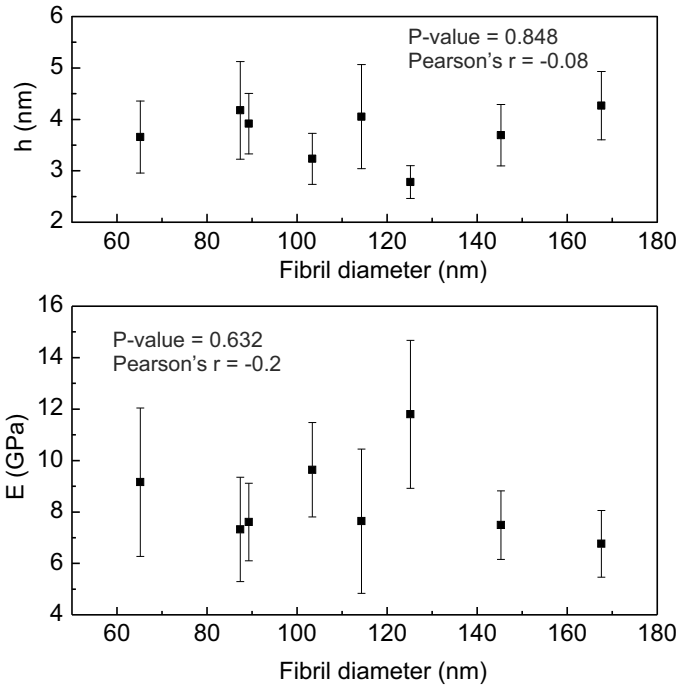

Figure 4.16: No statistically significant correlation was found between the indentation modulus and depth with the diameter of the fibrils.

4.3.2.4 Effect of analysis method

Several studies have previously investigated the mechanics of individual collagen fibrils by means of AFM cantilever–based nanoindentation (Heim et al., 2006; Grant et al., 2008; Wenger et al., 2007). Heim et al. (2006) have reported indentation moduli in the range of 1–2 GPa, and Grant et al. (2008) reported an average indentation modulus of (1.9 ± 0.5) GPa measured on reconstituted collagen fibrils originated from collagen from *Cucumaria frondosa* and bovine Achilles tendon, respectively. Wenger et al. (2007) have reported indentation moduli in the range of 3.7-11.5 GPa using native untreated collagen fibrils from rat tail tendon. The range of moduli values from literature is presented on the right hand side of the graph in Figure 4.17 with bars. Results from Grant et al. (2008) are comparable to those from Heim et al. (2006) but both are about 7 times lower from those presented by Wenger et al. (2007).

Collagen from all three studies originated from different species, although all three studies focused on type I collagen fibrils. The most likely explanation for the large differences in the results between Wenger et al. (2007) and the other two studies (Heim et al., 2006; Grant et al., 2008) is variations in the cross–linking, as discussed above in subsection 4.3.2.1. It is rather straightforward to assume that reconstituted collagen fibrils do have significantly different cross–linking, i.e. only immature divalent cross–links, compared to native collagen.

However, these studies have followed different analysis methods. Heim et al. (2006); Grant et al. (2008) have used the Hertzian contact theory whereas Wenger et al. (2007) have used the Oliver–Pharr method. The only difference between Heim et al. (2006) and Grant et al. (2008) was that the first assumed contact between a sphere (tip shape) and an infinitely long cylinder (fibril geometry). One might speculate that this could also be partly responsible for difference in reported indentation moduli.

Analysing our results from 8 fibrils in the same way as Grant et al. (2008) (Hertzian contact between two spheres) and Wenger et al. (2007) (Oliver–Pharr) showed that the Hertzian theory resulted in 24% lower indentation modulus when compared to the Oliver–Pharr method, while using the contact area function of the reconstructed tip. Additionally the Oliver–Pharr method assuming contact of a spherical indenter over a flat surface resulted in 8% and 42% larger average indentation modulus value compared to Oliver–Pharr using the reconstructed tip area function and Hertzian theory respectively. The contact area of a sphere and of the reconstructed tip apex is shown in Figure 4.18A. Indentation modulus values determined with the different approach of contact are compared in Figure 4.18B. The ratio of $E_{OP-Recon}/E_{OP-Sphere}$ is greater than 1 for ratio of areas $A_{OP-Recon}/A_{OP-Sphere}$ smaller than 1 and vice versa.

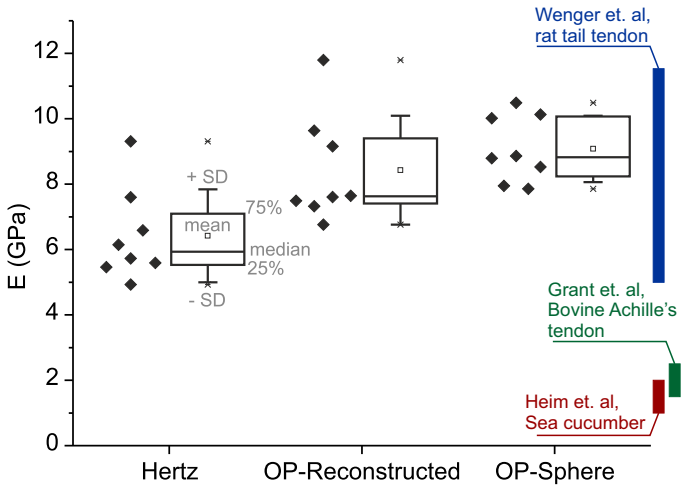

Figure 4.17: Indentation modulus plotted against the fibril diameter. No statistically significant correlation was found between the indentation modulus and depth with the diameter of the fibrils.

Changes in the contact area function result to slightly different indentation modulus values, which is explicitly due to the function of the contact area used in the Oliver–Pharr method. A comparison of the AFM tip area function (determined as described in section 4.2.3.3) with one of a sphere is shown in Figure 4.18A. The tip radius in the reconstructed tip shape was determined from the reconstructed image (Appendix B, Figure B.1). Below 2.9 nm of indentation depth the area of the sphere is larger than the one determined from the reconstructed method, which results in a lower indentation modulus value ($E_{OP-Recon}/E_{OP-Sphere} > 1$), as shown in 4.18B.

Our results from Hertzian analysis are higher than those presented in literature (Heim et al., 2006; Grant et al., 2009). Most likely cross–liking (as mentioned above) but also hydration state could be responsible for this difference. Both Heim at al. (20006) and Grant et al. (2009) have used reconstituted collagen fibrils. It is most likely that only immature divalent cross-links are present in these fibrils. This could explain the lower indentation moduli reported by these authors.

4.4 Conclusions

We have mechanically characterized individual collagen fibrils from rat tail tendon, mouse tail tendon and human bronchial airways via AFM cantilever–based nanoindentation. This is an important step towards the applicability of the technique on collagen fibrils with lower diameter (30 nm) compared to the ones studied previously (100 nm). However, our validation study and the comparison to previous studies suggested that there are limitations to be considered during interpretation of data. Such limitations are related to:

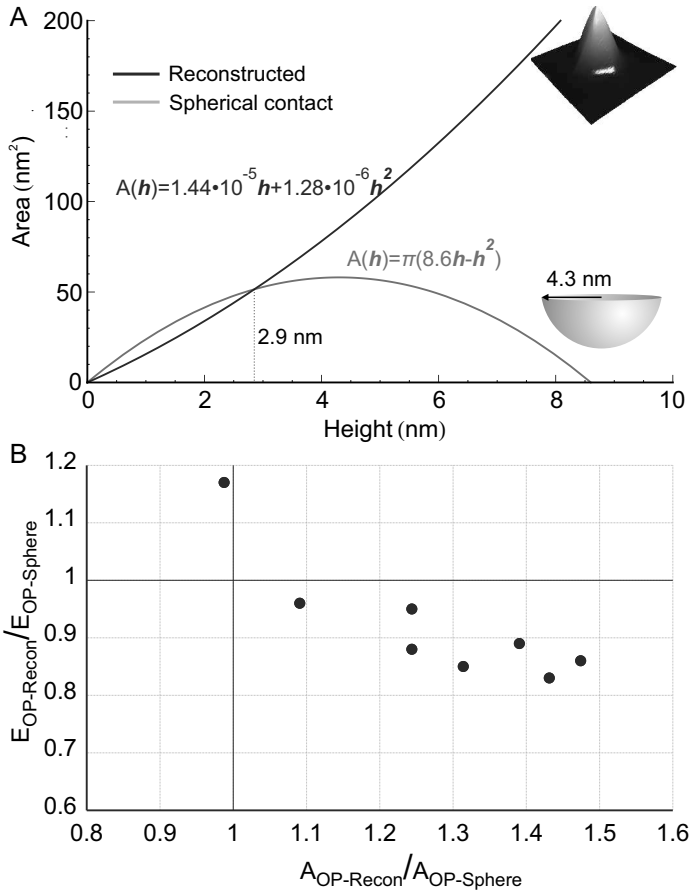

Figure 4.18: Projected areas of the reconstructed AFM tip and of a sphere with 4.3 nm radius. Assuming a spherical contact, the actual projected area is underestimated for indentation depths larger than 2.9 nm. This leads to an overestimation of indentation modulus values. (B) Indentation modulus differences between the two approaches are due to the different calculation of the projected area. It is therefore important to take into account the analysis method in the need of comparing results with literature or perform the same analysis method with literature that is of interest to compare with.

a. Sample topography. Geometrical features such as surface roughness and geometrical shape of sample (i.e. cylinder in the case of collagen fibrils) are responsible for the variation of data. This information can also be used to discriminate and if possible exclude data from analysis.

b. Tip geometry. Contact area depends on the tip geometry. Variations on the assumptions made to estimate the tip geometry could cause changes in the indentation modulus. This is possibly responsible for the larger effect on the accuracy of the measurements.

c. Analysis method. Several analysis methods exist to analyse data from nanoindentation tests. Assumptions amongst the various methods differ and therefore the resulting indentation modulus values. This should be considered when data are compared

to the literature values. Experimentation and analysis methods must be described in detail to allow cross–comparison of results obtained by different groups and different studies.

d. Biochemistry of collagen fibrils. The type and amount of inter–molecular cross–links seems to be determinant of collagen fibril nanoelasticity.

We additionally suggest the use of the reconstruction method to provide the contact area function of the AFM tip. The advantage is that this can be achieved with the same instrument, i.e. making it available to anyone performing cantilever-based indentation measurements.

The broad range of environmental conditions and ease of use of AFM has made it a popular technique for nanomechanical assessment of biological samples via cantilever–based nanoindentation (Cross et al., 2007; Stolz et al., 2009). The technique could be used to investigate the mechanics at different hierarchical levels of collagen tissues, most importantly at the level of individual collagen fibrils. Unravelling the mechanics at the individual fibril level of collagen will provide insight of the contribution of these elements on the mechanical properties at the tissue level. With no doubt AFM seems to be a promising tool to answer important biological, biomedical and clinical questions related to mechanical performance of collagen–rich tissues in both physiology and pathology.

Chapter 5

Altered structure–mechanical properties of type I collagen fibrils from the *oim* mouse model

5.1 Background

Recently, molecular dynamic simulations have shown larger local kink formations in the homotrimer compared to the heterotrimer collagen (Chang et al., 2012). Local kink formations were mostly responsible for the observed decrease in the tensile elastic modulus of the molecule (Chang et al., 2012). These findings may explain changes in crystalline packing into fibrils supported by evidence from x-ray diffraction of collagen originated from *oim* mouse compared to that from wild type (WT) ones (McBride et al., 1997). Additionally, Miles et al. (2002) have suggested a 7% higher inter–molecular lateral distance in *oim* collagen fibrils from estimations of increased volume fraction of water.

As a consequence of changes at the molecular and fibril level of type I homotrimeric collagen, a number of tissue abnormalities have also been reported in *oim* mice Byers et al. (1991); Prockop (1995). In particular, *oim* bones have been characterized by impaired mineralization processes due to changes in the composition and size of bone minerals (Phillips et al., 2000; Grabner et al., 2001). Abnormal collagen deposition in *oim* bones have also been reported (Phillips et al., 2002). Moreover, changes in the mechanical properties of *oim* bones have been reported. Both the strength and toughness are reduced in *oim* bones (Chipman et al., 1993; Miller et al., 2007). Similarly, the ultimate strength of *oim* tendons was impaired compared WT ones (Misof et al., 1997a).

Although, the substitution of $\alpha 2(I)$ chain from $\alpha 1(I)$ in the collagen molecule has been linked with reduced strength, toughness at the tissue level and structural abnormalities at the molecular level, the question with regards to changes in the relationship of structure–mechanical properties at the individual fibril level of collagen has not been answered so far.

This study is based on the hypothesis that the altered structure of *oim* type I collagen molecule alter the structure–mechanical function of the type I collagen fibril in *oim*.

AFM imaging and cantilever–based nanoindentation were employed to investigate the structure–mechanical relationship of *oim* collagen fibrils.

5.2 Materials and Methods

5.2.1 Chemicals

Phosphate Buffered Saline (PBS) tablets and pure ethanol were obtained from Sigma Aldrich, UK. For all experiments ultra–pure deionized water was used (Milli–Q DIRECT 5).

5.2.2 Animals and collagen sample preparation

Five months old B6C3Fe-a/a-+/+ wild type and pathologic B6C3Fe-a/a-Col1a2Oim/Oim mice were culled, tails were dissected and stored in gauze soaked with a phosphate buffer saline solution at -18^oC until further use. Each tail tendon section was harvested with scalpel and tweezers, and then deposited on microscope glass slide. To improve adhesion of collagen fibrils on the surface, poly–l–lysine coated glass slides were used (Thermo Scientific). To reveal areas with individual collagen fibrils the tail tendon sections were smeared out on the glass slide surface with the use of scalpel and tweezers similarly to Wenger et al. (2007). Samples were air dried, stored in a desiccator until further use. Maximilien Vanleene[1] and Prof. Sandra J. Shefelbine[1] contributed to this work by providing the mice tail tendons from wild type and *oim* animals, which were bred at the Department of Bioengineering at Imperial College, London.

5.2.3 Atomic force microscopy imaging and nanoindentation

AFM experiments were carried out in a temperature – (20.7 ± 0.7) ^oC – and humidity – (47.9 ± 6.7) % – controlled room with the MFP–3D atomic force microscope (Asylum

[1]Department of Bioengineering, Imperial College London, London, UK.

Research, Santa Barbara, CA, USA). All experiments that included the use of a solution were performed in a standard open fluid cell (Fluid Cell Lite, Asylum Research; Figure 5.1).

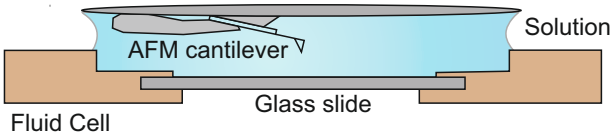

Figure 5.1: Illustration of experimental set–up for AFM cantilever–based nanoindentation performed in solution, either aqueous or ethanol.

Unless otherwise specified, images of individual collagen fibrils were obtained in contact mode at about 1 Hz scanning rate, either in air on dehydrated samples or in PBS before indentation testing. For swelling measurements, i.e. increase in collagen fibril height when going from dehydrated (experiments in air) to hydrated state, the same fibrils were imaged before and after hydration.

Cantilever–based nanoindentation tests were performed in fully hydrated samples (PBS), in air dried and in a number of PBS solutions with increasing concentration of ethanol. For nanoindentation tests on fully hydrated samples, the V–shaped and rectangular (PNP–TR and PNP–DB, NanoWorld AG, Switzerland) pyrex nitride cantilevers of (0.24 ± 0.02) N/m and (0.35 ± 0.05) N/m spring constants respectively (nominal values are 0.32 N/m and 0.48 N/m for PNP–TR and PNP–DB respectively) with a silicon nitride pyramidal tip of <10 nm tip radius, were employed. For nanoindentation tests in air dried samples, trihedral silicon tips with spring constant of (44.5 ± 5.6) N/m (nominal value is 40 N/m) and a tip radius of less than 10 nm (NSC15 rectangular cantilevers, MicroMasch) were used. For nanoindentation tests in pure ethanol, silicon cantilevers with spring constant (8.3 ± 1.8) N/m with about 7 nm tip radius (AC200, Olympus) were employed. All nanoindentation experiments were carried out under force control at 150 nN load for air dried samples, 2 nN load for PBS hydrated samples and at 14 nN load for samples immersed in pure ethanol. During indentation experiments, the maximum indentation depth must be considered to selecting the maximum load. The maximum indentation depth is limited to 10% of the height from the stiff substrate (Persch et al., 1994).

5.2.4 Acquisition of force curves

Acquisition of force curves from AFM cantilever–based nanoindentation was performed as described in section 4.2.2.2.

5.2.5 Determination of projected area of contact

For the NSC15 and AC200 cantilevers the projected area function of contact was determined by the reconstruction method described in section 4.2.3.2. Figure 5.2 shows the projected area function of contact of the AC200 cantilever tip which was used for nanoindentation experiments on collagen fibrils dehydrated with pure ethanol.

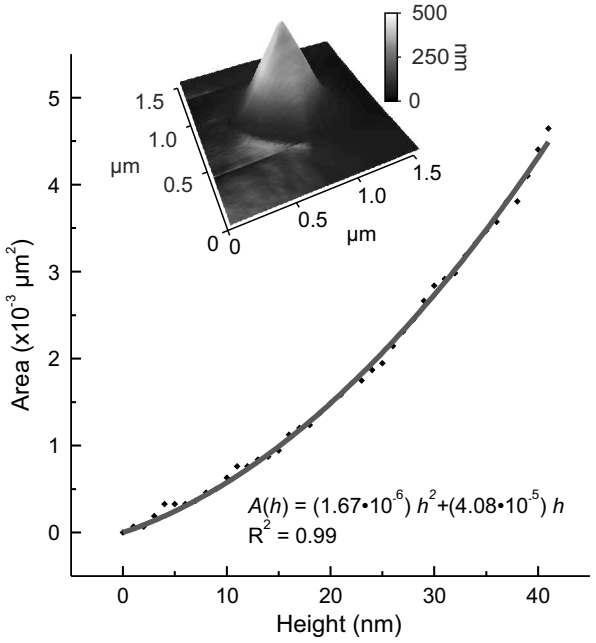

Figure 5.2: Projected area function of the reconstructed AC200 tip used in experiments carried out in 100% ethanol.

For the PNP–TR and PNP–DB AFM cantilevers the projected area of contact was approximated by assuming a pyramidal geometry with a round tip of radius R and half opening angle θ. The assumption of the pyramidal tip was based on the specifications provided by the manufacturer ($R = 10$ nm and $\theta = 35$ deg). A graphical representation of the vertical (blue) and horizontal (red) plane of a rounded pyramidal tip is illustrated in Figure 5.3. The projected area of contact of a pyramid with a round tip is given by:

$$A_{proj}(h, \xi) = 4\,(h + \xi)^2 \tan^2 \theta \tag{5.1}$$

where h is the indentation depth, ξ is a correction distance that accounts for the rounded tip. Assuming a sphere placed on the bottom of a pyramid the correction factor ξ can be described as a function of the half opening angle θ and tip radius R:

$$\xi(R, \theta) = R\,(\sin\theta + \cos\theta \tan\,(90 - \theta) - 1) \tag{5.2}$$

Equation 5.2 takes the more specific form:

$$A_{proj}(h) = 1.9\,(h + 7.4)^2 \tag{5.3}$$

for assuming a $R = 10$ nm and $\theta = 35$ rad.

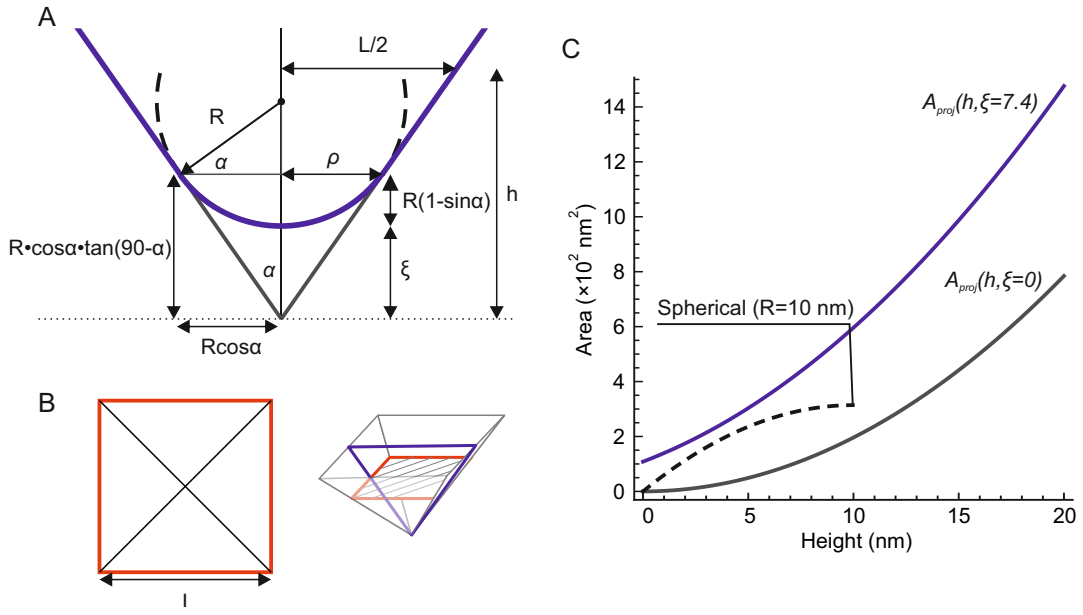

Figure 5.3: Vertical (blue; panel A) and horizontal (red; panel B) view of a round pyramidal tip with half opening angle θ and tip radius R. (C) Comparison of projected areas of contact among a spherical indenter of 10 nm radius (dashed curve), a pyramidal tip with sharp end (grey solid curve) and a pyramidal tip with rounded end (solid blue curve). h: indentation depth; ρ: contact radius; ξ: correction factor; L; width of rectangle.

For $h > R(1 - \sin\theta)$ the projected area can be determined by Equation 5.1. But for a round tip it is possible to have spherical contact. This is valid only when $h < R(1 - \sin\theta)$ and the projected area is described by Equation 5.4:

$$A_{sphere}(h) = \pi\left(2\rho h - h^2\right) \tag{5.4}$$

where ρ is the contact radius of the sphere as illustrated in Figure 5.3. Assuming a 10 nm tip radius and 35 degrees half opening angle, the factor $R(1 - \sin\theta)$ is 4.3 nm. The minimum indentation depths during AFM cantilever-based nanoindentation with the PNP cantilevers was about 10 nm. Therefore only Equation 5.1 for further data analysis, was used. The projected area of contact of a sphere (with 10 nm radius), of a sharp pyramid ($\xi = 0$, $R = 10$ nm, $\theta = 35$ deg) and a pyramid with round tip ($\xi = 7.4$ nm, $R = 10$ nm, $\theta = 35$ deg) are compared in panel C of Figure 5.3. Additionally, the area function retrieved from the reconstructed AC200 tip is shown in panel B of Figure 5.3.

5.2.6 Statistics

Statistical analysis was performed in Minitab 16.2.4. One way analysis of variance (ANOVA) was performed to test differences between groups. To correct for unequal variance among the data transformations were applied appropriately such as normal logarithm or square root. The generalized linear model (GLM) was performed to test differences between the rate of modulus increase of *oim* and WT collagen fibrils with ethanol concentration. Results were considered to be significant for P–value <0.05. Unless otherwise specified, data are presented as mean ± standard deviation.

5.3 Results

5.3.1 Indentation modulus of collagen fibrils from WT and *oim*

In PBS, the indentation modulus of *oim* collagen fibrils from both female and male animals was significantly larger – $E_{oim-♀} = (42.9 \pm 9.6)$ MPa, $E_{oim-♂} = (21.6 \pm 8.7)$ MPa with P–value <0.01 and P–value <0.001 respectively as shown in Figure 5.4 – compared to WT ones – $E_{WT-♀} = (6.9 \pm 3.4)$ MPa, $E_{WT-♂} = (2.6 \pm 1.7)$ MPa. Additionally, the indentation modulus of collagen fibrils from the *oim* female mouse was significantly larger than the *oim* male one (P–value <0.01). Although there is a trend of higher indentation modulus in female compared to male WT mice, no significant differences were observed (P–value $= 0.17$). Box plots of indentation modulus of hydrated collagen fibrils from *oim* and WT animals are presented in Figure 5.4.

In air dried samples, the indentation modulus of collagen fibrils was one order of magnitude greater compared to the ones measured in PBS. Interestingly, the modulus of *oim* collagen fibrils of male mouse – $E_{oim-♂} = (5.5 \pm 1.2)$ GPa – was significantly (P–value <0.05) lower compared to the one from the female WT collagen fibrils, $E_{WT-♀} = (8.4 \pm 1.7)$ GPa. Box plots of indentation modulus of collagen fibrils (experiments in ambient environment) from WT and *oim* mice are presented in Figure 5.5.

5.3.2 Indentation modulus of collagen fibrils increased with ethanol concentration

The indentation modulus of collagen fibrils from both WT and *oim* mice increased with increasing the ethanol (EtOH) concentration in the PBS solution (Figure 5.6). Interestingly, the rate of modulus increase of *oim* collagen was significantly lower (P–value <0.001) compared to the WT one. At 0% EtOH (i.e. samples immersed in 100% PBS) the indentation modulus of *oim* collagen fibril was – (2.7 ± 0.3) MPa – statistically significant larger compared to the WT one – (1.2 ± 0.4) MPa. No significant differences

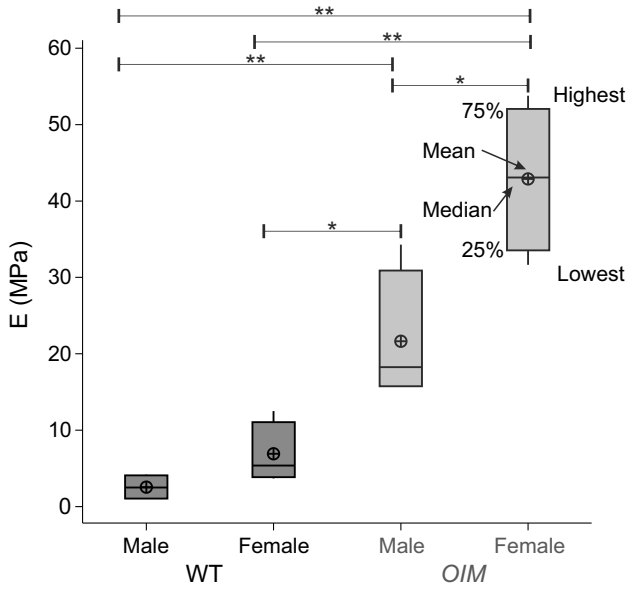

Figure 5.4: Box plots of indentation modulus of WT and *oim* collagen fibrils. Individual values correspond to averaged modulus of each fibril. The indentation modulus of *oim* collagen fibrils was ($E_{oim-♀}$ = (42.9 ± 9.6) MPa, $E_{oim-♂}$ = (21.6 ± 8.7) MPa with N = 4 fibrils each) statistically significant different (*P–value <0.01, **P–value <0.001) compared to the WT ones ($E_{WT-♀}$ = (6.9 ± 3.4) MPa, $E_{WT-♂}$ = (2.6 ± 1.7) MPa with N = 6 and N = 4 fibrils respectively). Indentation modulus values of collagen fibrils from WT animals did not differ significantly (P–value = 0.17).

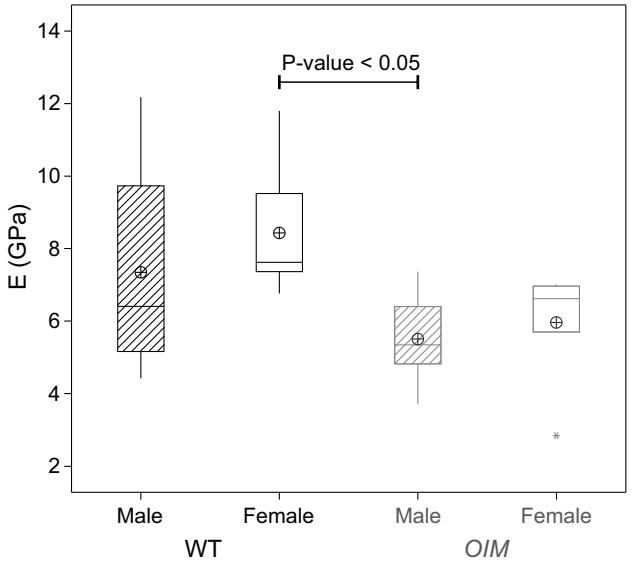

Figure 5.5: Box plots of indentation modulus of air dried collagen fibrils from WT and *oim* mice. The averaged indentation modulus of *oim* collagen fibrils in air was lower compared to the WT ones – E_{WT} = (7.9 ± 0.7) GPa and E_{oim} = (5.7 ± 0.3) GPa. Statistically significant differences were observed between collagen fibrils from the female WT and the male *oim* mice – $E_{WT-♀}$ = (8.4 ± 1.7) GPa and $E_{oim-♂}$ = (5.5 ± 1.2) GPa (P–value <0.05).

between the indentation modulus of WT and *oim* collage fibrils at 25% and 50% EtOH were found. The indentation modulus was estimated, by linear regression as shown in Figure 5.6, to be equal at about 65% EtOH. Finally, and similarly to the results from air dried samples, at 100% EtOH, i.e. dehydrated state, the indentation modulus of *oim* collagen fibril, $E_{oim-EtOH} = (453 \pm 102)$ MPa, was significantly lower (P–value <0.001) compared to the WT one, $E_{WT-EtOH} = (699 \pm 146)$ MPa. Indentation modulus values and the corresponding ethanol concentration are summarized in Table 1.

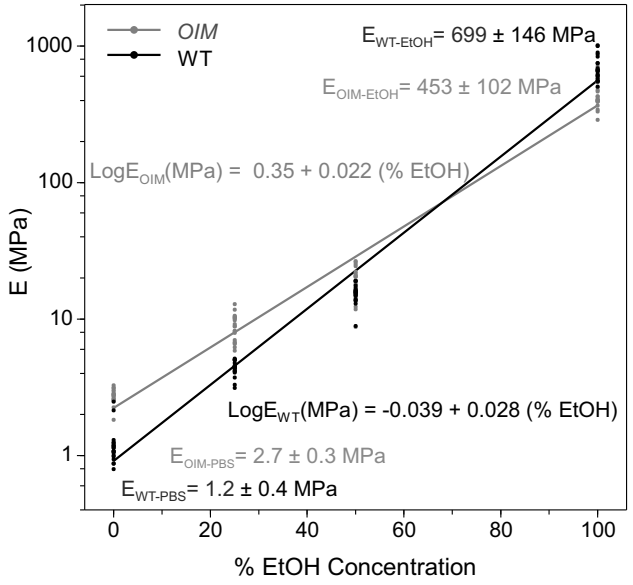

Figure 5.6: Increase of indentation modulus in increasing concentrations of ethanol diluted in phosphate buffer saline solution. The rate of increase in *oim* modulus was statistically significant (P–value <0.001) lower compared to WT one. In PBS (0% EtOH), the indentation modulus of *oim* collagen fibrils, $E_{oim-PBS} = 2.7 \pm 0.3$ MPa, fibril was significantly higher (P–valule <0.001) compared to the WT one, $E_{WT-PBS} = (1.2 \pm 0.4)$ MPa. At the dehydrated stae (i.e. 100% ethanol) the indentation modulus of WT collagen fibrils is significantly (P-value<0.001) higher compared to the indentation modulus of *oim* collagen fibrils.

	EtOH concentration	0%	25%	50%	100%
E (MPa)	**WT–male**	1.2 (0.4/20)	4.4 (0.5/19)	15.4 (2.2/20)	699 (146/21)
	***oim*–male**	2.7 (0.3/17)	8.8 (1.9/20)	19.1 (4.8/20)	453 (102/22)
	Significant difference	P–value <0.001	No	No	P–value <0.001

Table 5.1: Average indentation modulus of collagen fibrils from WT and *oim* male mice measured at increasing concentration of ethanol (EtOH) diluted in phosphate buffer saline solution. Data are presented as mean (SD/Number of tests on a single collagen fibril).

5.4 Discussion

5.4.1 Type I collagen fibrils from the *oim* mouse tail tendon exhibit 500% higher indentation modulus compared to the WT ones.

In this study, a significantly higher (more than 500%) indentation modulus of collagen fibrils from *oim* mice compared to the ones from WT was observed. This increase may be associated to a number of changes occurring at the fibril level of collagen. Such changes could include:

1. The structure and cross–linking state (i.e. collagen cross–linking) of collagen fibrils.
2. The ability to form H–bonds and the hydration level.

In the course of life, a number of biochemical changes occur in collagen fibrils. Reiser (1991); Bailey (2001) have shown that the non–enzymatic advanced glycation end products (AGEs) accumulate not only with ageing but also due to diabetes. AGEs are covalent bonds that cross–link the helical domains between adjacent collagen molecules within a collagen fibril, as have been illustrated earlier in Figure 2.2. Such biomechanical alterations in collagen fibrils have been associated with mechanical changes at the tissue level of rat tail tendon and both cortical (Tang et al., 2007) and (Vashishth et al., 2001) trabecular bone. Recently, Carriero et al. (2012) have measured significant increased in AGEs from *oim* bones. Although, direct measurements of the AGEs from *oim* collagen samples in mice tail tendons are currently lacking, a similar increase in AGEs is expected. Speculatively, the dramatic increase in indentation modulus in *oim* collagen fibrils could be partly associated with biochemical changes.

Another contributing factor in the mechanical aberration observed in *oim* collagen fibrils is the extent of hydration of these fibrils compared to WT ones. Hydration of collagen fibrils occurs naturally in biological conditions and plays an important role in the structure rigidity (Mogilner et al., 2002; Shoulders and Raines, 2009) and mechanical properties of collagen fibrils. During hydration, water is incorporated in the vicinity of collagen molecules within the collage fibril. It has been suggested, that water specifically binds the backbone structure and forms bridges in collagen molecules (Bella et al., 1995). This is achieved by the formation of hydrogen bonds (H–bonds) and hydrogen bonding networks (Bella et al., 1995, 1994).

H–bonds have been suggested to contribute in the deformation mechanisms and mechanical properties of the collagen molecule (Gautieri et al., 2009a). Studies based on molecular dynamics of collagen have shown that rearrangement and breaking of H–bonds occurs at low strains under axial deformation resulting in the toe region of the stress–strain curve (Gautieri et al., 2009a). At higher strains, the backbone structure

will dominate deformation increasing the slope of the stress–strain curve (Gautieri et al., 2009a). Experiments have also shown stiffening at both the fibril (van der Rijt et al., 2006; Yang et al., 2007; Grant et al., 2009) and tissue level of collagen (Pashley et al., 2003) with dehydration. Changes in the level of hydration of collagen fibrils may affect the extent of H–bond formation and therefore lead to mechanical impairment.

Results from AFM imaging of collagen fibrils (Figure 5.7) from a dehydrated (air dried) to a hydrated state in PBS revealed that the *oim* collagen fibrils swelled (1.6 ± 0.3 fold increase) significantly less (P–value <0.001) compared the WT ones (2.6 ± 0.4 fold increase) (Figure 5.8).

Decreased swelling could be explained by deficient functional hydration of the *oim* collagen fibrils. Presumably as a consequence of structural perturbations at the sub–fibrillar level and increased cross–linking, the lower swelling, i.e. functional hydration deficiency, in *oim* could result in rearrangement of hydrogen bonding, as has previously been proposed by Bella et al. (1994). A differential scanning calorimetry conducted by Miles et al. (2005) suggested that as the extent of collagen cross–linking changes the water content decreases. As a consequence the mechanical properties are also expected to change towards increased indentation modulus from our measurements. Less H–bonds are anticipated to form in *oim* collagen fibrils, unlike the WT ones. This would provide dominance to deformation of the backbone structure of collagen molecules during indentation and one would expect to result in stiffening of the collagen fibrils, which is supported by our evidence of increased indentation modulus in *oim*.

5.4.2 Altered hydration level and intermolecular packing in *oim* collagen fibrils

Previously, stiffening of native collagen fibrils (Grant et al., 2009) and collagen–based tissues (Pashley et al., 2003; Nalla et al., 2005) has been associated with chemical dehydration using polar solvents, such as ethanol. Chemical dehydration with ethanol displaces the water molecules within the structure of collagen fibrils resulting in rearrangement of the H-bonds. The stiffening of collagen–rich tissues has been associated with increased hydrogen bonding within collagen fibrils (Pashley et al., 2003). This was justified by the decrease of the inter–molecular lateral spacing resulting in a closest packing of collagen molecules and hence allowing more H–bonds to be formed. This suggests that increasing ethanol concentration in the PBS solution would constantly increase the number of H-bonds within the collagen fibril. Pashley et al. (2003); Nalla et al. (2005) suggested that increasing the ethanol (or other polar solvents) concentration in an aqueous solution would indirectly increase the number of H–bonds within the collagen fibril.

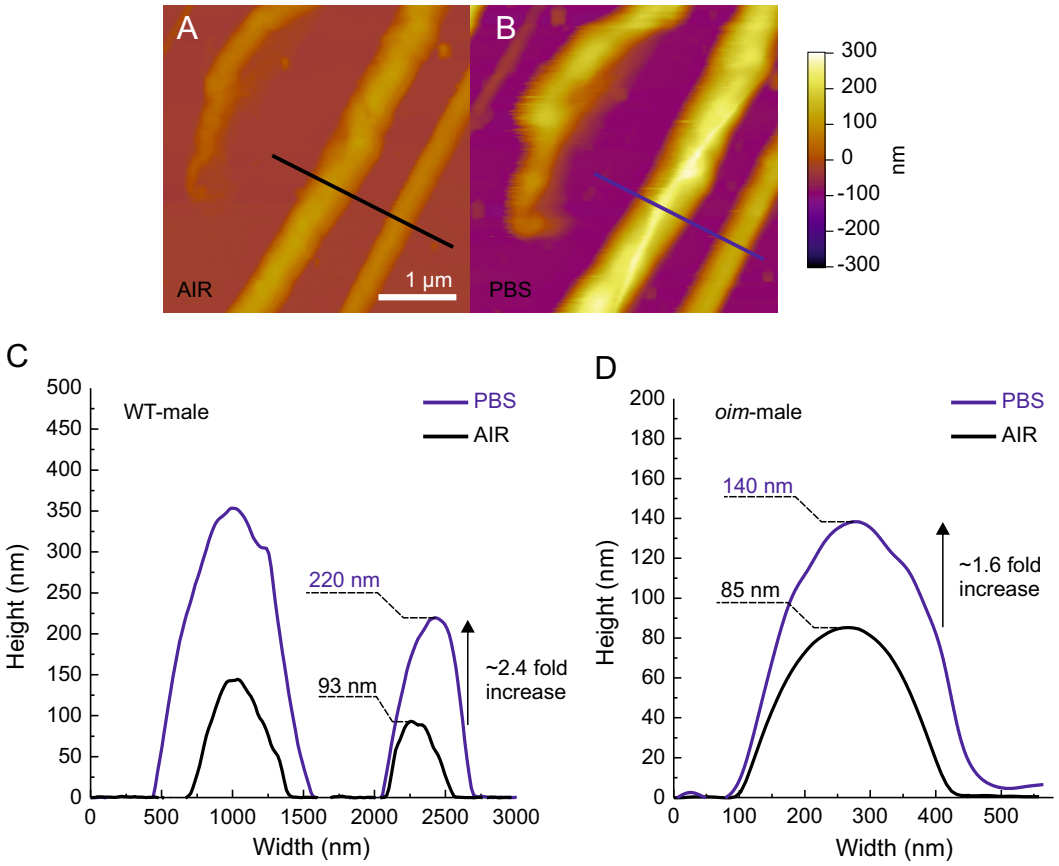

Figure 5.7: Swelling of collagen fibrils with incorporation of an aqueous solution. Panels A and B shows AFM height topography images of collagen fibrils from WT mouse imaged in air and PBS, respectively. Panels C and D shows line profiles of the cross–section of collagen fibrils originated from male WT and *oim* mice, respectively.

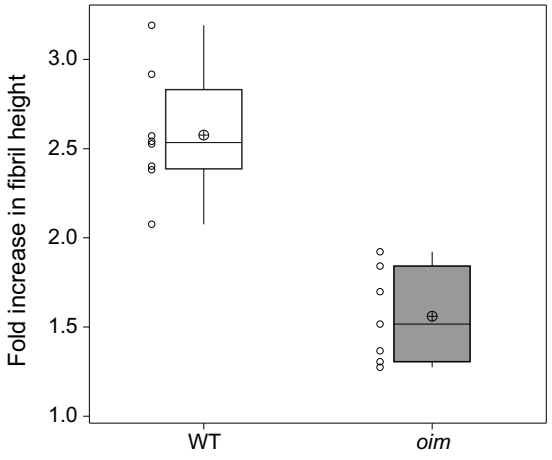

Figure 5.8: Fold increase in height of WT and *oim* male collagen fibrils. The height of WT collagen fibrils increased in by (2.6 ± 0.4) times whereas the height of *oim* collagen fibrils increased only by (1.6 ± 0.3) times.

Considering the above proposed effect of ethanol, our results (Figure 5.6) suggest that

less H–bonds would form in *oim* collagen fibrils compared to WT ones, with increasing the ethanol concentration. The lower indentation modulus of *oim* collagen fibrils at 100% EtOH, compared the WT one, suggest that the fibrillar structure is disturbed inhibiting formation of H–bonds.

Additionally, the *oim* collagen molecule has larger and more kink formations (Chang et al., 2012). These authors suggested that the packing of *oim* collagen molecules into fibrils could be impaired due to kink formations. Miles et al. (2002) estimated a 7% increase in the intermolecular lateral distance. By assuming a triclinic unit cell for the unit cell volume of the collagen fibril, as suggested by Orgel et al. (2006), the dried *oim* microfibril has 14% decreased volume due to the increase in intermolecular lateral distance (Markus Buehler and Shu–Wei Chang, personal communication). Undoubtedly, changes in the packing of collagen molecule could result in changes of the density of the collagen fibrils which is here reflected as alterations in the indentation modulus.

5.5 Conclusions

In this study, results on the mechanical and structural abnormalities at the fibril level of collagen using AFM cantilever–based nanoindentation and molecular dynamics were presented. These results show how defects at the molecular level of collagen results in changes of collagen mechanics at the fibril level. Experimentally *oim* collagen fibrils are stiffer in physiological solution. Additionally, it appears that *oim* collagen fibrils do not swell as much as the WT ones when going from air dried state to a hydrated state with PBS. Although the mechanism is not fully understood, results from another study (Carriero et al., 2012) suggests that the difference in hydration behaviour of *oim* collagen fibrils is likely due to a significant increase in AGEs crosslinks compared to WT collagen. This hypothesis is further supported by evidence of decreasing volume fraction of water with increasing cross–linking in collagen (Miles et al., 2005). Decreased swelling could be associated with less functionally hydrated fibrils resulting in higher indentation modulus. Results of indentation modulus at the fully dehydrated state suggested that the *oim* collagen fibrils are less dense. This is supported by the computational model suggesting increased inter–axial distance between the collagen molecules. Miles et al. (2002) have previously proposed an increase in inter–molecular distance in the *oim* collagen fibrils based on their findings showing increase volume fraction of water. Experimental findings from this study showed how biological important changes in the structure at the molecular level of collagen affect the mechanical competence of the fibrils at the hydrated state. Additionally, this study results link experimental and computation findings complementing on the relationship of structure–mechanical properties which was evident at the fully dehydrated state. A possible explanation of the increased brittleness of *oim* mouse bone from the results presented here would be that the histochemistry of *oim* type I collagen is changed, such that the deformation mechanisms present in

healthy type I collagen are no longer present in the *oim* collagen. As a consequence the ductility of fibrils is expected to be reduced and one would expect this to lead to more brittle behavior of the biocomposite bone as a whole. Further application of AFM cantilever–based nanoindentation can lead to cataloguing different pathological collagen phenotypes and their correlated mechanical properties as well as associated mechanical impairment.

Chapter 6

Effect of biochemistry on the nanoelasticity of collagen fibrils assessed by AFM

6.1 Background

Collagen is the most abundant structural protein in the human body. It composes the majority of the extracellular matrix of both hard and soft tissue such as bone, skin, the respiratory system, tendons and cartilage. Biomechanically speaking, collagen is one of the most important proteins. As mentioned in chapter 5, collagen biochemistry changes over the life–course and such changes have been associated with mechanical alterations at the tissue level. Although, tissue mechanics have been linked with biochemical changes of collagen they have not directly been linked with changes at the fibril level of collagen. Additionally, to the best of our knowledge little is known about how the biochemistry affects the mechanical properties at the level of the basic structural element, i.e. the individual collagen fibril.

As described in chapter 2, there are two types of collagen cross–links depending on the formation pathway; the enzymatic and non–enzymatic ones. During fibril formation, the collagen molecules are staggered to form a cylindrical structure which is rigidified by immature enzymatic cross–links (Eyre and Wu, 2005). The immature cross–links inter–connect the telopeptide of one collagen molecule to the helical domain of an adjacent one (Reiser et al., 1992). Over time the immature divalent cross–link undergoes chemical reformation resulting in a mature trivalent cross-links which now inter–connects a third molecule (Bailey, 2001; Avery and Bailey, 2008). During ageing, non–enzymatic glycation takes place resulting in the formation of glucose–mediated cross–links which accumulate in the vicinity of the helical domains between adjacent collagen molecules. These three different cross–are graphically summarized in chapter 2, 2.2.

Although there are biochemical changes in collagen fibrils with time, such changes may also be present in disease. For example, the airways in patients suffering from chronic asthma are characterized by chronic inflammation and, collagen accumulation leading to airway obstruction that fluctuates over time (Holgate et al., 2010). One of the main features of asthma is airway wall thickening due to subepithelial fibrosis, i.e. accumulation of collagen in the submucosa. Subepithelial fibrosis has been associated with disease severity and negatively correlated with FEV1% (Force Expiratory Volume at first second) (Chetta et al., 1997; Bradding et al., 1997). It becomes clear that the structural changes of collagen–tissue morphology in the airways of severe asthmatic may be associated with mechanical dis–functionality. Another characteristic feature of asthma is airway hyperresponsiveness (AHR is defined as a sudden constriction of the airway smooth muscles surrounding the bonchioles). Studies that have associated the methacholine sensiticity with the extent of subepithelial fibrosis (Boulet et al., 1995; Hoshino et al., 1998) converge to the hypothesis that there is also a direct association of the smooth muscle behaviour with the quality of their environment. In fact, a study by Chu et al. (1998) showed that collagen deposition was not indicative for distinction between mild and severe asthmatics. Al the above composes the complexity of the development of asthma and lead to the hypothesis that there well may be changes in the biochemistry–mechanics relationship apart from the structure–mechanics in collagen fibrils.

To test this hypothesis we have measured the indentation modulus of collage–rich tissue from three bronchial biopsies that were matched with an non–parallel immunohistochemistry study which provided measurements of the immature to mature cross–link ratio, indicative of the prevalent cross–link from the given samples. To test the hypothesis that accumulation of AGEs lead to an increase in the indentation modulus of collagen fibrils, we treated sections of mouse tail tendon with ribose for three (3) and five (5) days. We have additionally compare indentation modulus results of individual collagen fibrils from healthy and chronic asthmatic subjects.

6.2 Materials and Methods

6.2.1 Isolation of collagen fibrils from human bronchial biopsies

Collagen fibrils were isolated as described in 4.2.1.2. Briefly, the biopsies were incubated in separate wells for 24 hours into 0.1M Sorensens phosphate buffer (pH 7.2) containing 1 mg/ml bovine hyaluronidase and 1 mg/ml trypsin. After incubation, samples were washed with deionized water (Millipore) then placed and smeared out on glass slides to reveal areas with individual fibrils. All biological products were left in an incubator to dry at 37^oC overnight after deposition on the glass slides and then kept in a storage box

with silica gels. Sample preparation from human bronchial biopsies was performed by Ms Wiparat Manuyakorn[1].

6.2.2 Ribose treatment

Sample preparation and treatment with ribose were performed by Dr. David Smart[1].

Collagen strands were collected from mouse tail tendon sections using needle forceps and placed in Hank's Balanced Salt Solution (HBSS) containing 30mM HEPES, pH 7.4 and a broad spectrum protease inhibitor cocktail. Non–enzymatic glycosylation was mimicked in half the samples by the addition of 0.6M Ribose to HBSS. Both groups were incubated at 37^oC with the solutions and protease inhibitors being replaced every 1 to 2 days over the time course of the experiment. Samples were harvested from both the Ribose and Ribose free HBSS at each time point. To expose individual fibrils, the larger fibres were placed onto poly–l–lysine coated glass slides and separated using the points of two scalpels. The samples were then air dried before washing in ultrapure water and air dried prior to atomic force microscopy (AFM) experiments.

6.2.3 AFM imaging and cantilever–based nanoindentation

AFM experiments were carried out in a temperature – $(20.7 \pm 0.7)\ ^oC$ – and humidity – (47.9 ± 6.7) % – controlled room using the MFP–3D atomic force microscope (Asylum Research, Santa Barbara, CA, USA). Images of individual collagen fibrils were obtained in tapping mode at about 1 Hz scanning rate.

For nanoindentation tests on collagen fibrils from human bronchial biopsies the AC200 cantilevers with spring constant of (8.3 ± 1.8) N/m with about 7 nm tip radius (AC200, Olympus) were employed. For testing the murine collagen fibrils the NSC cantilever with (49.6 ± 7.4) N/m spring constant and 10 nm tip radius (MicroMasch) were used. Nanoindentation experiments were carried out under force control at 30 nN and 200 nN maximum load for human and murine collagen fibrils, respectively. Force Volume (FV) maps were recorded on collagen–rich areas from three biopsies, as illustrated in Figure 6.1. To determine the spring constant of each AFM cantilever the thermal noise method was employed as proposed by Sader et al. (1999).

6.2.4 Statistics

Statistical analysis was performed in Minitab 16.2.4. A two–sample t–test was performed to test differences between asthmatics and healthy groups. To test normality

[1]The Brooke Laboratories, Clinical and Experimental Sciences, Division of Infection, Inflammation and Immunity, University of Southampton, Faculty of Medicine, Southampton, UK.

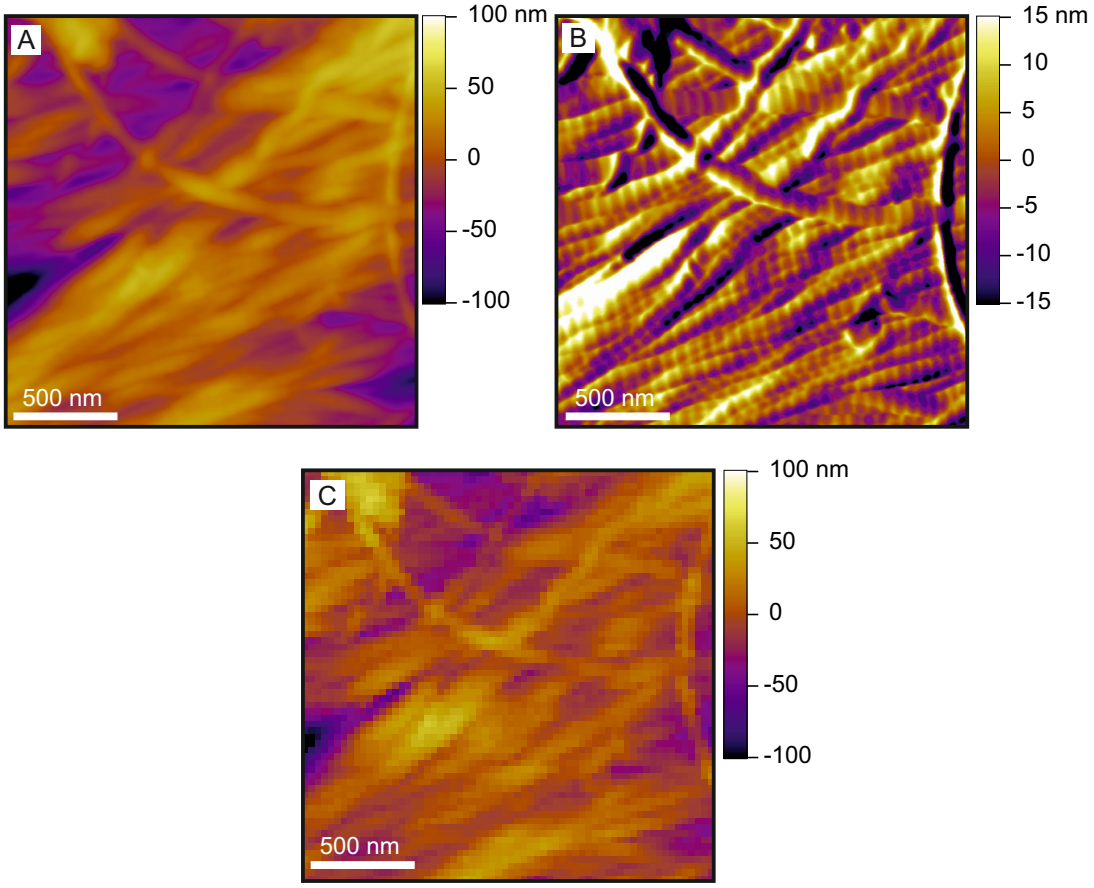

Figure 6.1: Panels A and B show the AFM height and amplitude images of a $2\mu \times 2\mu$m area of a dried bronchial biopsy respectively. Panel C corresponds to the force volume map of that area.

the Kolmogorov–Smirnov test was performed. To correct for unequal variance among the data, transformations were applied appropriately such as the normal logarithm. The generalized linear model (GLM) was performed to test differences indentation modulus of collagen fibrils from asthmatics and healthy individuals. Results were considered to be significant for P–value <0.05. Unless otherwise specified, data are presented as mean $\pm$ standard deviation.

6.3 Results

6.3.1 Effect of enzymatic cross–links

Results from the nanomechanical evaluation of collagen fibril sections, as presented in Figure 6.2, suggested a trend of decreasing indentation modulus with predominance of the immature divalent cross–links, from measurements of immature to mature aldimine ratio. For about equal amount of immature and mature aldimine cross–links (ratio

=1.09) the indentation modulus was found to be 3.42 GPa (95% CI:3.45 to 3.38 GPa), for ratio=2.51 the indentation modulus decreased slightly to 3.04 GPa (95% CI:3.18 to 3.00 GPa) while there was a greater decrease down to 2.20 GPa (95% CI:2.23 to 2.18 GPa) for ratio=3.37.

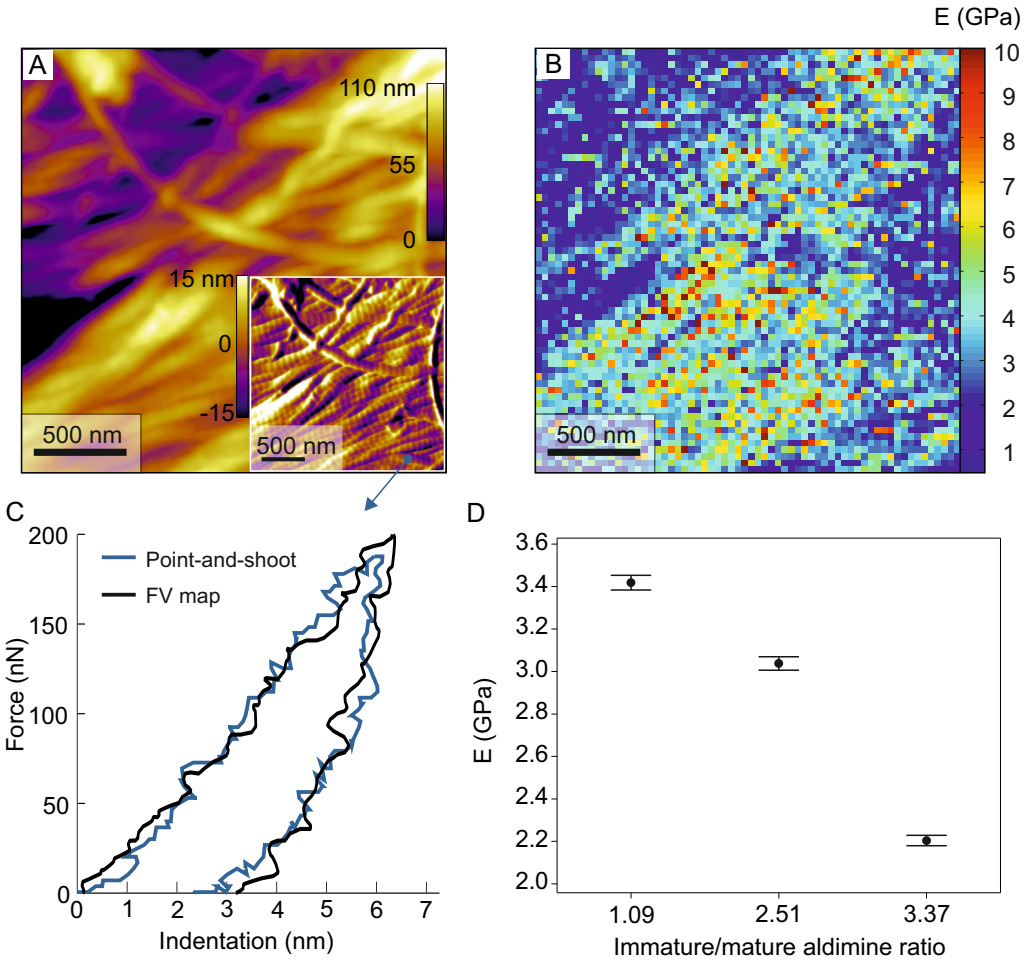

Figure 6.2: Panel A shows an AFM height image of a collagen tissue section from a bronchial biopsy. The inset in panel A shows the corresponding AFM amplitude image. Panel B shows two force–indentation curves retrieved from the area shown in panels A and B. The blue solid curve was collected by indenting the crest of a collagen fibrils by point–and–shoot operation. The black solid curve corresponds to a force–indentation curve which corresponds to the mean indentation modulus value of this area. Finally the indentation modulus is plotted against the immature to mature aldimine ratio for these specific biopsies.

6.3.2 Effect of non–enzymatic cross–links

Significant differences (P–value <0.001) were observed between the indentation modulus of ribose treated collagen fibrils compared to the ones incubated in ribose free (HBSS) and the control sample. More specifically, the indentation modulus of collagen fibrils increased to (10.2 ± 1.8) GPa and to (15.8 ± 0.7) GPa after 3 and 5 days of incubation

in solution with ribose, respectively. Interestingly, there was also an increased observed in collagen fibrils incubated in HBSS – (4.6 ± 0.6) GPa – compared the control sample – (2.6 ± 0.2). Results are presented below in Figure 6.3.

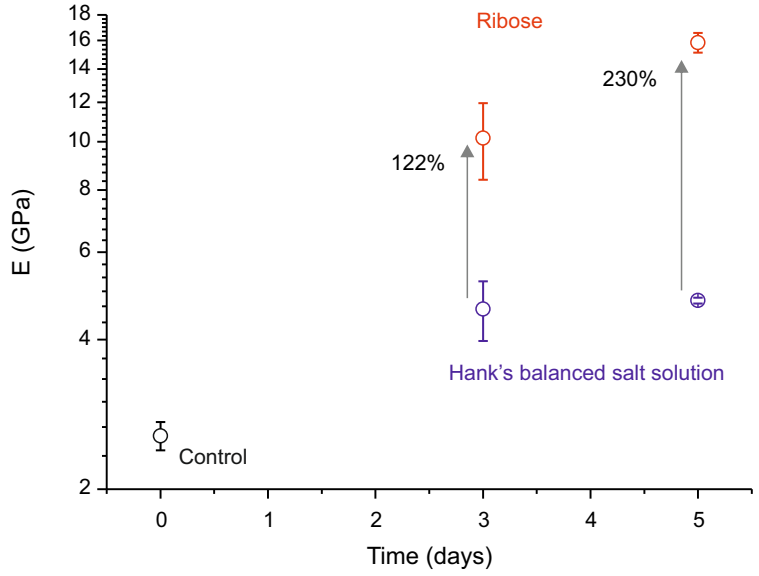

Figure 6.3: Indentation modulus increased up to about 500% from control to five days of treatment in ribose solution. There is also a marked increase (of about 85%) in indentation modulus of collagen fibrils incubated in the ribose free solution (HBSS, Hank's Balanced Salt Solution).

			E (GPa)
Time (days)	*0*	*3*	*5*
Control	2.6 (0.2)	n/a	n/a
Hank's buffer	n/a	4.6 (0.6)	4.8 (0.1)
Ribose	n/a	10.2 (1.8)	15.8 (0.7)

Table 6.1: Comparison of indentation modulus of collagen fibrils incubated in ribose, Hank's buffer (ribose free) with the one from control sample. Data are presented as mean (standard error of the mean).

6.3.3 Close to significant trend of lower indentation modulus in collagen fibrils from asthmatics

The indentation modulus of collagen fibrils from asthmatics was found to exhibit – (0.85 ± 0.24) GPa – a trend towards lower values compared to the healthy ones – (1.25 ± 0.36) GPa – but this was just not significant (P–value=0.05). In principle, there is not enough evidence to conclude that the mean of indentation modulus differ at the 0.05 level of significance between asthmatics and healthy individuals. This is most likely because of the sample size (n=5 asthmatics and n=7 healthy individuals). The P–value

may decrease with increasing the sample size resulting in stronger statements regarding significance of results (personal discussions with statistician).

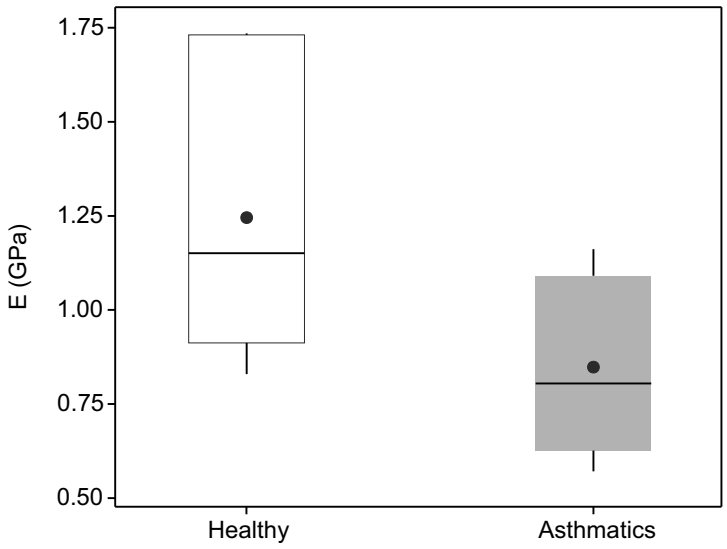

Figure 6.4: Box plots of indentation modulus of collagen fibrils from asthmatics ((0.85 ± 0.24) GPa, n=5 individuals) and healthy ((1.25 ± 0.36) GPa, n=7 individual) individuals.

6.4 Discussion

6.4.1 Collagen fibrils mechanics may degrade with predominance of immature divalent cross–links

Only three from the 20 bronchial biopsies, overlapped by chance with an unparalleled biochemistry study conducted by collaborators at the University of Aberdeen (Principal investigator: Prof. Simon Robins). The biochemistry study provided a relative amount of immature compared to mature aldimine cross–links for each sample. Likely, our AFM mechanical assessment shows a decreasing trend of indentation modulus as the immature to mature aldimine ratio increases (Figure 6.2). However, Due to the small sample size (N=3 biopsies) it cannot be said with certainty that the indentation modulus is negatively correlated with the immature to mature ratio of the collagen fibrils. However, these are tantalizing evidence that as the immature cross–links predominate in collagen fibrls the indentation modulus (i.e. nanoelasticity) decreases.

The inter–molecular distance of collagen within the collagen fibril, is expected to decrease with subsequent cross–linking (Bailey, 2001; Miles et al., 2005). This is supported by evidence on the volume fraction of water of artificially cross–linked collagen fibrils (Miles et al., 2005). This results in more dense fibrils which will become stiffer upon indentation.

A substantial increase in cross–linking is more defined with accumulation of advanced glycation end products presented in the next section.

6.4.2 Artificially induced AGEs are directly associated with increased collagen fibril mechanics

A previous study have shown an increase in AGEs with increasing the time of incubation (Vashishth et al., 2001) of bone samples. Considering the above, we have clear evidence that increasing the amount of AGEs directly affects the mechanical behaviour of collagen fibrils to about 230%. According to Miles et al. (2005) and to the findings presented in chapter 5, accumulation of AGEs are expected to result in decreased swelling of these fibrils. One explanation would be that collagen molecules are tightly packed due to increased AGEs, which inter–connect adjacent molecules. These inter–connections would not, therefore, allow the fibrils to absorb more water than the ones which are not cross–linked. As discussed previously, these leads to significant impairment of collagen fibril hydration which is thought to be important for maintaining the toe region under deformations at low strains.

Although the difference between the HBSS incubated and control sample was not statistically significant (P–value >0.05) it was approximates to about 85%. Current experimentation cannot justify with certainty the origin of the change. However, it is suspected that precipitation of minerals during the incubation period may have occurred. Further experiments on the samples incubated in HBSS need to be conducted to address the question in regards to what have caused this increase. Alternatively experiments could be repeated using PBS as a liquid, than HBSS.

6.4.3 The complexity in collagen mechanics in asthma

The difference in indentation modulus observed between asthmatics and healthy individuals may not be significant but could potentially provide a new hypothesis that could serve as the basis for further experimentation. This can only be accomplished in consideration with all the above results from this chapter and chapter 5.

One possible explanation of the decreased indentation modulus in asthmatics could be predominance of the immature divalent cross–links. However, the biochemistry results are rather controversial showing a great variability of immature to mature ratio ranging from less than 1 to about 7 fold difference. This great variability could be explained by different rates of collagen formation and degradation. Some patients may be characterized by increased formation rather than degradation which in the long term result in collagen fibril deposition and maturation. Hence, low relative amount of immature to mature cross–linking. Another, however, group of patients may well degrade collagen

more than they form resulting in higher amount of immature to mature ratio. In other words, asthmatic individuals may possess different behaviour of collagen turnover. This hypothesis seeks of further testing which can be accomplished by investigating serum markers of collagen formation and degradation (Heuck et al., 1997).

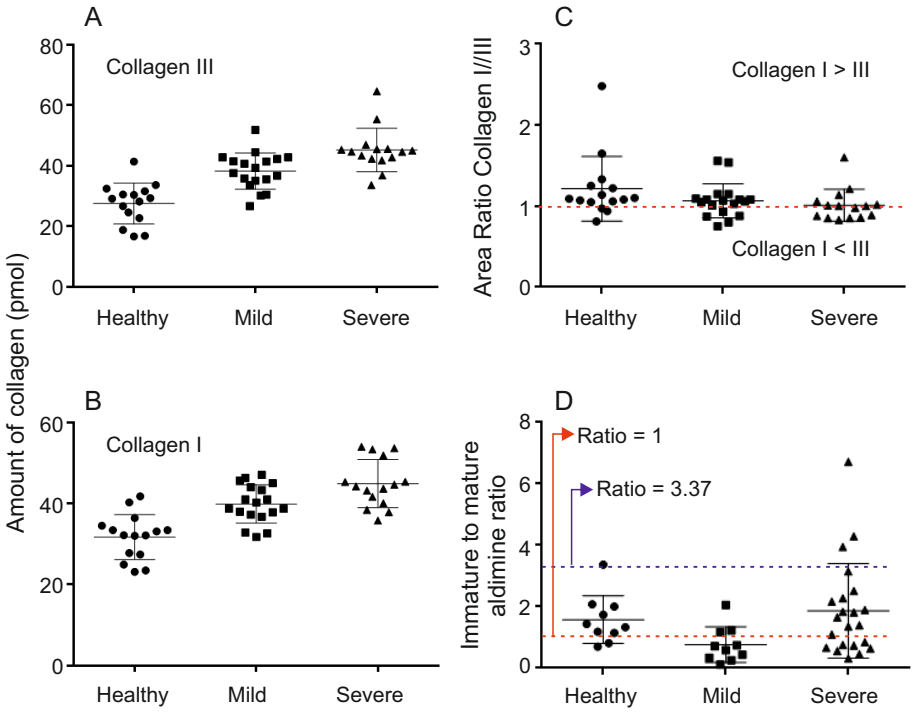

Figure 6.5: Results from an independent immunohistochemistry study. Panels A and B show an increase in total amount of both collagen types III and I respectively. Panel C shows the relative amount of collagen I to III. Panel D shows the relative amount of immature to mature aldimine cross–links.

In addition, the effect of ribose (i.e. glycation–related cross–links related to age of individual) on the indentation modulus suggests that collagen fibrils originated from older individuals would be stiffer. However, the age of healthy individuals ranged between 19 to 23 years old and one individual was 54 years. On the other hand the age of asthmatic individuals ranged between 33 to 45 years. This suggests more mature and glycated (AGEs) collagen fibrils i.e. increased indentation modulus to be observed in samples from asthmatic ones. However, this was not the case for indentation modulus as we rather observed a decrease in asthmatics (Figure 6.4). Currently, we do not hold information about the amount of AGEs. However, the biochemistry study (conducted unparalleled to the atomic force microscopy study by Prof. Simon Robins) suggested a great variability in the immature to mature aldimine ratio (Figure 6.5). Results from the biochemistry study also showed an increase in total amount of both collagen types III (Panel A in Figure 6.5) and I (Panel B in Figure 6.5) and a trend of increasing type III collagen relatively to collagen type I. This study however has experimental limitations and doubts exists regarding the measurements of total amount of collagen (results shown in panels A–C in Figure 6.5).

Perhaps the most intriguing result is the obvious increased variability of immature to mature aldimine ratio in patients with severe asthma. A number of biopsies were characterized by larger amount of mature aldimine cross–links (Ratio <1, red dashed line) which was also and mainly the case for patients with mild asthma. Additionally another great amount of biopsies from severe asthmatic patients were characterized by increased amount of immature cross–links ranging from 2 to 8 fold difference. The drawback here is that only three biopsies measured with AFM overlapped with immunohistochemistry data and results are shown above in Figure 6.2. Further limitations exist in current measurements of the total and relative amount of collagen because they are based in area estimations stained with antigens for collagen types I and III. This means that, although the technique is accepted, it only provides with the amount of collagen types on the surface of the biopsy. This could be solved by performing truly quantitative assays, e.g. Western Blotting, which provides a better estimation of the relative amount of proteins in the biopsy.

6.5 Conclusions

Here we have presented results from AFM nanomechanical investigations on collagen fibrils originated from bronchical biopsies from asthmatics and healthy individuals. Our results suggested a decreasing trend of indentation modulus with increasing the amount of immature cross–links. Further we observed a trend towards decreased indentation modulus in collagen fibrils obtained from asthmatic bronchial biopsies, however, this was close to significant (P–value=0.05). The origin of collagen fibril mechanics in asthma are difficult to elucidate with the current results. However, a number of studies will be carried out from collaborators to help us understand these changes. Unfortunately, the biochemistry study was conducted unparalleled for the majority of the samples and thus we do cannot investigate further to associating the biochemistry to our AFM results. Additionally we have tested the hypothesis of increasing indentation modulus with increasing the AGEs. This study showed a significant increase in indentation modulus with increasing the incubation time of the sample in ribose solution. Further experiments are needed to draw conclusions with certainty in regards to the collagen cross–linking in asthmatics and its association with indentation modulus and mechanical properties of the airway lumen. Experiments would include truly quantitative assays, such as Western Blotting, to provide a more reliable measurements of amount of collagen types present and their relative amount. In addition, bronchial biopsies, which have been mechanically assessed with AFM cantilever–based nanoindentation, are to be also assessed for the types and amount of cross–links. Further to AFM experiments, data retrieved from more patients are analysed which would make clear the significance of the difference between asthmatics and healthy individuals. Future work is also planned

to mechanically assess biopsies at the tissue level. tissue mechanical properties are also to be tested planned to test even more fibrils under physiological conditions.

Chapter 7

Discussion and conclusions

In this chapter the main findings of the PhD thesis are discussed and the current limitations are pointed out. A number of suggestions are presented for optimizing experiments, analysis methods and testing a number of hypotheses that suggested from the results.

7.1 Thesis outcomes, experimental limitations and future work

7.1.1 Validation study of nanomechanical assessment of collagen fibrils with AFM

The validation study showed that the atomic force microscopy cantilever–based nanoindentation can be successfully applied to indent collagen fibrils with diameter of 30 nm. In addition, the continuous indentation testing with increasing the indentation depth showed that the 10% Bueckle's rule should be followed to avoid the effect of substrate on the measured values of stiffness and indentation modulus. This is important to delivering reproducible results. Comparing results from AFM–cbN and conventional nanoindentation suggests a good agreement between the two techniques, however, the lack of a gold standard technique does not enables us to perform a thorough calibration of the determination of the AFM tip area function. The lack of a gold standard sample raises a number of limitations when using other polymer samples:

a. Geometrical features such as surface roughness and geometrical shape of the sample (i.e. cylinder in the case of collagen fibrils) can be responsible for part of the variation of data. In this sense, topography information could and should also be used to discriminate and exclude data from analysis optimizing the outcomes.

b. The contact area, between the tip and the sample, depends highly on the tip geometry. Variations on the assumptions made to estimate the tip geometry can cause changes in the indentation modulus. This is possibly responsible for the larger effect on the accuracy of the measurements. We have used a method to reconstruct the tip shape by imaging a spike and using a deconvolution algorithm (as suggested by Keller and Franke (1993)) to extract the tip shape. AFM cantilever–based nanoindentation on polymeric samples with known mechanical properties were tested and indentation modulus was comparable to the one determined via conventional nanoindentation. These results also suggest that the reconstruction procedure used to deconvolute the AFM tip shape provides with rather reliable measurements of the contact area.

c. Determination of the contact depth is essential for optimizing the quantitative character of AFM cantilever–based nanoindentation. In conventional nanoindentation a correction factor is used to estimate the contact depth. According to Pharr and Bolshakov (2002) the geometric correction factor depends on the "effective shape" of the indenter and can be demonstrated as a function of the exponent value, n, of Equation 3.7 (power law function used to fit the unloading part of the force–indentation curve) (Oliver and Pharr, 2004). Introducing the value to our analysis we expect a relative increase of the indentation modulus. An ideal optimization would be to determine the correction factor specifically for each analysed force–displacement curves which is characterized by a certain exponent value, n (dimensionless) by (Pharr and Bolshakov, 2002):

$$\varepsilon = n\left(1 - \frac{2\Gamma\left(\frac{n}{2(n-1)}\right)}{\sqrt{\pi}\Gamma\left(\frac{1}{2(n-1)}\right)}(n-1)\right) \tag{7.1}$$

where Γ is the the "gamma" function.

d. The analysis method used can also affect the resulting indentation modulus. Several analysis methods exist to analyse data from nanoindentation tests. Assumptions amongst the various methods differ and in consequence the resulting indentation modulus values often differ as well. One particular analysis method must be selected to analyse all data for meaningful comparisons. Experimenters are also urged to compare their values with literature only if the same analysis methods have been used. Also experimentation and analysis methods should be described in detail to allow cross–comparison of results obtained by different groups and different studies.

e. Beyond the practical limitations in experiments and analysis methods the physicochemical properties of the sample (in our case the collagen fibrils) must also be considered. The type and amount of inter–molecular cross–links seems to be determinant of collagen fibril nanoelasticity.

Although there are limitations associated with the small size of the AFM tip and the nanoscale structural inhomogeneity of the tested sample, the technique can deliver important information about the elastic properties at the nanoscale.

7.1.2 Altered structure–mechanical relationship of collagen fibrils from the *oim* mouse model

The validation study enabled us to apply the technique in the *oim* mouse model, which is known to produce structurally abnormal collagen molecules and most probably fibrils.

The indentation modulus of hydrated *oim* collagen fibrils was significantly higher than that of WT collagen fibrils. In addition, the *oim* collagen fibrils swelled less compared to WT ones. The decreased swelling suggest lower hydration level of *oim* collagen fibrils which explains the increased indentation modulus. Recently, Carriero et al. (2012) have observed increased AGEs (advance glycation end products) in *oim* bones. Miles et al. (2005) have associated the water content in collagen with increased cross–linking. However, Miles et al. (2002) have found increased water content in the *oim* collagen fibrils, which fails to explain the decreased swelling observed in this study. The controversy between high water content (Miles et al., 2002) and low swelling in *oim* (present study) could be explained by increased lateral spacing within the *oim* collagen fibrils. When fibrils were immersed in pure ethanol solution, the indentation modulus of *oim* collagen fibrils was significantly lower than that of WT ones. This suggests that *oim* collagen fibrils have lower density. Chang et al. (2012) have shown structural alterations in the *oim* collagen molecule, and further suggested lower packing of collagen molecules into fibrils.

The WT collagen molecules are more tightly packed into collagen fibrils compared to the *oim* collagen molecules, due to local kink formations (Chang et al. (2012), results from dehydrated collagen fibril from current study). Upon hydration, water molecules binds the structure forming bridges that inter-connect collagen molecules. This functional water causes substantial swelling to the WT fibril. However, we anticipate that water molecules will not be able to form these bridges at the locations with local kink formations because of increased inter-molecular lateral distance. In other words, larger amount of water would be needed to feel the gaps in *oim* collagen fibrils, explaining the increased water content, without contributing to functional hydration.

The results from this study have associated structural changes of collagen molecules to their altered mechanical properties. This provides further understanding of how important the structural integrity is for the improved mechanical function of collagen fibrils and thereafter collagen–rich tissues. Further, to understanding the structure–mechanical function of collagen fibrils, the study confirmed our hypothesis to employ the AFM–cbN for investigating changes in the mechanical properties of collagen fibrils.

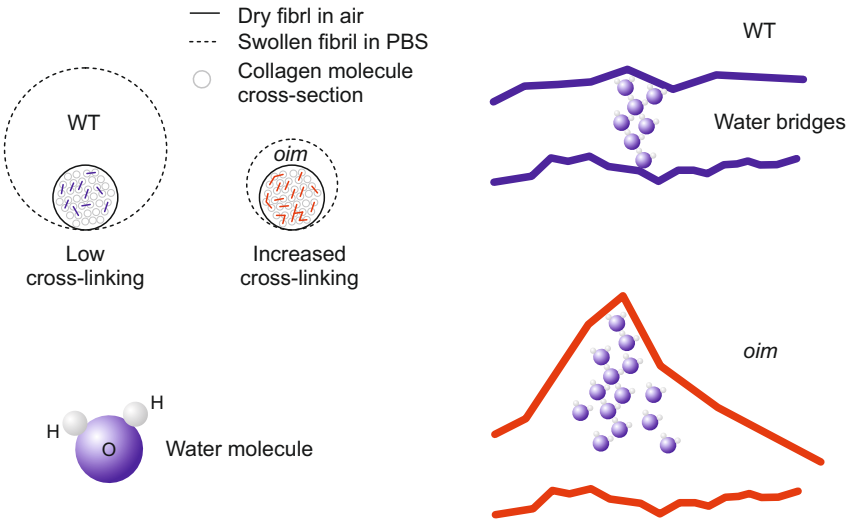

Figure 7.1: Swelling in *oim* collagen fibrils is hindered because of increased cross–linking and because of deficient functional hydration. The latter case is expected to be a result of higher inter–molecular lateral distance in *oim* collagen fibrils.

As a result, the technique can be applied to a number of other collagen–related diseases, and further provide better understanding of the effect of cross–linking on the mechanical properties of collagen fibrils.

7.1.3 The amount and type of cross–linking are strong determionants of collagen fibril mechanics

Whilst the immature to mature aldimine cross–linking ratio increase there was a trend towards lower indentation modulus. Incubating collagen–rich sample in ribose solution increase the amount of AGEs in collagen fibrils. (Vashishth et al., 2001). The indentation modulus increased with the duration of incubation. Extensive cross–linking is known to reduce hydration of the collagen fibrils (Miles et al., 2005) which will also have substantial effects in the mechanics at physiological conditions.

Chemically treated collagen fibrils were tested in air dried conditions. This is the main limitation of the study, because it cannot deliver information regarding the hydration. However, these findings lead to the hypothesis of increased density of collagen fibril with increased cross–linking.

In summary, both the type and amount of cross–linking influences the indentation modulus of collagen fibrils. It is suggested that the presence of more immature collagen fibrils, compared to the amount of mature cross–links, would allow more hydration since the fibril is less cross–linked, i.e. less bridges are present that inter–connect collagen molecules. These results could potentially be beneficial to validate molecular dynamics

simulations and potentially be used as predictive tools to assess the mechanical properties of collagen fibrils by only knowing their chemical state.

7.1.4 Nanomechanical alterations in asthmatic biopsies at the fibril level of collagen

According to the concept of mechanical implications in chronic asthma collagen fibrils from bronchial biopsies of asthmatics were tested and compared to healthy ones. This revealed a lower indentation modulus in collagen fibrils from asthmatics compare to healthy subjects. This may be explained by the biochemistry of collagen cross–links in asthmatics. The immunohistochemistry study conducted unparalleled (by Prof. Simon Robins and co–workers) presented in this thesis has shown increased amounts of collagen deposited in the submucosa (subepithelial layer) of asthmatic patients. In addition, a number of bronchial biopsies from asthmatics were characterized by immature collagen fibrils. These results suggested a large variation of relative amount of immature to mature cross–links between asthmatic patients. Based on the cross–linking study, a decrease in indentation modulus with increasing the ratio immature to mature cross–links, was anticipated.

Conclusions regarding the effect of cross–linking can be drawn only for specific biopsies tested, because the available immunohistochemistry data overlapped only with three of the biopsies at hand. For these biopsies, we observed a trend towards a decrease in indentation modulus whilst the immature cross–links predominate. This shows

Further studies are to be developed to assess the mechanical properties of bronchial airway to better understand the mechanical implications in asthma and perhaps other pulmonary diseases with altered tissue remodelling.

a. Analysis of further data to confirm the effect changes in asthma on the indentation modulus of collagen fibrils.

b. Experiments to test the hypothesis of increased variation of indentation modulus within individual donors. This hypothesis is based on the accumulation and increased turn over of collagen fibrils in asthmatics. To test this hypothesis the tested collagen fibrils from each donor should be increased to at least 10 per sample.

c. Experiments to elucidate the tissue level mechanics. Such experiments can be accomplished by performing similar nanoindentation tests with an AFM cantilever. In this case, however, glass microspheres are firmly attached at the edge of an AFM. The diameter of the microspheres could range from 5μm – to 50μm, as shown in Figure 7.2. The microsphere are then used to indent the surface of the sample up to about 200 nm indentation depths. We have validated the technique by testing mouse

lung tissue sections from parenchyma at fully hydrated state incubated in PBS solution. From such experiments we could map the indentation modulus over the tested area, as shown below in Figure 7.3, and also provide quantitative results linking the percentage of surface with a particular range of indentation modulus. Unfortunately it was not possible in the course of the PhD project to obtain human biopsy samples prepared for these experiments.

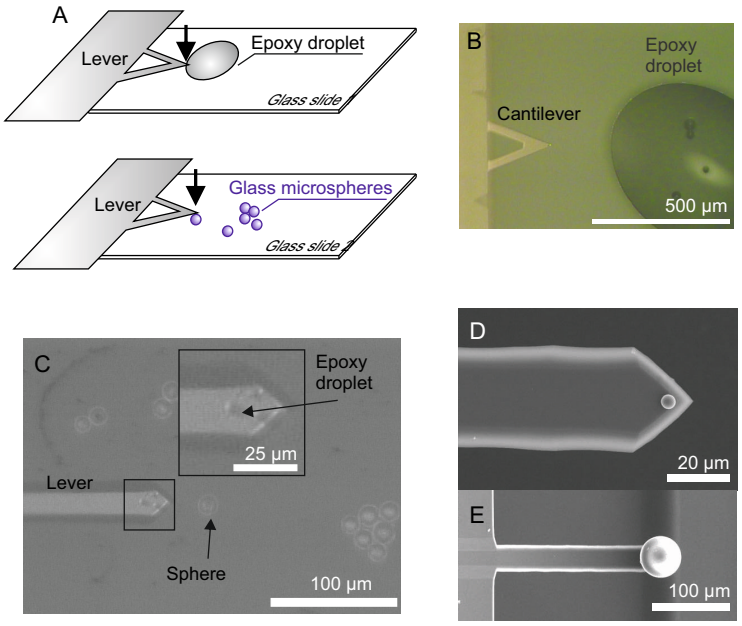

Figure 7.2: (A) Schematic of (B) Optical microscope image of an epoxy droplet on a glass slide and a V–shaped cantilever. (C) Optical microscope image of rectangular lever and the borosilicate glass microspheres (native sphere and aggregates) of 15 μm diameter. (D,E) SEM images of the AIO–TL cantilevers with a 5 μm and a 50 μm sphere attached.

7.2 Conclusion

The aim of the thesis was to investigate potential changes in the mechanical properties of collagen fibrils in osteogenesis imperfecta and asthma and the association of the changes to structural and cross–linking alterations.

To mechanically assess collagen fibrils in a reproducible fashion, the AFM–cantilever based nanoindentation (AFM–cbN) was validated and applied to samples of interest. The validation of AFM–cbN was performed by comparing results with a well established technique, conventional nanoindentation, to test the reliability of the determination of the AFM tip area function.

Results from the validation study showed that AFM–cbN can be used to assess differences in the mechanical properties between to polymeric samples, PMMA and PP.

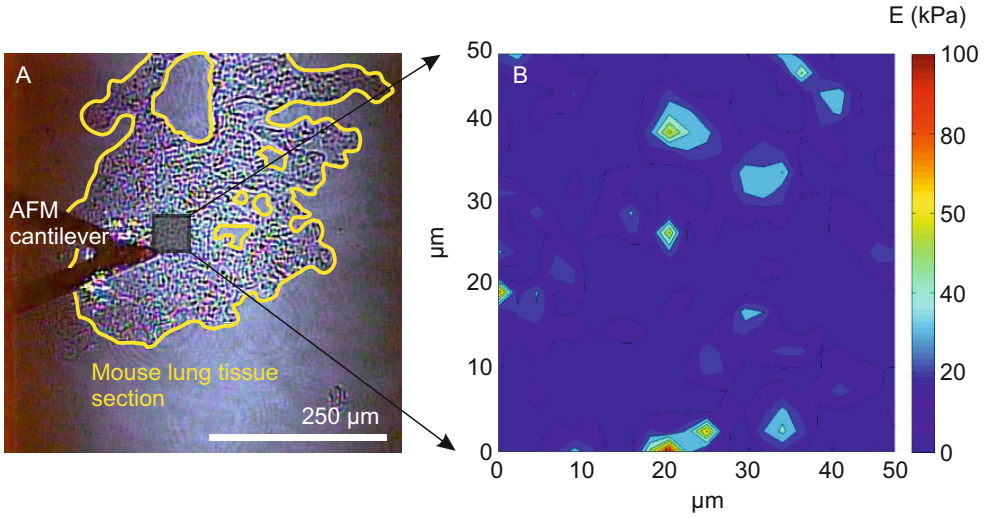

Figure 7.3: (Panel A) Optical microscope image showing the mouse lung tissue section (highlighted with yellow colour) and the V–shaped AFM cantilever (PNP–TR, $k = 0.07$ N/m, $R_{sphere} = 5\mu$m, MicroMasch). (Panel B) Map of the indentation modulus over a $50\mu \times 50\mu$m area.

Further, the reproducibility of AFM–cbN is ensured if the 10% Bueckle's rule is followed when assessing the mechanical properties of collagen fibrils. Even though the lack of a gold standard method to determine the AFM tip area function did not allow for a full calibration of AFM–cbN, results are comparable between the two techniques.

Results from AFM imaging and cantilever–based nanoindentation on *oim* collagen fibrils suggested the association of structural changes of *oim* collagen molecules with the altered indentation modulus of *oim* collagen fibrils. Currently, changes in the indentation modulus can potentially be associated with structural changes at the fibril level based on the microfibril model (Orgel et al., 2006) of collagen structure. Beyond the effect of structural changes, the indentation modulus of *oim* collagen fibrils could also be increased as a result of increased amount of cross–linking (Carriero et al., 2012). This hypothesis was corroborated by the increased indentation modulus of collagen fibrils with chemically induced cross–link (AGEs: advanced glycation end products). Additionally, the increased cross–linking has been shown to reduce the hydration of collagen fibrils (Miles et al., 2005), which could further explain the increased stiffness and indentation modulus at the fibril level. The structural, cross–linking and hydration alterations are believed to decrease the ductility at the fibril, tissue level of collagen and bone.

Furthermore, the type of cross–linking influenced the indentation modulus of collagen fibrils. This was evident by comparing results between healthy and asthmatic individuals, and confirmed by analysing the biochemical assays provided by collaborators. These findings suggested a trend towards lower indentation modulus with increasing the immature to mature cross–linking ratio. Additional factors could be responsible for mechanical changes between healthy and asthmatics. The amount of collagen types I and

III, the abundant collagen types found in the submucosa. It is suggested that the diameter of type I collagen fibrils is decreased with increasing the amount of collagen type III. The biochemistry data suggested a trend towards lower amount of type III collagen in asthmatics. A possible decreased fibril diameter in asthmatics would result in changing the density of the subepithelial layer of the airways and hence the indentation modulus at the tissue level. While it is important to recognize that this work helps to understand the structure–mechanical relationship of collagen fibrils in health and pathology, it is also important to acknowledge that there remains work to be carried out, for providing improved insight on the effect of the different chemistry of cross–linking on the mechanical properties of collagen fibrils.

In summary, this thesis achieved to show the structure–mechanical function of collagen fibrils from *oim* mouse. It was also shown that the amount and type of cross–linking influences the mechanical properties of collagen fibrils. These results enhance our understanding of the effect of structural and cross–linking changes on the mechanical properties of collagen fibrils.

Application of atomic force microscopy cantilever–based nanoindentation for assessing the nanoscale mechanics of collagen fibrils could potentially be used in collaboration with computational simulations (*in silico*) to corroborate results from the later studies. With a fruitful collaboration of experimental and *in silico* studies the results could be used as a predictive tool to assess nanomechanical changes as a result of both structural and cross–linking alterations. Ultimately, it is anticipated that the use AFM–cbN from engineers in collaboration with the medical researchers in academia and industry could lead to the development of diagnostic tools for collagen–related pathologies.

Appendix A

Collagen surface roughness

The surface of collagen fibrils is characterized by convex (peak regions) and concave (trough regions) features, as shown in Figure A.1. Peak to trough distance is about 3 nm. To provide a scale perspective of the contact at these areas, the radius of curvature was determined. For calculations of the radius of curvature refer to Appendix B. The radius of curvature of the convex feature of collagen (R_{CX}; Figure A.1) was calculated, from Equation B.2, to be about 135 nm. This was about 10–fold larger than the AFM tip radius (≈10 nm). Such a large difference has negligible effects on the tip–collagen contact, when assuming the sample surface to be flat. However, the radius of curvature of the concave features (R_{CV}; Figure A.1) was ≈20 nm, comparative in size with the AFM tip. This would result in a rather larger contact surface than the calculated one resulting in a systematic overestimation of the measured indentation modulus.

Shallow indentations of the AFM tip on the convex and concave asperities would result in different contact cases, as illustrated in Figure A.1. The slope between the trough and peak features of collagen could also be a factor for the variation of the data at low indentation depths. The steepest slope was calculated to be 20%. In a similar manner, the contact would be altered at these regions as well as the resulting force-indentation curve leading to systematic errors in calculated indentation modulus values.

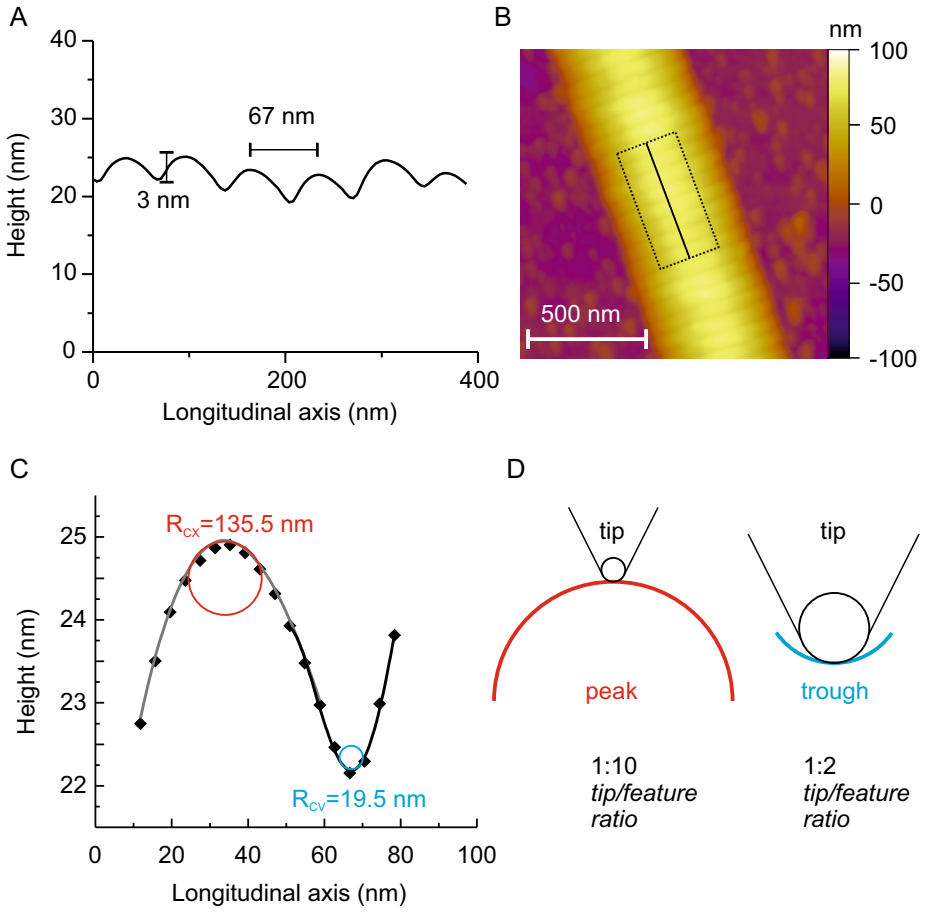

Figure A.1: Contact between the topographical features of collagen surface with the AFM tip. (A) Profile across the longitudinal axis of a collagen fibril with characteristic D-ibanding of 67 nm. The profile graph shown in panel A is an average of profiles taken within the rectangle shown in panel B. (C) Radius of curvatures of a convex (peak) and concave (trough) feature. (D) In scale illustration of contact cases between the AFM tip, the peak and the trough regions. Note that the graph in panel C is not drawn to scale, thus the radius of the circles is smaller than the axis units suggest.

Appendix B

Determination of radius of curvature

Indentation data analysis often assumes a standard tip shape such as a cone with a standard opening angle (2θ) and spherical tip radius (R_{tip}). In this study we have calculated the tip radius of curvature from the reconstructed tip geometry shown in Figure B.1. The two principal profiles were fitted with a polynomial function:

$$y(x) = a + bx + cx^2 + dx^3 \tag{B.1}$$

The radius of curvature from each profile was then determined by:

$$R(x) = \frac{\left(1 + \left(\frac{\partial y}{\partial x}\right)^2\right)^{3/2}}{Abs\left[\frac{\partial^2 y}{\partial x^2}\right]} \tag{B.2}$$

where y is the polynomial function.

Finally the average radius of curvature is determined by combining the two principal radii:

$$R_{avg}(x) = 2\left(\frac{1}{R_1} + \frac{1}{R_2}\right)^{-1} \tag{B.3}$$

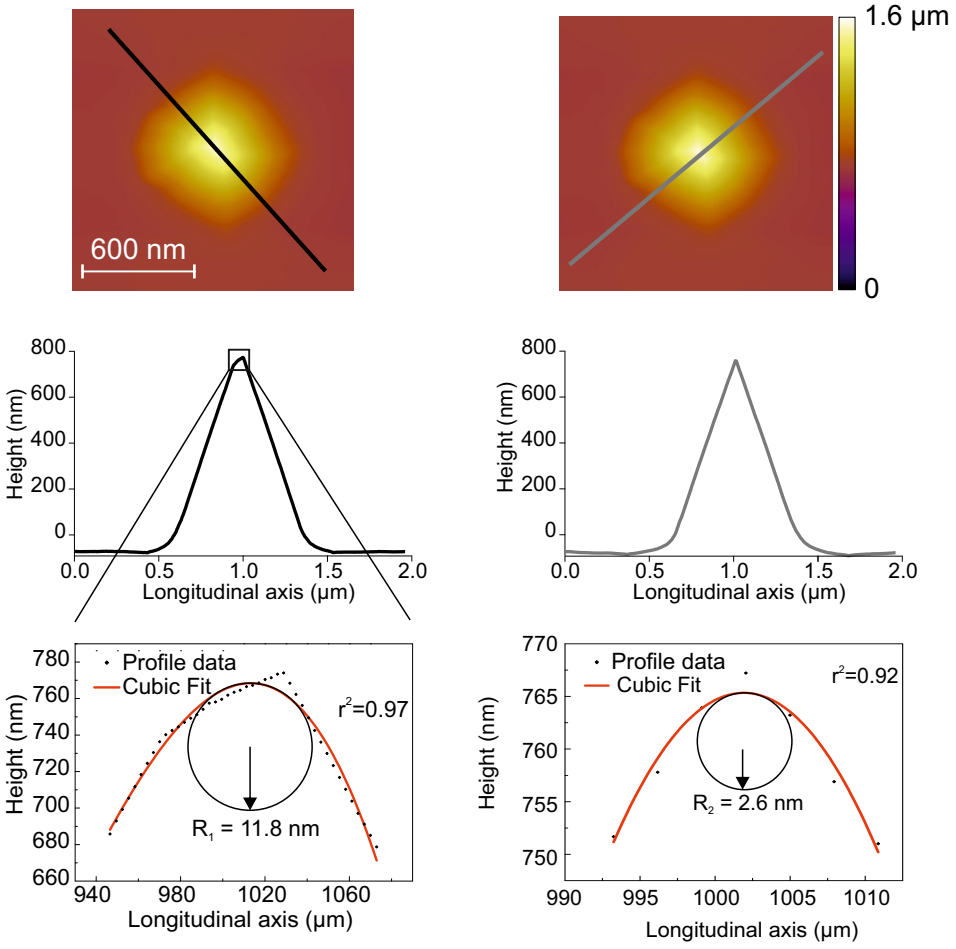

Figure B.1: Determining the tip radius from two principal radii of curvature.

Appendix C

Publications

- **Articles**

  1. **O.G. Andriotis**, W. Manuyakorn, J. Zekonyte, O. L. Katsamenis, S. Fabri, P. H. Howarth, D. E. Davies, P. J. Thurner, 2013. "Comparative nanomechanical evaluation of human and murine collagen fibrils via atomic force microscopy cantilever-based nanoindentation". *Submitted*
  2. **O. G. Andriotis**, SW. Chang, M. Vanleene, P. H. Howarth, D. E. Davies, S. J. Shefelbine, M. J. Buehler, and P. J. Thurner, 2013. "Collagen Fibril Abnormalities from the OIM Mouse Model Measured via Atomic Force Microscopy". *In preparation*
  3. **O.G. Andriotis**, W. Manuyakorn, D. Smart, S. Robins, P. H. Howarth, O. L. Katsamenis, D. E. Davies, P. J. Thurner, 2013. "Nanomechanical implications in collagen fibrils in severe asthmatics". *In preparation*

- **Conference abstracts and proceedings**

  1. **Orestis G Andriotis**, Maximilien Vanleene, Shefelbine Sandra, Philipp Thurner, 2012. "COLLAGEN NANOSTIFFNESS IS SEVERELY IMPAIRED IN OI MICE MODEL", *Journal of Biomechanics*, Vol. 5:S529. *18^{th} Congress of European Society of Biomechanics.*
  2. **Orestis G. Andriotis**, David Smart, Donna E. Davies, Peter H. Howarth, Philipp J. Thurner, 2012. "Non-enzymatic glycation increases indentation modulus of type I native collagen fibrils". Presented at the *Seeing at the Nanoscale* Conference, Bristol, UK.
  3. O. Andriotis1, W. Manuyakorn2, O. L. Katsamenis1, P.H. Howarth2, D.E. Davies2 and P.J Thurner, 2011. "PROBING THE NANOMECHANICAL PROPERTIES OF HUMAN AIRWAY COLLAGEN FIBRILS". *17^{th} Postgraduate Conference of Engineering Sciences.*

- **Awards**

  1. **Orestis G. Andriotis**, David Smart, Wiparat Manuyakorn, Orestis L. Katsamenis, Simon Robins, Peter H. Howarth, Donna E. Davies and Philipp J. Thurner, 2013. "Cross-link density and type are strong determinants of collagen fibril nanoelasticity". ***ESB Student Award*** at the 19^{th} Congress of European Society of Biomechanics.
  2. **Orestis G. Andriotis**, Shu-Wei Chang, Maximilien Vanleene, Peter H. Howarth, Donna E. Davies, Sandra J. Shefelbine, Markus J. Buehler and Philipp J. Thurner, 2012. "COL1A2 gene mutation alters tropocollagen molecules structure and nanoelasticity of collagen fibrils: a joint experimental and computational study". ***Best poster presentation*** at the Postgraduate Conference of Engineering Science in Southampton.

- **Other publications from collaborations**

  1. Katsamenis, O. L., Chong, H.M.H., **Andriotis, O.G.**, Thurner, P.J., 2012. "Load-Bearing in Cortical Bone Microstructure: Selective Stiffening and Heterogeneous Strain Distribution at the Lamellar Level". Journal of the Mechanical Behavior of Biomedical Materials.
  2. O.L. Katsamenis, **O.G. Andriotis** and P.J. Thurner, Distribution of nanoelasticity in osteonal level affects bone fracture toughness behaviour, Abstracts at 18th Congress of the European Society of Biomechanics (ESB), Lisbon, Portugal, July 1-4, 2012.
  3. P.J. Thurner, O. L. Katsamenis, S. Nobakhti, **O. Andriotis**, H. M. H. Chong, G. Limbert, Microstructure, Interfaces, Composition - Towards Better Microscale Experimentation and Models of Bone, Abstract at the 6th European Congress on Computational Methods in Applied Sciences and Engineering (ECCOMAS 2012), Vienna, Austria, September 10-14, 2012.
  4. Y.H. Man, N.D. Evans, R.O.C. Oreffo, **O. Andriotis**, P.J. Thurner, SUBSTRATE STIFFNESS REGULATES SKIN EPIDERMAL CELL MORPHOLOGY, ADHESION AND PROLIFERATION, Abstract at the Postgraduate Conference of Engineering Sciences in Southampton, 2012.
  5. K.Y. Ching, B. Su, P. Basnett, I. Roy, **O. Andriotis**, B. Sengers and M.Stolz, MECHANICAL ADJUSTABLE AND BIODEGRADABLE CARTILAGE IMPLANT MATERIALS FOR TREATMENT OF ARTICULAR CARTILAGE DEFECTS IN KNEE- OR HIP JOINTS, Abstract at the Postgraduate Conference of Engineering Sciences in Southampton, 2012.

References

Allen, M. J., Hud, N. V., Balooch, M., Tench, R. J., Siekhaus, W. J., and Balhorn, R. (1992). Tip-radius-induced artifacts in afm images of protamine-complexed dna fibers. *Ultramicroscopy*, 42:1095–1100.

An, S. S., Kim, J., Ahn, K., Trepat, X., Drake, K. J., Kumar, S., Ling, G., Purington, C., Rangasamy, T., Kensler, T. W., et al. (2009). Cell stiffness, contractile stress and the role of extracellular matrix. *Biochemical and biophysical research communications*, 382(4):697–703.

Asthma, U. (2001). Out in the open: a true picture of asthma in the uk today. *Asthma J*, 6(Suppl 3):1–16.

Avery, N. and Bailey, A. (2008). Restraining cross-links responsible for the mechanical properties of collagen fibers: natural and artificial. In *Collagen*, pages 81–110. Springer.

Bailey, A. and Shimokomaki, M. (1971). Age related changes in the reducible cross-links of collagen. *FEBS letters*, 16(2):86–88.

Bailey, A. J. (2001). Molecular mechanisms of ageing in connective tissues. *Mechanisms of ageing and development*, 122(7):735–755.

Bank, R., Bayliss, M., Lafeber, F., Maroudas, A., and Tekoppele, J. (1998). Ageing and zonal variation in post-translational modification of collagen in normal human articular cartilage. *Biochem. J*, 330:345–351.

Barone, A., Salerno, M., Patra, N., Gastaldi, D., Bertarelli, E., Carnelli, D., and Vena, P. (2010). Calibration issues for nanoindentation experiments: Direct atomic force microscopy measurements and indirect methods. *Microscopy research and technique*, 73(10):996–1004.

Beck, K. and Brodsky, B. (1998). Supercoiled protein motifs: the collagen triple-helix and the α-helical coiled coil. *Journal of structural biology*, 122(1):17–29.

Bella, J., Brodsky, B., and Berman, H. M. (1995). Hydration structure of a collagen peptide. *Structure*, 3(9):893–906.

Bella, J., Eaton, M., Brodsky, B., and Berman, H. M. (1994). Crystal and molecular structure of a collagen-like peptide at 1.9 a resolution. *Science*, 266(5182):75–81.

Binnig, G., Quate, C., and Gerber, C. (1986). Invention of afm. *Phys. Rev. Lett*, 56:930.

Binnig, G. and Rohrer, H. (1983). Scanning tunneling microscopy. *Surface Science*, 126(1):236–244.

Birk, D. (2001). Type v collagen: heterotypic type i/v collagen interactions in the regulation of fibril assembly. *Micron*, 32(3):223–237.

Birk, D. and Mayne, R. (1997). Localization of collagen types i, iii and v during tendon development. changes in collagen types i and iii are correlated with changes in fibril diameter. *European journal of cell biology*, 72(4):352–361.

Black, J. L., Burgess, J. K., and Johnson, P. R. (2003). Airway smooth muscleits relationship to the extracellular matrix. *Respiratory physiology & neurobiology*, 137(2):339–346.

Boulet, L., Bélanger, M., and Carrier, G. (1995). Airway responsiveness and bronchial-wall thickness in asthma with or without fixed airflow obstruction. *American journal of respiratory and critical care medicine*, 152(3):865–871.

Bradding, P., Redington, A. E., and Holgate, S. T. (1997). *Airway wall remodelling in the pathogenesis of asthma: cytokine expression in the airways*. CRC Press Inc. Boca Raton, Florida, USA.

Buckle, H., Westbrook, J., and Conrad, H. (1973). The science of hardness testing and its research applications. *American Society for Metals, Materials Park, Ohio*.

Buehler, M. J. (2006). Atomistic and continuum modeling of mechanical properties of collagen: elasticity, fracture, and self-assembly. *Journal of Materials Research*, 21(08):1947–1961.

Buehler, M. J. (2007). Molecular nanomechanics of nascent bone: fibrillar toughening by mineralization. *Nanotechnology*, 18(29):295102.

Buehler, M. J. (2008). Nanomechanics of collagen fibrils under varying cross-link densities: atomistic and continuum studies. *Journal of the Mechanical Behavior of Biomedical Materials*, 1(1):59–67.

Burton, A. C. (1954). Relation of structure to function of the tissues of the wall of blood vessels. *Physiological reviews*, 34(4):619–642.

Byers, P. H., Wallis, G. A., and Willing, M. C. (1991). Osteogenesis imperfecta: translation of mutation to phenotype. *Journal of medical genetics*, 28(7):433.

Carriero, A., Zimmermann, E. A., Tang, S., Alliston, T., Kazakia, G., Ritchie, R. O., and Shefelbine, S. J. (2012). Preclinical investigation of bone fracture: A multiscale approach for mouse models. In *OSTEOPOROSIS INTERNATIONAL*, volume 23, pages S375–S375. SPRINGER LONDON LTD 236 GRAYS INN RD, 6TH FLOOR, LONDON WC1X 8HL, ENGLAND.

Carroll, N., Elliot, J., Morton, A., and James, A. (1993). The structure of large and small airways in nonfatal and fatal asthma. *American Review of Respiratory Disease*, 147(2):405–410.

Chang, S.-W., Shefelbine, S. J., and Buehler, M. J. (2012). Structural and mechanical differences between collagen homo-and heterotrimers: Relevance for the molecular origin of brittle bone disease. *Biophysical journal*, 102(3):640–648.

Chapman, J. A., Tzaphlidou, M., Meek, K. M., and Kadler, K. E. (1990). The collagen fibrila model system for studying the staining and fixation of a protein. *Electron microscopy reviews*, 3(1):143–182.

Chetta, A., Foresi, A., Del Donno, M., Bertorelli, G., Pesci, A., and Olivieri, D. (1997). Airways remodeling is a distinctive feature of asthma and is related to severity of disease. *CHEST Journal*, 111(4):852–857.

Chipman, S. D., Sweet, H. O., McBride, D. J., Davisson, M. T., Marks, S. C., Shuldiner, A. R., Wenstrup, R. J., Rowe, D. W., and Shapiro, J. R. (1993). Defective pro alpha 2 (i) collagen synthesis in a recessive mutation in mice: a model of human osteogenesis imperfecta. *Proceedings of the National Academy of Sciences*, 90(5):1701–1705.

Chu, H. W., Halliday, J. L., Martin, R. J., Leung, D. Y., Szefler, S. J., and Wenzel, S. E. (1998). Collagen deposition in large airways may not differentiate severe asthma from milder forms of the disease. *American journal of respiratory and critical care medicine*, 158(6):1936–1944.

Clark, J. G., Kuhn 3rd, C., McDonald, J. A., and Mecham, R. P. (1983). Lung connective tissue. *International review of connective tissue research*, 10:249.

Clifford, C. A. and Seah, M. P. (2005). Quantification issues in the identification of nanoscale regions of homopolymers using modulus measurement via afm nanoindentation. *Applied surface science*, 252(5):1915–1933.

Coats, A., Zioupos, P., and Aspden, R. (2003). Material properties of subchondral bone from patients with osteoporosis or osteoarthritis by microindentation testing and electron probe microanalysis. *Calcified tissue international*, 73(1):66–71.

Cross, S. E., Jin, Y.-S., Rao, J., and Gimzewski, J. K. (2007). Nanomechanical analysis of cells from cancer patients. *Nature nanotechnology*, 2(12):780–783.

Currey, J. D. (2003). Role of collagen and other organics in the mechanical properties of bone. *Osteoporosis international*, 14:S29–S36.

Currey, J. D. (2005). Hierarchies in biomineral structures. *Science*, 309(5732):253–254.

Cusack, S. and Miller, A. (1979). Determination of the elastic constants of collagen by brillouin light scattering. *Journal of molecular biology*, 135(1):39–51.

Diamant, J., Keller, A., Baer, E., Litt, M., and Arridge, R. (1972). Collagen; ultrastructure and its relation to mechanical properties as a function of ageing. *Proceedings of the Royal Society of London. Series B. Biological Sciences*, 180(1060):293–315.

Dickenson, R., Hutton, W., et al. (1981). The mechanical properties of bone in osteoporosis. *Journal of Bone & Joint Surgery, British Volume*, 63(2):233–238.

Discher, D. E., Janmey, P., and Wang, Y.-l. (2005). Tissue cells feel and respond to the stiffness of their substrate. *Science*, 310(5751):1139–1143.

Eanes, E. D. (1992). Dynamics of calcium phosphate precipitation. *Calcification in biological systems. CRC Press, Boca Raton, FL*, pages 1–18.

Engler, A. J., Sen, S., Sweeney, H. L., and Discher, D. E. (2006). Matrix elasticity directs stem cell lineage specification. *Cell*, 126(4):677–689.

Eppell, S., Smith, B., Kahn, H., and Ballarini, R. (2006). Nano measurements with micro-devices: mechanical properties of hydrated collagen fibrils. *Journal of the Royal Society Interface*, 3(6):117–121.

Eyre, D. R. and Wu, J.-J. (2005). Collagen cross-links. In *Collagen*, pages 207–229. Springer.

Fantner, G. E., Rabinovych, O., Schitter, G., Thurner, P., Kindt, J. H., Finch, M. M., Weaver, J. C., Golde, L. S., Morse, D. E., Lipman, E. A., et al. (2006). Hierarchical interconnections in the nano-composite material bone: Fibrillar cross-links resist fracture on several length scales. *Composites science and technology*, 66(9):1205–1211.

Fischer-Cripps, A. C. (2012). *Nanoindentation*, volume 1. Springer.

Folkestad, L., Hald, J. D., Hansen, S., Gram, J., Langdahl, B., Abrahamsen, B., and Brixen, K. (2012). Bone geometry, density, and microarchitecture in the distal radius and tibia in adults with osteogenesis imperfecta type i assessed by high-resolution pqct. *Journal of Bone and Mineral Research*, 27(6):1405–1412.

Franchi, M., Fini, M., Quaranta, M., De Pasquale, V., Raspanti, M., Giavaresi, G., Ottani, V., and Ruggeri, A. (2007). Crimp morphology in relaxed and stretched rat achilles tendon. *Journal of anatomy*, 210(1):1–7.

Fraser, R., MacRae, T., Miller, A., and Suzuki, E. (1983). Molecular conformation and packing in collagen fibrils. *Journal of molecular biology*, 167(2):497–521.

Fratzl, P. (2003). Cellulose and collagen: from fibres to tissues. *Current opinion in colloid & interface science*, 8(1):32–39.

Fratzl, P., Gupta, H., Paschalis, E., and Roschger, P. (2004). Structure and mechanical quality of the collagen–mineral nano-composite in bone. *Journal of Materials Chemistry*, 14(14):2115–2123.

Fratzl, P., Misof, K., Zizak, I., Rapp, G., Amenitsch, H., and Bernstorff, S. (1998). Fibrillar structure and mechanical properties of collagen. *Journal of structural biology*, 122(1):119–122.

Fratzl, P., Paris, O., Klaushofer, K., and Landis, W. (1996). Bone mineralization in an osteogenesis imperfecta mouse model studied by small-angle x-ray scattering. *Journal of Clinical Investigation*, 97(2):396.

Fratzl, P. and Weinkamer, R. (2007). Natures hierarchical materials. *Progress in Materials Science*, 52(8):1263–1334.

Gadelrab, K. and Chiesa, M. (2012). Numerically assisted nanoindentation analysis. *Materials Science and Engineering: A*.

Garcia, R. and San Paulo, A. (1999). Attractive and repulsive tip-sample interaction regimes in tapping-mode atomic force microscopy. *Physical Review B*, 60(7):4961.

Gautieri, A., Buehler, M. J., and Redaelli, A. (2009a). Deformation rate controls elasticity and unfolding pathway of single tropocollagen molecules. *Journal of the Mechanical Behavior of Biomedical Materials*, 2(2):130–137.

Gautieri, A., Uzel, S., Vesentini, S., Redaelli, A., and Buehler, M. J. (2009b). Molecular and mesoscale mechanisms of osteogenesis imperfecta disease in collagen fibrils. *Biophysical journal*, 97(3):857–865.

Gautieri, A., Vesentini, S., Redaelli, A., and Buehler, M. J. (2009c). Single molecule effects of osteogenesis imperfecta mutations in tropocollagen protein domains. *Protein Science*, 18(1):161–168.

Gautieri, A., Vesentini, S., Redaelli, A., and Buehler, M. J. (2011). Hierarchical structure and nanomechanics of collagen microfibrils from the atomistic scale up. *Nano letters*, 11(2):757–766.

Godfrey, M. (2009). Extracellular matrix. *Asthma and COPD. Basic Mechanisms and Clinical Management*, pages 265–274.

Gold, D. R. and Wright, R. (2005). Population disparities in asthma. *Annu. Rev. Public Health*, 26:89–113.

Grabner, B., Landis, W., Roschger, P., Rinnerthaler, S., Peterlik, H., Klaushofer, K., and Fratzl, P. (2001). Age-and genotype-dependence of bone material properties in the osteogenesis imperfecta murine model (oim). *Bone*, 29(5):453–457.

Grant, C. A., Brockwell, D. J., Radford, S. E., and Thomson, N. H. (2008). Effects of hydration on the mechanical response of individual collagen fibrils. *Applied Physics Letters*, 92(23):233902–233902.

Grant, C. A., Brockwell, D. J., Radford, S. E., and Thomson, N. H. (2009). Tuning the elastic modulus of hydrated collagen fibrils. *Biophysical journal*, 97(11):2985–2992.

Grant, C. A., Phillips, M. A., and Thomson, N. H. (2012). Dynamic mechanical analysis of collagen fibrils at the nanoscale. *Journal of the Mechanical Behavior of Biomedical Materials*, 5(1):165–170.

Grunlan, J. C., Xia, X., Rowenhorst, D., and Gerberich, W. W. (2001). Preparation and evaluation of tungsten tips relative to diamond for nanoindentation of soft materials. *Review of Scientific Instruments*, 72(6):2804–2810.

Gumbiner, B. M. (1996). Cell adhesion: the molecular basis of tissue architecture and morphogenesis. *Cell*, 84(3):345–357.

Gupta, H., Messmer, P., Roschger, P., Bernstorff, S., Klaushofer, K., and Fratzl, P. (2004). Synchrotron diffraction study of deformation mechanisms in mineralized tendon. *Physical review letters*, 93(15):158101.

Gupta, H. S., Seto, J., Wagermaier, W., Zaslansky, P., Boesecke, P., and Fratzl, P. (2006). Cooperative deformation of mineral and collagen in bone at the nanoscale. *Proceedings of the National Academy of Sciences*, 103(47):17741–17746.

Harley, R., James, D., Miller, A., and White, J. (1977). Phonons and the elastic moduli of collagen and muscle. *Nature*, 267:285–287.

Heim, A. J., Koob, T. J., and Matthews, W. G. (2007). Low strain nanomechanics of collagen fibrils. *Biomacromolecules*, 8(11):3298–3301.

Heim, A. J., Matthews, W. G., and Koob, T. J. (2006). Determination of the elastic modulus of native collagen fibrils via radial indentation. *Applied physics letters*, 89(18):181902–181902.

Heuck, C., Wolthers, O. D., Hansen, M., and Kollerup, G. (1997). Short-term growth and collagen turnover in asthmatic adolescents treated with the inhaled glucocorticoid budesonide. *Steroids*, 62(10):659–664.

Hoff, C. R., Perkins, D. R., and Davidson, J. M. (1999). Elastin gene expression is upregulated during pulmonary fibrosis. *Connective tissue research*, 40(2):145–153.

Holgate, S., Arshad, H., Roberts, G., Howarth, P., Thurner, P., and Davies, D. (2010). A new look at the pathogenesis of asthma. *Clinical Science*, 118:439–450.

Holgate, S. T. (2009). Airway remodeling. *Asthma and COPD. Basic Mechanisms and Clinical Management*, pages 82–95.

Hopcroft, M. A., Nix, W. D., and Kenny, T. W. (2010). What is the young's modulus of silicon? *Microelectromechanical Systems, Journal of*, 19(2):229–238.

Hoshino, M., Nakamura, Y., and Sim, J. J. (1998). Expression of growth factors and remodelling of the airway wall in bronchial asthma. *Thorax*, 53(1):21–27.

Hulmes, D. (2008). Collagen diversity, synthesis and assembly. In *Collagen*, pages 15–47. Springer.

Hulmes, D., Wess, T. J., Prockop, D. J., and Fratzl, P. (1995). Radial packing, order, and disorder in collagen fibrils. *Biophysical Journal*, 68(5):1661–1670.

Hulmes, D. J. and Miller, A. (1979). Quasi-hexagonal molecular packing in collagen fibrils. *Nature*.

Irvin, C. G. (2009). Chapter 5 - pulmonary physiology. In *Asthma and COPD: Basic Mechanisms and Clinical Management*, pages 53 – 69. Academic Press, Oxford, second edition.

Jäger, I. and Fratzl, P. (2000). Mineralized collagen fibrils: a mechanical model with a staggered arrangement of mineral particles. *Biophysical Journal*, 79(4):1737–1746.

James, A. L., Paré, P. D., and Hogg, J. C. (1989). The mechanics of airway narrowing in asthma. *American Review of Respiratory Disease*, 139(1):242–246.

Jones, E. Y. and Miller, A. (1991). Analysis of structural design features in collagen. *Journal of molecular biology*, 218(1):209–219.

Kadler, K., Holmes, D., Trotter, J., and Chapman, J. (1996). Collagen fibril formation. *Biochem. J*, 316:1–11.

Kamoun-Goldrat, A. S. and Le Merrer, M. F. (2007). Animal models of osteogenesis imperfecta and related syndromes. *Journal of bone and mineral metabolism*, 25(4):211–218.

Kannus, P. (2000). Structure of the tendon connective tissue. *Scandinavian journal of medicine & science in sports*, 10(6):312–320.

Kawana, S. and Jones, R. A. (2001). Character of the glass transition in thin supported polymer films. *Physical Review E*, 63(2):021501.

Keller, D. J. and Franke, F. S. (1993). Envelope reconstruction of probe microscope images. *Surface Science*, 294(3):409–419.

Khoshnoodi, J., Cartailler, J.-P., Alvares, K., Veis, A., and Hudson, B. G. (2006). Molecular recognition in the assembly of collagens: terminal noncollagenous domains are key recognition modules in the formation of triple helical protomers. *Journal of Biological Chemistry*, 281(50):38117–38121.

King, J. D. and Bobechko, W. P. (1971). Osteogenesis imperfecta an orthopaedic description and surgical review. *Journal of Bone & Joint Surgery, British Volume*, 53(1):72–89.

Kivirikko, K. I. and Prockop, D. J. (1967). Enzymatic hydroxylation of proline and lysine in protocollagen. *Proceedings of the National Academy of Sciences of the United States of America*, 57(3):782.

Kucharz, E. J. (1992). *The collagens: biochemistry and pathophysiology*. Springer.

Kühn, K. (1986). The collagen family-variations in the molecular and supermolecular structure. *Rheumatology*, 10:29–69.

Kuwano, K., Bosken, C. H., Paré, P. D., Bai, T. R., Wiggs, B. R., and Hogg, J. C. (1993). Small airways dimensions in asthma and in chronic obstructive pulmonary disease. *American Review of Respiratory Disease*, 148(5):1220–1225.

Kuznetsova, N. V., McBride Jr, D. J., and Leikin, S. (2003). Changes in thermal stability and microunfolding pattern of collagen helix resulting from the loss of α2 (i) chain in osteogenesis imperfecta murine. *Journal of molecular biology*, 331(1):191–200.

Lambert, R. K. (1991). Role of bronchial basement membrane in airway collapse. *Journal of Applied Physiology*, 71(2):666–673.

Landis, W., Song, M., Leith, A., McEwen, L., and McEwen, B. (1993). Mineral and organic matrix interaction in normally calcifying tendon visualized in three dimensions by high-voltage electron microscopic tomography and graphic image reconstruction. *Journal of structural biology*, 110(1):39–54.

Launey, M. E., Chen, P.-Y., McKittrick, J., and Ritchie, R. O. (2010). Mechanistic aspects of the fracture toughness of elk antler bone. *Acta Biomaterialia*, 6(4):1505–1514.

Leblond, C. and Inoue, S. (1989). Structure, composition, and assembly of basement membrane. *American journal of anatomy*, 185(4):367–390.

Lo, C.-M., Wang, H.-B., Dembo, M., and Wang, Y.-l. (2000). Cell movement is guided by the rigidity of the substrate. *Biophysical journal*, 79(1):144–152.

Lodish, H., Berk, A., Zipursky, S. L., Matsudaira, P., Baltimore, D., Darnell, J., et al. (2000). Collagen: the fibrous proteins of the matrix.

Loparic, M., Wirz, D., Daniels, A., Raiteri, R., VanLandingham, M. R., Guex, G., Martin, I., Aebi, U., and Stolz, M. (2010). Micro-and nanomechanical analysis of articular cartilage by indentation-type atomic force microscopy: validation with a gel-microfiber composite. *Biophysical journal*, 98(11):2731–2740.

Maillard, L. (1912). Action of amino acids on sugars. formation of melanoidins in a methodical way. *Compt. Rend*, 154:66–68.

Maksym, G. N. and Bates, J. H. (1997). A distributed nonlinear model of lung tissue elasticity. *Journal of applied physiology*, 82(1):32–41.

Martinez, F. (2007). Genes, environments, development and asthma: a reappraisal. *European Respiratory Journal*, 29(1):179–184.

McBride, D. J., Choe, V., Shapiro, J. R., and Brodsky, B. (1997). Altered collagen structure in mouse tail tendon lacking the $\alpha 2$ (i) chain. *Journal of molecular biology*, 270(2):275–284.

McFadden Jr, E. and Gilbert, I. A. (1994). Exercise-induced asthma. *New England Journal of Medicine*, 330(19):1362–1367.

Mendler, M., Eich-Bender, S. G., Vaughan, L., Winterhalter, K. H., and Bruckner, P. (1989). Cartilage contains mixed fibrils of collagen types ii, ix, and xi. *The Journal of cell biology*, 108(1):191–197.

Miles, C. A., Avery, N. C., Rodin, V. V., and Bailey, A. J. (2005). The increase in denaturation temperature following cross-linking of collagen is caused by dehydration of the fibres. *Journal of molecular biology*, 346(2):551–556.

Miles, C. A., Sims, T. J., Camacho, N. P., and Bailey, A. J. (2002). The role of the $\alpha 2$ chain in the stabilization of the collagen type i heterotrimer: A study of the type i homotrimer in¡ i¿ oim¡/i¿ mouse tissues. *Journal of molecular biology*, 321(5):797–805.

Miller, E., Delos, D., Baldini, T., Wright, T. M., and Camacho, N. P. (2007). Abnormal mineral-matrix interactions are a significant contributor to fragility in oim/oim bone. *Calcified tissue international*, 81(3):206–214.

Misof, K., Landis, W., Klaushofer, K., and Fratzl, P. (1997a). Collagen from the osteogenesis imperfecta mouse model (oim) shows reduced resistance against tensile stress. *Journal of Clinical Investigation*, 100(1):40.

Misof, K., Rapp, G., and Fratzl, P. (1997b). A new molecular model for collagen elasticity based on synchrotron x-ray scattering evidence. *Biophysical journal*, 72(3):1376–1381.

Mogilner, I. G., Ruderman, G., and Grigera, J. R. (2002). Collagen stability, hydration and native state. *Journal of molecular Graphics and Modelling*, 21(3):209–213.

Montesano, R. and Orci, L. (1988). Transforming growth factor beta stimulates collagen-matrix contraction by fibroblasts: implications for wound healing. *Proceedings of the National Academy of Sciences*, 85(13):4894–4897.

Myllyharju, J. and Kivirikko, K. I. (2001). Collagens and collagen-related diseases. *Annals of medicine*, 33(1):7–21.

Myllyharju, J. and Kivirikko, K. I. (2004). Collagens, modifying enzymes and their mutations in humans, flies and worms. *TRENDS in Genetics*, 20(1):33–43.

Nalla, R., Balooch, M., Ager Iii, J., Kruzic, J., Kinney, J., and Ritchie, R. (2005). Effects of polar solvents on the fracture resistance of dentin: role of water hydration. *Acta biomaterialia*, 1(1):31–43.

Nihlberg, K., Larsen, K., Hultgardh-Nilsson, A., Malmstrom, A., Bjermer, L., and Westergren-Thorsson, G. (2006). Tissue fibrocytes in patients with mild asthma: a possible link to thickness of reticular basement membrane. *Respir Res*, 7(50):50.

Oliver, W. C. and Pharr, G. M. (2004). Measurement of hardness and elastic modulus by instrumented indentation: Advances in understanding and refinements to methodology. *Journal of materials research*, 19(01):3–20.

Orgel, J. P., Irving, T. C., Miller, A., and Wess, T. J. (2006). Microfibrillar structure of type i collagen in situ. *Proceedings of the National Academy of Sciences*, 103(24):9001–9005.

Ottani, V., Raspanti, M., and Ruggeri, A. (2001). Collagen structure and functional implications. *Micron*, 32(3):251–260.

Oxlund, H. and Andreassen, T. (1980). The roles of hyaluronic acid, collagen and elastin in the mechanical properties of connective tissues. *Journal of anatomy*, 131(Pt 4):611.

Pagon, R. A., Bird, T. D., Dolan, C. R., Stephens, K., Adam, M. P., Steiner, R. D., Adsit, J., Basel, D., et al. (2005). Col1a1/2-related osteogenesis imperfecta.

Pashley, D. H., Agee, K. A., Carvalho, R. M., Lee, K.-W., Tay, F. R., and Callison, T. E. (2003). Effects of water and water-free polar solvents on the tensile properties of demineralized dentin. *Dental Materials*, 19(5):347–352.

Paterson, C. R., McAllion, S., and Stellman, J. L. (1984). Osteogenesis imperfecta after the menopause. *New England Journal of Medicine*, 310(26):1694–1696.

Pelham, R. J. and Wang, Y.-l. (1997). Cell locomotion and focal adhesions are regulated by substrate flexibility. *Proceedings of the National Academy of Sciences*, 94(25):13661–13665.

Persch, G., Born, C., and Utesch, B. (1994). Nano-hardness investigations of thin films by an atomic force microscope. *Microelectronic Engineering*, 24(1):113–121.

Petruska, J. A. and Hodge, A. J. (1964). A subunit model for the tropocollagen macromolecule. *Proceedings of the National Academy of Sciences of the United States of America*, 51(5):871.

Pharr, G. M. and Bolshakov, A. (2002). Undestanding nanoindentation unloading curves. *Journal of Materials Research*, 17(10):2660–2671.

Phillips, C., Bradley, D., Schlotzhauer, C., Bergfeld, M., Libreros-Minotta, C., Gawenis, L., Morris, J., Clarke, L., and Hillman, L. (2000). ¡ i¿ oim¡/i¿ mice exhibit altered femur and incisor mineral composition and decreased bone mineral density. *Bone*, 27(2):219–226.

Phillips, C. L., Pfeiffer, B. J., Luger, A. M., and Franklin, C. L. (2002). Novel collagen glomerulopathy in a homotrimeric type i collagen mouse (oim). *Kidney international*, 62(2):383–391.

Prockop, D. J. and Kivirikko, K. I. (1984). Heritable diseases of collagen. *The New England journal of medicine*, 311(6):376–386.

Prockop, D. J., Kivirikko, K. I., Tuderman, L., Guzman, N. A., et al. (1979). The biosynthesis of collagen and its disorders (first of two parts). *The New England journal of medicine*, 301(1):13–23.

Prockop, J. (1995). Collagens: molecular biology, diseases, and potentials for therapy. *Annual review of biochemistry*, 64(1):403–434.

Puttock, M. and Thwaite, E. (1969). *Elastic compression of spheres and cylinders at point and line contact*. Commonwealth Scientific and Industrial Research Organization Melbourne, Australia.

Ramachandran, G., Bansal, M., and Bhatnagar, R. (1973). A hypothesis on the role of hydroxyproline in stabilizing collagen structure. *Biochimica et Biophysica Acta (BBA)-Protein Structure*, 322(1):166–171.

Ramachandran, G. and Kartha, G. (1954). Structure of collagen. *Nature*, pages 269–270.

Rauch, F. and Glorieux, F. H. (2004). Osteogenesis imperfecta. *The Lancet*, 363(9418):1377–1385.

Rauch, F. and Glorieux, F. H. (2005). Osteogenesis imperfecta, current and future medical treatment. In *American Journal of Medical Genetics Part C: Seminars in Medical Genetics*, volume 139, pages 31–37. Wiley Online Library.

Rauch, F., Land, C., Cornibert, S., Schoenau, E., and Glorieux, F. H. (2005). High and low density in the same bone: a study on children and adolescents with mild osteogenesis imperfecta. *Bone*, 37(5):634–641.

Reihsner, R. and Menzel, E. (1998). Two-dimensional stress-relaxation behavior of human skin as influenced by non-enzymatic glycation and the inhibitory agent aminoguanidine. *Journal of biomechanics*, 31(11):985–993.

Reiser, K., McCormick, R., and Rucker, R. (1992). Enzymatic and nonenzymatic cross-linking of collagen and elastin. *The FASEB Journal*, 6(7):2439–2449.

Reiser, K. M. (1991). Nonenzymatic glycation of collagen in aging and diabetes. In *Proceedings of the Society for Experimental Biology and Medicine. Society for Experimental Biology and Medicine (New York, NY)*, volume 196, pages 17–29. Royal Society of Medicine.

Rho, J.-Y. (1996). An ultrasonic method for measuring the elastic properties of human tibial cortical and cancellous bone. *Ultrasonics*, 34(8):777–783.

Rho, J.-Y., Kuhn-Spearing, L., and Zioupos, P. (1998). Mechanical properties and the hierarchical structure of bone. *Medical engineering & physics*, 20(2):92–102.

Ricci, D. and Braga, P. C. (2004). Recognizing and avoiding artifacts in afm imaging. In *Atomic Force Microscopy*, pages 25–37. Springer.

Robins, S. P. and Bailey, A. J. (1977). The chemistry of the collagen cross-links. characterization of the products of reduction of skin, tendon and bone with sodium cyanoborohydride. *Biochem. J*, 163:339–346.

Roche, W., Williams, J., Beasley, R., and Holgate, S. (1989). Subepithelial fibrosis in the bronchi of asthmatics. *The Lancet*, 333(8637):520–524.

Sader, J. E., Chon, J. W., and Mulvaney, P. (1999). Calibration of rectangular atomic force microscope cantilevers. *Review of Scientific Instruments*, 70:3967–3969.

Saito, M. and Marumo, K. (2010). Collagen cross-links as a determinant of bone quality: a possible explanation for bone fragility in aging, osteoporosis, and diabetes mellitus. *Osteoporosis international*, 21(2):195–214.

Sato, M., Grese, T. A., Dodge, J. A., Bryant, H. U., and Turner, C. H. (1999). Emerging therapies for the prevention or treatment of postmenopausal osteoporosis. *Journal of medicinal chemistry*, 42(1):1–24.

Satomi, N., Takahara, A., and Kajiyama, T. (1999). Determination of surface glass transition temperature of monodisperse polystyrene based on temperature-dependent scanning viscoelasticity microscopy. *Macromolecules*, 32(13):4474–4476.

Scott, J. (1980). Collagen–proteoglycan interactions. localization of proteoglycans in tendon by electron microscopy. *Biochem. J*, 187:887–891.

Scott, J. E., Orford, C. R., and Hughes, E. W. (1981). Proteoglycan-collagen arrangements in developing rat tail tendon. an electron microscopical and biochemical investigation. *Biochem. J*, 195:573–581.

Shen, Z. L., Dodge, M. R., Kahn, H., Ballarini, R., and Eppell, S. J. (2008). Stress-strain experiments on individual collagen fibrils. *Biophysical Journal*, 95(8):3956–3963.

Shen, Z. L., Kahn, H., Ballarini, R., and Eppell, S. J. (2011). Viscoelastic properties of isolated collagen fibrils. *Biophysical journal*, 100(12):3008–3015.

Shoulders, M. D. and Raines, R. T. (2009). Collagen structure and stability. *Annual review of biochemistry*, 78:929.

Silver, D., Miller, J., Harrison, R., and Prockop, D. J. (1992). Helical model of nucleation and propagation to account for the growth of type i collagen fibrils from symmetrical pointed tips: a special example of self-assembly of rod-like monomers. *Proceedings of the National Academy of Sciences*, 89(20):9860–9864.

Sims, T., Miles, C., Bailey, A., and Camacho, N. (2003). Properties of collagen in oim mouse tissues. *Connective tissue research*, 44(1):202–205.

Smith, J. (1968). Molecular pattern in native collagen. *Nature*, 219:157–158.

Stolz, M., Gottardi, R., Raiteri, R., Miot, S., Martin, I., Imer, R., Staufer, U., Raducanu, A., Düggelin, M., Baschong, W., et al. (2009). Early detection of aging cartilage and osteoarthritis in mice and patient samples using atomic force microscopy. *Nature nanotechnology*, 4(3):186–192.

Svensson, R. B., Hassenkam, T., Grant, C. A., and Magnusson, S. P. (2010). Tensile properties of human collagen fibrils and fascicles are insensitive to environmental salts. *Biophysical journal*, 99(12):4020–4027.

Svensson, R. B., Mulder, H., Kovanen, V., and Magnusson, S. P. (2013). Fracture mechanics of collagen fibrils: Influence of natural cross-links. *Biophysical journal*, 104(11):2476–2484.

Swadener, J., Rho, J.-Y., and Pharr, G. (2001). Effects of anisotropy on elastic moduli measured by nanoindentation in human tibial cortical bone. *Journal of biomedical materials research*, 57(1):108–112.

Tang, S., Zeenath, U., and Vashishth, D. (2007). Effects of non-enzymatic glycation on cancellous bone fragility. *Bone*, 40(4):1144–1151.

Traub, W., Arad, T., Vetter, U., and Weiner, S. (1994). Ultrastructural studies of bones from patients with osteogenesis imperfecta. *Matrix Biology*, 14(4):337–345.

Trus, B. L. and Piez, K. A. (1980). Compressed microfibril models of the native collagen fibril. *Nature*.

Tschumperlin, D. J., Shively, J. D., Kikuchi, T., and Drazen, J. M. (2003). Mechanical stress triggers selective release of fibrotic mediators from bronchial epithelium. *American journal of respiratory cell and molecular biology*, 28(2):142–149.

van der Rijt, J. A., van der Werf, K. O., Bennink, M. L., Dijkstra, P. J., and Feijen, J. (2006). Micromechanical testing of individual collagen fibrils. *Macromolecular bioscience*, 6(9):697–702.

Van Noort, S. J. T., Van der Werf, K. O., De Grooth, B. G., Van Hulst, N. F., and Greve, J. (1997). Height anomalies in tapping mode atomic force microscopy in air caused by adhesion. *Ultramicroscopy*, 69(2):117–127.

Vanleene, M., Porter, A., Guillot, P.-V., Boyde, A., Oyen, M., and Shefelbine, S. (2012). Ultra-structural defects cause low bone matrix stiffness despite high mineralization in osteogenesis imperfecta mice. *Bone*, 50(6):1317–1323.

Vashishth, D., Gibson, G., Khoury, J., Schaffler, M., Kimura, J., and Fyhrie, D. (2001). Influence of nonenzymatic glycation on biomechanical properties of cortical bone. *Bone*, 28(2):195–201.

Vetter, U., Eanes, E., Kopp, J., Termine, J., and Robey, P. G. (1991). Changes in apatite crystal size in bones of patients with osteogenesis imperfecta. *Calcified tissue international*, 49(4):248–250.

Ward, C., Pais, M., Bish, R., Reid, D., Feltis, B., Johns, D., and Walters, E. (2002). Airway inflammation, basement membrane thickening and bronchial hyperresponsiveness in asthma. *Thorax*, 57(4):309–316.

Weinberger, M. (2000). Corticosteroids for exacerbations of asthma: problems and solutions. *The Journal of Pediatrics*, 136(3):276–278.

Weinberger, M. (2004). Respiratory infections and asthma: current treatment strategies. *Drug discovery today*, 9(19):831–837.

Weiner, S. and Wagner, H. D. (1998). The material bone: structure-mechanical function relations. *Annual Review of Materials Science*, 28(1):271–298.

Wenger, M. P., Bozec, L., Horton, M. A., and Mesquida, P. (2007). Mechanical properties of collagen fibrils. *Biophysical journal*, 93(4):1255–1263.

Wess, T., Hammersley, A., Wess, L., and Miller, A. (1995). Type i collagen packing, conformation of the triclinic unit cell. *Journal of molecular biology*, 248(2):487–493.

Williams, B. R., Gelman, R. A., Poppke, D. C., and Piez, K. A. (1978). Collagen fibril formation. *J. biol. Chem*, 253(18):6578–6585.

Wilson, E. B. and Worcester, J. (1945). The normal logarithmic transform. *The Review of Economics and Statistics*, 27(1):17–22.

Yamauchi, M. and Shiiba, M. (2008). Lysine hydroxylation and cross-linking of collagen. In *Post-translational Modifications of Proteins*, pages 95–108. Springer.

Yang, L., van der Werf, K. O., Koopman, B. F., Subramaniam, V., Bennink, M. L., Dijkstra, P. J., and Feijen, J. (2007). Micromechanical bending of single collagen fibrils using atomic force microscopy. *Journal of Biomedical Materials Research Part A*, 82(1):160–168.

Yeung, T., Georges, P. C., Flanagan, L. A., Marg, B., Ortiz, M., Funaki, M., Zahir, N., Ming, W., Weaver, V., and Janmey, P. A. (2005). Effects of substrate stiffness on cell morphology, cytoskeletal structure, and adhesion. *Cell motility and the cytoskeleton*, 60(1):24–34.

Yuan, H., Kononov, S., Cavalcante, F. S., Lutchen, K. R., Ingenito, E. P., and Suki, B. (2000). Effects of collagenase and elastase on the mechanical properties of lung tissue strips. *Journal of Applied Physiology*, 89(1):3–14.